

Quantum Dot Probes for Neuroimaging and Visualization of Extracellular Vesicles

Mengying Zhang

A dissertation

submitted in partial fulfilment of the
requirements for the degree of

Doctor of Philosophy

University of Washington

2020

Reading Committee:

Elizabeth Nance, Chair

Vincent Holmberg

Lucia Vojtech

Program Authorized to Offer Degree:

Molecular Engineering and Sciences

©Copyright 2020

Mengying Zhang

University of Washington

Abstract

Quantum Dot Probes for Neuroimaging and Visualization of Extracellular Vesicles

Mengying Zhang

Chair of the Supervisory Committee:

Elizabeth Nance

Department of Chemical Engineering

Central nervous system (CNS) diseases have long known hard to treat due to (1) highly restricted barriers such as the blood brain barrier (BBB) and the brain parenchyma penetration barrier, and (2) the dynamic and heterogeneous neurological disease microenvironment, which is dependent on disease etiology and disease progression, and is variable from patient to patient. Nanotechnology based imaging probes, such as quantum dots (QDs), are thus of interest to study complex changes in the brain and develop cutting-edge imaging tools. QDs have several advantages over traditional probes including tailorable excitation and emission spectra, tailorable surface functionalities, and high photoluminescence and photostability, which are ideal characteristics for *in vivo* imaging. QDs have been utilized in various applications in the brain; however, a systematic evaluation of QD behavior in brain-relevant conditions has not been done. Therefore, we first sought to comprehensively investigate QD colloidal stability, toxicity, and

cellular uptake *in vitro*, *ex vivo* and *in vivo* in the neonatal brain environment. We found QD behavior is highly dependent on surface functionality, and QDs can activate metallothionein detoxification pathways in cells in organotypic whole hemisphere slice cultures. QDs are mainly internalized in the corpus callosum region in microglia, cells that mediate inflammation in the brain. Using multiple biological models in this study also indicated the need for careful consideration of barriers that exist in different study platforms, when investigating nanomedicine behavior in brain microenvironment.

We next sought to utilize QDs to label and visualize extracellular vesicles (EVs). EVs are cell-secreted vesicles that play an important cell-cell communication role and participate in normal and pathological processes. Direct visualization and tracking of EVs is essential to broaden the utility of EVs as biomarkers of injury, however, current labeling techniques fail due to lack of sensitive, specific and robust labeling. We have developed a QD-EV conjugation platform using 4-formylbenzoate (4FB) to 6-hydrazinonicotinate acetone hydrazone (HyNic) click chemistry. We showed this method can be performed under physiological conditions, is universal to EVs coming from different sources, such as human semen fluids and rat brain, and has better resistance to photobleaching compared to commonly used labeling dye. This QD-EV conjugation method also has room for optimization by using catalyst or altering QD:EV ratio. QD-EV conjugates and unconjugated QDs can be easily separated by size exclusion chromatography (SEC). We also show this QD-EV conjugation platform enables high resolution visualization and real-time study of the EV-cell interaction.

In summary, we investigated both fundamental understanding of QD neuroimaging probes in the developing brain and application of QDs for labeling and visualizing EVs. The understanding of

QD behavior and impact in the brain, and subsequent use of QDs to label and trace biological entities represents a promising advancement in the field of bioimaging for neurological disease.

TABLE OF CONTENTS

LIST OF FIGURES	v
LIST OF TABLES	viii
LIST OF MOVIES.....	ix
ACKNOWLEDGEMENTS	x
CHAPTER 1: Introduction	1
1.1 Central nervous system diseases: impact, challenges and needs	1
1.2 Quantum dot imaging probes	2
1.3 Use of QDs in the brain.....	3
1.4 Extracellular vesicles and their medical potential.....	4
1.5 Overview of project chapters	5
CHAPTER 2: Methods	7
2.1 Core-shell CdSe/CdS QD synthesis and characterization	7
2.2 Animal work and ethics statement	11
2.3 OWH slice culture preparation.....	12
2.4 QD dose selection.....	13
2.5 Characterization of QD stability in brain-related biological fluid as a function of surface functionality	13
2.6 Evaluation of QD toxicity in OWH slices as a function of surface functionality and dose by LDH Assay	15

2.7 Evaluation of QD-induced oxidative stress, inflammation, and metal detoxification in OWH slices by RT-qPCR	16
2.8 QD penetration and cellular uptake in OWH slices	18
2.9 Time-lapse imaging of QD cellular and intracellular internalization	20
2.10 BV-2 cell culture	21
2.11 <i>In vitro</i> QD toxicity and cellular uptake in BV-2 cells by MTT assay and confocal microscopy	21
2.12 <i>In vivo</i> QD cellular uptake in <i>mglur5</i> model.....	22
2.13 Isolation of EVs from human semen and rat brain.....	22
2.14 Quantification, size distribution, and purity characterization of EVs	23
2.15 Conjugation of QDs to sEVs or bEVs.....	24
2.16 Characterization of QD-EV conjugates.....	25
2.17 Optimization of QD-EV conjugation	26
2.18 SYTO RNASelect staining and fluorescence imaging of QD-sEV conjugates	27
2.19 Characterization of QD-EV bond stability under biological and storage conditions.....	28
2.20 QD-sEV treatment of <i>ex vivo</i> human vaginal epithelial sheets	28
2.21 Confocal imaging and time-lapse tracking of QD-bEVs on BV-2 cells	29
2.22 Photostability comparison of QD-bEVs and DiI-bEVs	30
2.23 Statistical analysis	31
 CHAPTER 3: Quantum dot cellular uptake and toxicity in the developing brain: Implications for use as imaging probes	 32
3.1 Introduction	32
3.2 Results and discussion.....	33

3.2.1 Physicochemical characterization of core-shell CdSe/CdS QDs	33
3.2.2 Colloidal Stability of QDs in neurophysiologically relevant fluids.	36
3.2.3 Ex vivo QD cellular uptake and time-lapse internalization imaging.	40
3.2.4 QD-induced toxicity, oxidative stress, inflammation and metal detoxification in OWH slices as a function of surface functionality.	45
3.2.5 In vitro QD toxicity and cellular uptake on BV-2 cells.....	50
3.2.6 In vivo QD cellular uptake in mglur5 neuroinflammatory rat model.	52
3.3 Conclusion.....	54
 CHAPTER 4: Quantum dot labeling and visualization of extracellular vesicles	 56
4.1 Introduction	56
4.2 Results and discussion.....	57
4.2.1 Chemistry for QD-EV conjugation	57
4.2.2 Characterization of Purified sEVs and QD-sEV conjugates	59
4.2.3 Visualization, confirmation, and stability of QD-sEV conjugates.....	62
4.2.4 Optimizing QD-EV conjugation by altering QD distribution on EVs and increasing reaction efficiency	64
4.2.5 Investigating bEVs interaction with BV-2 cells through QD-bEV conjugates.....	66
4.3 Conclusion.....	71
 CHAPTER 5: Research Summary	 72
5.1 Quantum dot labeling and visualization of extracellular vesicles.....	72
5.2 Quantum dot cellular uptake and toxicity in the developing brain: implications for use as imaging probes	74

5.3 Nanoparticle-microglia interaction in the ischemic brain is modulated by injury duration and treatment	76
5.4 Governing transport principles for nanotherapeutic application in the brain.....	78
5.6 Extracellular vesicles in human semen modulate antigen-presenting cell function and decrease downstream antiviral T cell responses	81
5.7 Systems-level thinking for nanoparticle-mediated therapeutic delivery to neurological diseases.....	82
APPENDIX A: Supplementary Figures to Chapter 3.....	84
APPENDIX B: Supplementary Figures to Chapter 4.....	98
APPENDIX C: Supplementary Figure to Chapter 5.....	106
BIBLIOGRAPHY.....	107
CURRICULUM VITAE.....	117

LIST OF FIGURES

Figure 1. Surface functionalization and characterization of CdSe-CdS core-shell QDs.	36
Figure 2. Colloidal stability of QDs at 37°C in neurophysiological-relevant fluids.	38
Figure 3. Iba1+ microglia and lysosome uptake of QDs in <i>ex vivo</i> OWH slices.	42
Figure 4. NeuN+ neuron uptake of QDs in <i>ex vivo</i> OWH slices.	45
Figure 5. Dose-dependent toxicity of QD-PEG-OH and QD-PEG-OMe in <i>ex vivo</i> OWH slices.	47
Figure 6. Time-dependent mRNA profiles of QD-induced metallothionein and proinflammatory markers in OWH slices.	49
Figure 7. Toxicity of QDs on <i>in vitro</i> BV-2 cells.	52
Figure 8. QD cellular uptake in P7 rats, 4 h post-administration.	54
Figure 9. Schematic of QD-EV conjugation chemistry	58
Figure 10. Characterization of purified sEVs and QD-sEV conjugates.	61
Figure 11. TEM imaging of QDs, sEVs, and QD-sEVs.	64
Figure 12. Characterization of QD-bEV conjugates.	67
Figure 13. Photostability and imaging of QD-bEVs on BV-2 cells.	70
Figure A1. ATR-FTIR spectra of QD-MPA (orange), QD-PEG-OMe (blue), and QD-PEG-OH (red).	84
Figure A2. Colloidal stability of QDs at 23°C in neurophysiological fluids.	86
Figure A3. Cadmium ion release and QD photoluminescence change over time.	87
Figure A4. QD penetration in OWH slices.	88

Figure A5. pH influence on QD-PEG-OMe stability in aCSF media.....	89
Figure A6. Fraction of Iba1+ cells containing QDs in the corpus callosum region in OWH slices.	89
Figure A7. Cross-sectional views of z-stack confocal images of QDs colocalization with Iba1+ microglia following 24 h incubation in OWH slices.	90
Figure A8. Olig2+ oligodendrocyte uptake of QDs in OWH slices.	91
Figure A9. Time-dependent mRNA profiles of QD-induced anti-inflammatory and oxidative stress markers in OWH slices.	92
Figure A10. Dose-dependent toxicity of QD-MPA in OWH slices by LDH assay.	93
Figure A11. Cellular uptake of QD-MPA on <i>in vitro</i> BV-2 cells.....	94
Figure A12. QD cellular uptake in hippocampus and PVR regions in P7 rats, 4 h post- administration.	95
Figure A13. QD cellular uptake in P7 rats, 24 h post-administration.....	96
Figure B1. Fluorescence imaging of QD colocalization with sEVs after QD-sEV conjugation...98	
Figure B2. Imaging of QD-sEV conjugates on human vaginal tissue.	98
Figure B3. Size distribution of sEVs before and after storing at 4°C for 25 d.	99
Figure B4. 4FB-HyNic bond stability in biological and storage conditions.....	100
Figure B5. Catalysts accelerate HyNic-4FB bond formation.	101
Figure B6. Representative frames of time-lapse imaging of QD-bEVs on BV-2 cells.	103
Figure B7. Cumulative counts of the bEV-cell interaction.....	104

Figure C1. Visualization and quantification of AF700-CD40 distribution in the tumor via immunofluorescence imaging.106

LIST OF TABLES

Table 1. Primer sequences for RT-qPCR.....	17
Table 2. CdSe/CdS QD characterization in 10 mM NaCl.	34

LIST OF MOVIES

Movie A1.	96
Movie A2.	96
Movie A3.	96
Movie A4.	97
Movie A5.	97
Movie B1.	104
Movie B2.	104
Movie B3.	105

ACKNOWLEDGEMENTS

I am grateful for the chance of taking my final exam here. This written paper will not be accomplished without efforts from numerous people. I would love to first thank all my committee members, Dr. Nance, Dr. Holmberg, Dr. Vojtech, and Dr. Gao, to attend my final exam, listen to my research, and give valuable feedback during the past 5 years. First, I would love to thank my PI, Dr. Elizabeth Nance. She is such a generous mentor who is always student-oriented, passionate about neurological researches and loves to motivate people with her inspiration. She not only leads me into the research field, but also fully supports my personal life and outreach interest such as science communication and leadership experience as secretary of WChE. I would love to thank Dr. Holmberg and Dr. Vojtech, they are such great collaborators who I can't ask for more, and always willing to share their expertise in QDs and EVs. Lastly, I would like to especially thank Dr. Gao. I first learned about QDs in his lecture in 2014 when I was an undergraduate exchange student at UW. I did not anticipate QDs would play an important role in my life the next 5 years, but I attribute this lovely coincidence to the beautiful, colorful, and amazing new world of QDs Dr. Gao showed me then.

I would like to shout out to my lab mates, especially graduate students Rick, Chad, Andrea, and Mike they accompany me longest in the lab. As the first generation of Nance lab, we support each other and grow up together from the ground. I thank my team "Spooky Action", which includes 6 lovely undergraduate students Binh, Kate, Olesya, Nina, Jimmy, and Tolu. Without them, I will not be able to proudly present my research here. Sometimes I even consider them as my mentors because of their optimistic attitude about science and life which I always get inspired by. I greatly appreciate all the lab members' efforts on maintaining a healthy, fun, and supportive culture. I feel so beloved in every Friday happy hour in Kate's pub, every lab event, and every time we went to

eat pho. Thank many of you who came to celebrate Chinese New Year with me once a year from 2018 to 2020. Nance lab is truly my family here in Seattle.

Besides the Nance lab, I thank all my collaborators for their generous share of knowledge and chance for doing exciting researches together. I thank Dr. Garden and her postdoc Katie and Ph.D. student Macarena, who I gain a lot of help from about FACS and microglia culturing. I also thank Dr. Andrea McQuate for her providing of neonatal rat for research when we just started our lab.

I want to especially thank my family and my friend. Simon, I won the competition that I defend earlier than you, so now you should acknowledge me as Dr. Zhang in your thesis. One of the greatest gifts I have during graduate school is to meet you and love you. When I look back, I am sure I will miss the years that we got to both work at UW (and can easily meet each other every day on the Garfield Ln because you work in HSB and I work in Benson Hall) and support each other's research. I love all the moments that we discuss science, even we often disagree with each other because I think things experimentally while you think as a statistician. Thank you, mom and dad, for raising me and let me chase my dream without living burden. Mom, you are one of the strongest women I've ever seen in my life. Even though you were diagnosed with cancer many years ago, you are always optimistic and encouraging, which really motivates me whenever I feel down. I thank my best friend Yue Pan (Alice) who share similar interests and opinions of life with me and support all my crazy ideas even from the other side of Earth (she is in Norway now). I thank Engage, where I get to meet a group of scicomm lovers, organize siccomm workshops, and give a public talk about the story of my research. I thank my boxing gym, even though I wasn't able to go in during the pandemic, I had much fun time maintaining healthy and punching out my stress about the graduate school there. I thank many of my friends in the US and back in China. You all make my life in graduate school much much better.

In the end, I would like to thank UW. It is such a beautiful university that I immediately fell in love with the first time I visited. It also provides a supportive and collaborative environment and makes me feel like home as an international student. I thank all the people above, and more and more who I am not listing here. Thank you all for being in my life! Without you all, I may still survive through the graduate school, however, I will not be as happy as I am right now.

CHAPTER 1: Introduction

1.1 Central nervous system diseases: impact, challenges and needs

Central nervous system (CNS) diseases, including Alzheimer disease, Parkinson disease, stroke, traumatic brain injury (TBI), epilepsy, multiple sclerosis, and autistic spectrum disorder (ASD), are a group of neurological disorders that affect the structure or function of the CNS. It is reported that CNS diseases ranked highest in overall disease burden and ranked second highest for cause of death, comprising 16.8% of global mortality in 2015.¹ Economically, the current estimated annual cost to American society for only nine common CNS diseases is nearly 800 billion dollars, and is expected to increase in the following years due to an aging population with greater susceptibility to age-related neurological disorders.² In addition to the cost for treatment, there is also a financial burden of daily care, supervision, assistance, and impact on quality of life from disability, which can hurt the family and people around the patient.

Challenges in treating CNS diseases are also associated with the lowest success rate of drugs to market compared to other therapeutic areas.³ Compared to other organs, the percentage of injected drug dose found in the brain is often below 0.5%,⁴ and is attributed to the inability of most drugs to overcome the strictly regulated blood-brain barrier (BBB).⁵ However, even if a drug does cross this barrier, it must still navigate the tortuous brain microenvironment to reach the diseased site. The drug also needs to specifically uptake into the cell type of interest to achieve the best therapeutic effect. Thus, a therapeutic must be designed with an understanding of the brain environment, especially many transport barriers present in the brain, as well as the delivery method or mechanism itself. Due to the complexity and heterogeneity of the onset and progression of neurological diseases processes that leads to variability from patient to patient, selective, sensitive

and specific probes which serve as diagnosis tools for CNS diseases, can also improve the design of therapeutic interventions. This chapter will outline the use of quantum dots (QDs) as neuroimaging probes, and the potential of these probes in labeling and visualizing extracellular vesicle (EV) transport to solve complex biological questions in the context of CNS disease.

1.2 Quantum dot imaging probes

Nanoscale probes are an emerging cutting-edge tool for both disease process detection and neurological imaging.⁶⁻⁹ Various engineered nanoparticles have shown advantages over conventional contrast agents by providing protection from clearance and demonstrating the ability to overcome barriers to drug delivery, such as the BBB.^{5, 10}

Luminescent semiconductor nanocrystals, or QDs, have especially attracted the interest of researchers due to their tunable excitation/emission spectra and tailorable surface functionality, as well as their robust photostability and efficient luminescence, which make them amendable for *in vivo* animal imaging.¹¹⁻¹³ For biological imaging applications, hydrophobic QDs can be made water soluble by exchange with bifunctional ligands or coating with an amphiphilic segment or group, and variable biomolecules such as antibodies and peptides can later be attached to the QDs to achieve specific labeling and targeting.¹¹ In particular, cadmium selenide (CdSe) QDs are a well-understood, model system that has been widely studied and optimized over the past thirty years, with tunability across the entire visible spectrum. Moreover, recent developments have led to breakthroughs in photostability and QD efficiency, resulting in core-shell QDs with nearly ideal luminescence characteristics.^{14, 15} Because of these advantageous attributes, CdSe QDs have become a common material for use in a variety of different biological applications, including multi-modal imaging and studies of lymphatic basins¹⁶ and live cells.¹⁷

1.3 Use of QDs in the brain

In the context of neurological research, QD applications in the brain have been widely explored in both fundamental research as well as in clinical investigation.¹⁸⁻²⁷ The small hydrodynamic size (10-20 nm) make QDs particularly suitable for neuroscience research, such as in applications of neuron and glia cell labeling and tracking.²⁸ Recently, the potential of QDs in monitoring electrical signals in neurons opened a new and sophisticated field of application,²⁶ which attracts more attention to the use of QDs in the brain. As prospective probes for neurological imaging, however, there are potential concerns for clinical translation, including the toxicity of QDs.²⁹ To address that and further discover the biomedical potential of QD-based probes, investigation into a combination of QD characterization and biological impact is needed, which will be discussed extensively in Chapter 3.

Other than using QDs directly in the brain to gather information based on the interaction between QDs and brain microenvironment, QDs have also been used to label brain-related biological entities. Tagging QDs on peptide or antibodies can be used to visualize and track single dynamic molecular processes of neuronal receptors and transporters over extended periods of time.^{30, 31} QD bioconjugates can also be used to deliver therapeutics to the targeted site in the developing brain,³² or provide a sensitive diagnostic method to characterize the presence or absence of a specific predictive biomarker for CNS diseases.³³ *Via* labeling QDs with larger biological entities such as viruses,^{34, 35} QDs may reveal details of pathogen-host interaction and further explain molecular mechanisms of disease development. Exploring more QDs-labeling method to critical biological entities to the brain, including EVs, can then provide new tools to advance the understanding of neurobiology, which may lead to new therapeutic for CNS diseases.

1.4 Extracellular vesicles and their medical potential

EVs are a variety of small membranous vesicles released from the cells into the extracellular environment and serve as a vehicle carrying diverse molecules, including RNA and proteins.^{36, 37} Along with direct cell-cell contact or transfer of secreted molecules, intercellular transfer of extracellular vesicles has emerged as a third mechanism for critical intercellular communication.³⁶ Although prior literature shows the release of apoptotic bodies during apoptosis,³⁸ the fact that healthy cells also shed vesicles from their plasma membrane was demonstrated recently. EVs from healthy cells can be categorized as exosomes and microvesicles (MVEs) according to the difference of size, morphology, and molecular composition. However, it is hard to distinguish and separate exosomes and MVEs in reality due to their coexistence in biological systems and the limitation of current isolation technology.³⁶ Hence it is often encouraged to study EVs (collectively measuring 40-1000 nm in diameter³⁹) as an entity.

Current interest in EVs has dramatically risen with the increasing knowledge of EVs' ability to interact with recipient cells to deliver cargos from the original cell. It has been found that EVs play an important role in maintaining normal physiological functions, including factor secretion in kidney monitoring and repair,^{40, 41} immune modulation,⁴² and tissue homeostasis.⁴³ EVs have also been shown to play a role in pathological functions, notably in cancer and neurodegeneration.^{39, 44} In the presence of injury, EVs secreted by neurons and reactive glia induce and propagate neuroinflammation processes in several neurological diseases,⁴⁵ including Alzheimer's,⁴⁶ TBI,⁴⁷ and depression.⁴⁸ In addition, the feature of intercellular communication of EVs also make EVs potential biomarkers and pharmacological targets for various diseases.⁴⁹ Since EVs protect their contents from clearance or degradation, cargos in EVs can be transported remotely, such that identification of them could enable a method to monitor of disease progression. According to EVs'

pathological function, it is envisioned to suppress disease progression by interrupting EV-mediated crosstalk, including interfering with EV biogenesis and/or release, EV removal from the circulation, and inhibition of EV uptake by the target recipient cell.⁵⁰ Alternatively, injecting stem cell-derived EVs are proposed to promote tissue regeneration after injury.⁵¹ EVs also have interest as drug delivery vehicles as a “natural” carrier with the potential to circulate without detection by the immune system.⁵² Therefore the ability to visualize EVs could provide significant improvements in understanding EVs as pathological mediators or as therapeutic interventions. The limitations in visualizing EVs, which will be discussed in Chapter 4, necessitate a universal, stable and sensitive approach that can allow for imaging of EVs in their native environments (e.g. *in vivo*). QDs provide a unique platform to tag EVs to better visualize their behavior in tissue and in mediating cell response.

1.5 Overview of project chapters

In **Chapter 2**, we summarize all methods used throughout the thesis.

In **Chapter 3**, we systematically evaluate the behavior of QDs, including their toxicity, stability, and cellular uptake, in *in vitro*, *ex vivo*, and *in vivo* developing brain models. We demonstrate that CdSe/CdS core/shell QD behavior is highly dependent on their surface functionality. We also show that PEG coating on QDs is important for the stability of QDs, and PEGylated QDs induce dose- and time-dependent toxicity in organotypic whole hemisphere (OWH) slices, while activate metallothionein pathways for metal detoxification. We then indicate QDs are dominantly uptaken into microglia. By using various models to investigate QD performance in the brain, we emphasize the importance of taking consideration of biological barriers absence or presence in the testing models, as they are shown to change the behaviors of nanoparticles in the microenvironment.

In **Chapter 4**, we present a click-chemistry based QD bioconjugation method to label and visualize EVs. We demonstrate this labeling method can be generally applied to EVs from various resources, including human semen-derived EVs (sEVs) and rat brain-derived EVs (bEVs), can be stable in biological environments, can be tailored by catalysts or altering QD:EV ratio, and can present ability to real-time visualize EV-cell interaction at high resolution. In addition, we demonstrate the resulting QD-EV conjugates have better resistance to photobleaching compared to organic dye DiI labeled EVs. This QD-EV conjugation may allow further detailed exploration of EV-cell interaction or investigation of therapeutic or pathological target of EVs.

In **Chapter 5**, we summarize all thesis-related research, including other manuscript contributions.

CHAPTER 2: Methods

2.1 Core-shell CdSe/CdS QD synthesis and characterization

Materials and reagents: Cadmium oxide (CdO, $\geq 99.99\%$), selenium ($\geq 99.99\%$), trioctylphosphine oxide (TOPO, 90%), trioctylphosphine (TOP, 97%), hexadecylamine (HDA, 90%), oleic acid (OLA, 90%), 1-octadecene (ODE, 90%), 1-octanethiol ($\geq 98\%$) and 3-mercaptopropionic acid (MPA, $\geq 99\%$) were purchased from Sigma-Aldrich. PEG5000k-methoxy (PEG-OMe, PLS-604), and PEG5000k-hydroxyl (PEG-OH, PBL-8083) were purchased from Creative PEGWorks. Hexanes ($\geq 98.5\%$), toluene ($\geq 99.5\%$), acetone ($\geq 99.5\%$), methanol ($\geq 99.8\%$) and citric acid ($\geq 99.5\%$) were purchased from Fischer Scientific. All reagents were used as received, without further purification.

CdSe core synthesis: CdSe nanocrystal cores were synthesized *via* a modified version of the protocol developed by De Nolf *et al.*⁷⁸ In a typical synthesis, 150 mg cadmium oxide (CdO), 12 g 1-octadecene (ODE), and 1 g oleic acid (OLA) were added to a 100 mL 3-neck flask on a Schlenk line, heated to 110 °C under nitrogen, and degassed for 30 min while stirring. The mixture was then heated to 280 °C under nitrogen and stirred at 600 rpm until clear and colorless. After lowering the temperature to 100 °C, 2 g of hexadecylamine (HDA) and 2 g of trioctylphosphine oxide (TOPO) were quickly added and the mixture was degassed for an additional hour. The flask was then heated to 280 °C under nitrogen, after which a solution of TOP : Se (190 mg of Se dissolved in 4 mL of trioctylphosphine) was rapidly injected. Aliquots were taken as the nanocrystals grew, and ultraviolet-visible (UV-vis) absorption spectroscopy was used to monitor nanocrystal diameter by tracking the position of the $1S_{3/2}1S_e$ excitonic absorption feature.⁵³ Once the desired nanocrystal diameter was achieved, the heating mantle was removed, and the mixture was allowed

to cool. When the temperature of the flask reached 100 °C, 10 mL of toluene was injected in order to facilitate nanocrystal purification. Once cooled to room temperature, the nanocrystal cores were purified by adding antisolvent (ethanol) to the reaction mixture until the point of opalescence, followed by rapid centrifugation, and dispersion of the resulting nanocrystal precipitate in clean toluene – a process which was repeated three times.

Core-shell CdSe/CdS QD growth: Protective CdS shells were grown onto the CdSe nanocrystal cores using a modified version of the protocol developed by Chen *et al.*¹⁴ Prior to shell growth, cadmium oleate was prepared using previously established procedures.⁵⁴ Briefly, 129 mg CdO, 950 µL OLA, and 10 mL ODE were heated to 110 °C and degassed for 45 minutes using standard Schlenk line methods. The mixture was then heated to 280 °C under nitrogen and stirred at 700 rpm until clear and colorless. The resulting cadmium oleate complex was then cooled to 100 °C and degassed for an additional hour prior to being cooled to room temperature and transferred to a nitrogen-filled glove box for storage. Core-shell CdSe/CdS QDs were then prepared by adding 200 nmol of CdSe nanocrystal cores to a mixture of 2.5 g ODE and 2 g HDA in a 100 mL flask attached to a Schlenk line. The mixture was heated to 60 °C under nitrogen and degassed for 1 h while stirring at 850 rpm, followed by heating under nitrogen to 120 °C and degassing for an additional 20 min. A syringe pump was then loaded with two separate syringes: one containing cadmium oleate dissolved in ODE, and one containing 1-octanethiol dissolved in ODE. For the 3.4 nm-diameter CdSe cores used in this study, 8.7 mL of cadmium oleate complex mixed with an additional 0.8 mL of ODE were loaded into one syringe, and 300 µL of 1-octanethiol mixed with 9.2 mL of ODE were loaded into the other syringe. To facilitate shell growth, the dispersion of nanocrystal cores was heated under nitrogen to 290 °C at a rate of ~ 14 °C min⁻¹, and once the solution temperature reached 200 °C, the syringes containing the cadmium and sulfur precursors

were slowly injected at a rate of 2.3 mL h⁻¹ using the syringe pump. After completion of the injection, the dispersion was held at 290 °C for an additional 30 min. 2 mL of OLA were then rapidly injected, and the dispersion was cooled to 200 °C and left to anneal at that temperature for 1 h. After cooling to room temperature, the core–shell QD dispersion was purified several times by the addition of ethanol, followed by centrifugation and dispersion of the precipitated QDs into clean toluene.

Core–shell CdSe/CdS QD surface functionalization: Core–shell CdSe/CdS QDs were functionalized *via* ligand exchange procedures modified from Zhang *et al.*⁵⁵ using three different target surface chemistries, including 3-mercaptopropionic acid (MPA), PEG5000k-methoxy (PEG-OMe), and PEG5000k-hydroxyl (PEG-OH). In a typical synthesis, QD surface functionalization and transfer to aqueous media was achieved by dissolving either 70 µL MPA, 120 mg PEG-OMe, or 120 mg PEG-OH into a mixture of 300 µL deionized water and 1 mL methanol. The ligand solution was then adjusted to a pH of ~12 by the gradual addition of 40% NaOH. ~15 nmols of core–shell CdSe/CdS QDs dispersed in 500 µL chloroform (for MPA functionalization) or hexanes (for PEG-OMe and PEG-OH functionalization) were added to the 1.3 mL ligand solution along with a stir bar. The solution was then stirred at 1000 rpm for 30 min, followed by the addition of 1 mL deionized water. The solution was then left to stir for another 20 min. The organic and aqueous phases were then separated, and the functionalized QDs (now dispersed in the aqueous phase) were collected. MPA-functionalized QDs (QD-MPA) were purified *via* the addition of acetone, followed by centrifugation, dispersion of the precipitated QDs into deionized water, and filtration through a 0.2 µm nylon filter. For PEG-OMe and PEG-OH functionalized QDs (QD-PEG-OMe and QD-PEG-OH), the dispersions were filtered through a 0.2 µm nylon filter, neutralized with citric acid, and placed under vacuum using a rotary evaporator to

remove excess hexanes and methanol. The optimized syntheses outlined in the preceding sections were carried out numerous times to produce the large quantities of functionalized QDs necessary for the *in vitro*, *ex vivo*, and *in vivo* studies.

QD Characterization: QD absorption characteristics were determined by collecting UV-vis extinction spectra with an Agilent Cary 60 UV-vis spectrophotometer. Care was taken such that all absorbance values recorded were below 1.0. Nanocrystal morphology was evaluated *via* transmission electron microscopy (TEM) using a FEI Tecnai G2 F20 Supertwin TEM operating at an accelerating voltage of 200 kV. ImageJ software was used to determine nanocrystal size distributions. Photoluminescence characteristics were determined for each sample of functionalized CdSe/CdS QDs using a PerkinElmer LS-55 fluorescence spectrometer. Absolute photoluminescence quantum yield measurements were carried out using a Hamamatsu C9920-12 integrating sphere and verified using a rhodamine 640 perchlorate reference dye (Exciton, Inc.). QD particle concentrations were determined by measuring the position and intensity of the $1S_{3/2}1S_e$ excitonic absorption feature.⁵⁴ The hydrodynamic diameter and zeta potential (ζ -potential) of each of the functionalized core-shell CdSe/CdS QD samples were obtained by dynamic light scattering (DLS) using a Zetasizer Nano DLS system (Malvern Instruments, Malvern, UK). For baseline size and ζ -potential measurements, samples were diluted 1:1000 in 10 mM sodium chloride (NaCl), pH 7.4. Size and polydispersity (PDI) measurements were performed at 23°C at a scattering angle of 173°, and ζ -potential was determined by laser Doppler anemometry (LDA). The measured hydrodynamic diameter and QD surface charge from different batches were then combined to determine average values for each surface functionality. FTIR spectra for MPA, PEG-OMe, and PEG-OH-functionalized CdSe/CdS QDs were obtained using a Bruker Alpha IR spectrometer equipped with a platinum attenuated total reflectance (ATR) accessory and a diamond crystal

sampling module. Prior to FTIR analysis, the QD-PEG-OMe and QD-PEG-OH samples were placed under vacuum in a rotary evaporator until completely dry, and then were re-dispersed into chloroform. The MPA-functionalized QDs were purified *via* the addition of acetone, followed by centrifugation and dispersion of the precipitated QDs into methanol. Spectra were recorded under a nitrogen atmosphere after forming thin films of material on the diamond ATR crystal. QD thin films were formed by drop-casting the chloroform or methanol particle dispersions directly onto the surface of the ATR crystal and allowing the solvents to evaporate completely.

2.2 Animal work and ethics statement

The animal studies were performed in strict accordance with the NIH guidelines for the care and use of laboratory animals (NIH Publication No. 85-23 Rev. 1985). All animal procedures were approved by the Institutional Animal Care and Use Committee of the University of Washington, Seattle, Washington. For healthy newborn pups, time-mated pregnant female Sprague-Dawley rats (virus antibody free CD® (SD) IGS, Charles River Laboratories) were purchased and arrived on estrous day 17 (E17). For pups with neuroinflammation, we used a transgenic rat model generated by Sigma Advanced Genetic Engineering (SAGE) labs through knocking out of the metabotropic glutamate receptor (*mglur5*) on a SD background. *mglur5* knockout (KO), wild-type (WT), and heterozygous (HET) pups were bred by HET x HET crosses. All dams used in these studies were housed individually and allowed to acclimate to their environment for a minimum of five days prior to delivering (E22). Day of birth was defined as postnatal day (P) 0 (P0). Litters containing both sexes were cross-fostered and culled to 12 animals on P4, and genotypes for *mglur5* pups were determined by real-time PCR (Bio-Rad) on P4. Each litter was housed under standard conditions with an automatic 12-h light/dark cycle, temperature range of 23-26°C, and access to

standard chow and autoclaved tap water *ad libitum*. Pups were checked daily for health. Both genders were used for all studies.

2.3 OWH slice culture preparation

OWH slices were prepared based on modification to a previously published paper to maintain *in vivo*-like conditions.⁵⁶ OWH slices were prepared from healthy P14 newborn SD rats. Neonatal rats were decapitated under aseptic conditions after euthanasia by a pentobarbital overdose > 100 mg/kg. The brain was quickly removed under sterile conditions, dissected into two hemispheres, and sectioned immediately into 300- μ m-thick brain slices using a McIlwain tissue chopper (Ted Pella, Inc., USA). For each hemisphere, six consecutive slices at the level of bregma were separated in dissection medium (3.2 g glucose/500 mL HBSS, 1% of penicillin). The separated brain slices were transferred onto sterile 30-mm-diameter, 0.4- μ m-pore-size cell culture membrane inserts (Millipore, Billerica, MA) in six-well tissue culture plates. To evaluate slice viability throughout the experimental window, supernatant aliquots were obtained to measure lactate dehydrogenase (LDH), as described below. For the LDH assay, cellular uptake, and time-lapse imaging studies, one OWH slice was placed on each membrane insert; for the quantitative reverse transcription polymerase chain reaction (RT-qPCR) study, three OWH slices were placed on each membrane insert and the volume of media was adjusted accordingly. Each well was pre-filled with 1 mL of slice culture medium (200 mL MEM, 200 mL HBSS, 4 mL Glutamax, and 1% penicillin) pre-warmed to 37°C. The slices were maintained in a sterile incubator (ThermoFisher) at 37°C with constant humidity, 95% air, and 5% CO₂ overnight and randomized to treatment groups prior to each study.

2.4 QD dose selection

We estimated the dose used in *in vitro* and *ex vivo* studies based on the dose of nanoparticles that would be directly exposed to the brain after intravenous (i.v.) injection *in vivo*. There is limited published data on QD biodistribution in the neonatal rat brain. Based on previous research with other sub-40-nm diameter nanoparticles,⁵⁷⁻⁵⁹ brain uptake corresponds to a nanomaterial dose ranging from $\sim 0.2 \mu\text{g}$ to $30 \mu\text{g}$, depending on the material and method of quantification. The selection of QD dose of $0.01 - 1 \mu\text{M}$ corresponds to $\sim 0.12 - 12 \mu\text{g}$, which is in this range. Therefore, the doses used in this study represent an *in vivo* exposure level for investigation in *in vitro* and *ex vivo* environments.

2.5 Characterization of QD stability in brain-related biological fluid as a function of surface functionality

Time-dependent stability: QD-MPA, QD-PEG-OH and QD-PEG-OMe were diluted by 1x phosphate buffered saline (PBS) or artificial cerebrospinal fluid (aCSF) (119 mM NaCl, 26.2 mM NaHCO₃, 2.5 mM KCl, 1 mM NaH₂PO₄, 1.3 mM MgCl₂, 10 mM glucose, 2.5 mM CaCl₂, bubbled with CO₂) to form a $0.1 \mu\text{M}$ suspension. The aCSF was adjusted to pH 7.4 before adding the QDs. The suspended particles were incubated at 23°C or 37°C for up to 24 h. 1 mL samples of suspension were measured by DLS at 0, 4, and 24 h to obtain particle hydrodynamic diameter (n=3) and assess time-dependent aggregation.

pH-dependent stability: 0.1x aCSF (aCSF:DI water = 1:9) was adjusted to pH 2, 4, 7, and 9 by titrating with 0.2M HCl. QD-PEG-OMe particles were diluted into 0.1x aCSF with different pH values to a final concentration of $0.1 \mu\text{M}$. The suspended particles were incubated at 37°C for up to 24 h. 1-mL samples of suspension were measured by DLS at 0 and 24 h to obtain particle

hydrodynamic diameters (n=3). The pH of each QD suspension was measured at 0 h and 24 h to validate no change in pH during the study.

QD aggregation kinetics: We explored the role that Ca^{2+} ions play on the initial QD aggregation kinetics in aCSF at 37°C, based on previously published work that shows Ca^{2+} as a key factor in colloidal stability of polystyrene particles.⁶⁰ QD-MPA, QD-PEG-OH and QD-PEG-OMe were diluted to 0.1 μM by 0.5 mM, 1 mM, and 4 mM CaCl_2 , respectively. The hydrodynamic diameter of the suspended particles was tested in triplicate by DLS at 23°C or 37°C with 200 ten-second measurements over the course of 33 min. Briefly, aCSF was brought to 37°C inside the DLS instrument and allowed to equilibrate for 3 min. QDs were then quickly added and mixed by pipette to achieve a concentration of 0.1 μM . Hydrodynamic diameter measurements were taken every 10 s over a period of 8 min 20 s (50 total measurements). 1 M CaCl_2 solution was then quickly added to achieve a 0.5 mM CaCl_2 concentration, followed by an additional 50 measurements. This process was repeated for successive CaCl_2 concentrations of 1, 2, 3, 4, 5, 6, 8, and 10 mM.

QD photoluminescence stability: QD-MPA, QD-PEG-OH and QD-PEG-OMe particles were diluted by aCSF to form 0.1 μM suspensions and incubated at 37°C for up to 24 h. The aCSF was adjusted to pH 7.4-7.6 before adding the QDs. Photoluminescence spectra of QD suspensions were measured at 0 h, 1 h, 4 h and 24 h using a SpectraMax M5 Microplate Reader (Molecular Devices) with a 450 nm excitation wavelength, and the photoluminescence intensity was then plotted as a function of time.

QD dissolution stability: QD-MPA, QD-PEG-OH and QD-PEG-OMe particles were diluted by aCSF to form 0.1 μM suspensions and incubated at 37°C for up to 24 h. The aCSF was adjusted to pH 7.4-7.6 before adding the QDs. At 0 h and 24 h, 1 mL of QD suspension was transferred to an Amicon Ultra-2 Centrifugal Filter Unit (50 kD) and centrifuged at 3,000 $\times g$ for 10 min in order

to filter out the QDs. The fluid that passed through the filter was then collected for inductively coupled plasma mass spectroscopy (ICP-MS) analysis using a NexION 2000 ICP Mass Spectrometer (PerkinElmer) to measure the quantity of Cd²⁺ ions released into the suspension.

2.6 Evaluation of QD toxicity in OWH slices as a function of surface functionality and dose by LDH Assay

QDs were added to brain slices in a dose-dependent manner (0.01, 0.1 and 1 μM) for 24 h, and viability of each whole brain slice was evaluated. Media beneath pre-cut, 300-μm-thick OWH slices on membrane inserts was changed to fresh, pre-warmed slice culture medium. The QD-MPA, QD-PEG-OH and QD-PEG-OMe were diluted to 1, 0.1, and 0.01 μM by 1xPBS, and 100 μL of suspended particles were carefully dropped onto each slice. Slices without QD treatment served as the non-treated control group (NT), and slices receiving 1% Triton X-100 were considered as the 100%-cell-death, maximum-release group (Tx). The slices were then incubated at 37°C with constant humidity, 95% air, and 5% CO₂ for 24 h. At the end of the exposure time, fresh medium was replaced, and supernatant aliquots were taken at 0, 1, 2, 4, 8, and 24 h timepoints. NT and Tx groups were run for each QD-treated study. Supernatants at each time point were utilized to determine cell death with an LDH assay kit, according to manufacturer instructions (Cayman, USA). The percentage of LDH released in each whole-hemisphere brain slice was quantified by measuring the absorbance intensity of the formazan reactive product, subtracting the intensity of NT groups, and normalizing by the intensity of Tx groups. (n=3)

$$\% \text{Cytotoxicity} = \% \text{LDH release} = \frac{\text{Experimental release}}{\text{Maximum release (Tx)}} \times 100\%$$

2.7 Evaluation of QD-induced oxidative stress, inflammation, and metal detoxification in OWH slices by RT-qPCR

Brain slices were treated with 0.1 μM QDs for 1 h, 6 h, and 24 h, and evaluated by RT-qPCR for mRNA expression of inflammatory cytokines, oxidative stress, and metal detoxification. Each experiment was done on three to six 300- μm -thick OWH slices in order to obtain enough RNA (>250 ng/ μL) post-extraction. P14 brains were sliced as described above, and three OWH slices containing hippocampal regions were placed on each membrane insert. The media beneath brain slices and membrane inserts was changed to fresh, pre-warmed slice culture medium prior to addition of QDs. The QD-MPA, QD-PEG-OH and QD-PEG-OMe were diluted to 0.1 μM by 1xPBS and 300 μL of suspended particles were carefully dropped on top of each slice. The NT control group was prepared using 300 μL of 1xPBS in place of colloidal QD particles. At the end of the exposure time, slices were washed with 300 μL of 1xPBS, removed from the culture dish, collected in *RNAlater* (Invitrogen) and stored at -80°C . The RNA extraction, cDNA reverse transcription, qPCR assay and analysis were done following MIQE guidelines.⁶¹ RNA extraction was performed using TRIzol (Invitrogen) and chloroform (Sigma). After thawing the slices, the *RNAlater* was removed and 1 mL TRIzol was added to the slices. The slices were homogenized using a Pasteur pipet, and 0.2 mL chloroform was added per 1 mL TRIzol to separate RNA, DNA, and proteins. The RNA phase was collected, mixed with isopropyl alcohol (Honeywell) and centrifuged for precipitation, and washed with 75% ethanol. The RNA concentration was measured by using a NanoDrop instrument (ThermoFisher), and only RNA samples with A_{260}/A_{280} ratio above 1.8 and A_{260}/A_{230} ratio above 1.9 were used for the next step. Single-stranded complementary DNA (cDNA) was reverse-transcribed from 2 μg total-RNA-per-sample with the High-Capacity cDNA Reverse Transcription Kit (Applied Biosystems) according to manufacturer

tumor necrosis			CCT CAG CCT CTT CTC	GGA ACT TCT CCT CCT
factor	TNF- α	NM_012675.3	ATT C	TGT T
			GGA GAC TTC ACA GAG	GCC ATT GCA CAA CTC
interleukin 6	IL-6	NM_012589.2	GAT AC	TTT
transforming				
growth factor,			GAA CCA AGG AGA CGG	GGG ACT GAT CCC ATT
beta 1	TGF- β 1	NM_021578.2	AAT AC	GAT TT
			CGC ACC CGG TTA CTA	GCA TGA ATT CCA GCT
caspase 3	Casp-3	NM_012922.2	TTC	TGT G
BCL2 associated			GCT ACA GGG TTT CAT	CCA TGT TGT TGT CCA
X	BAX	NM_017059.2	CCA	GTT C
			ACG CTG TCA TCG ATT	GGC CTT GTA GAC ACC
interleukin 10	IL-10	NM_012854.2	TCT	TTT
			TTC GAC AGT GAG GAG	GAT GCT GCT GTG AGA
interleukin 1 beta	IL-1 β	NM_031512.2	AAT G	TTT G
metallothionein 1	Mt1	NM_138826.4	CACCGTTGCTCCAGATT	AGCAGCAGCTCTTCTTG
metallothionein				
2A	Mt2A	NM_001137564.1	CAGCGATCTCTCGTTGATGAGCAGGATCCATCTGTG	
metallothionein 3	Mt3	NM_053968.3	TCCTACTGGTGGTTCCT	GCACACTTCTCACATCCT

2.8 QD penetration and cellular uptake in OWH slices

Antibody stains were utilized to evaluate co-localization of QDs in neurons, microglia, and oligodendrocytes in OWH brain slices. Media beneath pre-cut 300- μ m-thick brain slices on

membrane inserts was changed to fresh, pre-warmed slice culture medium prior to QD addition. To study QD penetration into OWH slices, QDs were diluted to 1 μM by 1xPBS, and 100 μL of suspended particles were carefully dropped on top of each slice. To evaluate cellular uptake, QD-MPA, QD-PEG-OH and QD-PEG were diluted to 0.1 μM by 1xPBS, and 100 μL of suspended particles were carefully dropped on top of each slice. After incubating the slices with QDs at 37°C with constant humidity, 95% air, and 5% CO₂ for 24 h, the slices were fixed by 4% PFA or formalin for 1 h. Slices were then washed with 1xPBS twice. Each brain slice was carefully cut out of the surrounding membrane using forceps and scalpel. To assess QD penetration, slices were imaged using a Nikon A1 confocal microscope (Nikon Instruments Inc, USA) at 20x magnification with z-stack at 5- μm -per-step, and presented in 3D-projection view. To assess QD cellular uptake, slices were stained with primary antibodies for neurons (NeuN, Abcam ab190195, USA), microglia (Iba1, Wako 019-19741, USA), and oligodendrocytes (Olig2, Abcam ab109186, USA), followed by Alexa Fluor 488 secondary antibody (Life Technologies, USA) and DAPI for cell nuclei. Briefly, slices were incubated with 500 μL primary antibody for 6 h with 3% TritonX and 6% serum, followed by 500 μL secondary antibody for 2 h with 3% Triton X. Z-stack images at 40x and 60x were taken using a Nikon A1 confocal microscope, and maximum-intensity images were formed in regions of interest, including the cortex, corpus callosum, and hippocampus.

Image analysis was performed in order to quantify the fraction of microglia cells containing QDs in each organotypic brain slice. Brain slices were treated with QDs and stained using anti-Iba1+ for microglia, as described above, with three slices per QD type. For each slice, 2x2 confocal tile-scan images were acquired at 40x magnification, in three regions of interest per slice, for each of the nine slices. Iba1+ cells in the corpus callosum were counted, and Iba1+ cells colocalized with QD+ signals were considered to be QD-containing microglia.

2.9 Time-lapse imaging of QD cellular and intracellular internalization

Time-lapse imaging of QD internalization into microglia in organotypic brain slices was carried out using a Nikon A1 confocal microscope. In preparation for live tissue staining, each brain slice was carefully cut out of the surrounding membrane using forceps and scalpel, and transferred to a 6-well plate with staining solution. To stain the cells, brain slices were incubated with 500 μ L FITC CD11b (BioLegend, USA) at 1:200 ratio in staining media (125 mL HBSS, 250 mL MEM, 125 mL horse serum, 5 mL GlutaMAX, 5 mL penicillin) for 6 h at 37°C, 5% CO₂ and 40% humidity in the dark. After incubation, slices were gently washed twice in staining media. 0.5 μ M QD-MPA, QD-PEG-OH, and QD-PEG-OMe were dropped on an uncoated glass-bottom microwell dish (MatTek Corp., USA), and the brain slice was immediately placed on top of the QD solution and imaged. Time-lapse imaging was carried out in an environmental chamber at 37°C and 5% CO₂. Prior to imaging, the environmental chamber was pre-equilibrated for 30 min. The corpus callosum was located, and images were acquired every 10 min at 40x for 3 h and compiled into video format.

To evaluate QD intracellular internalization, OWH slices were first incubated with 300 μ L LysoTracker (ThermoFisher) on the membrane insert and 1 mL beneath the insert at 1 μ M to stain lysosomes. After incubating for 1 h at 37°C, 5% CO₂, and 40% humidity in the dark, slices were gently washed and removed from the membrane. 1 μ M QD-PEG-OH and QD-PEG-OMe were dropped on an uncoated glass-bottom microwell dish (MatTek Corp., USA), and the brain slice was immediately placed on top of the QD solution and imaged. Time-lapse images or z-stack images at 40x were taken every 2-30 min using a Nikon A1 confocal microscope at the corpus callosum region. Maximum-intensity images were formed from the z-stack images.

2.10 BV-2 cell culture

The murine microglia cell line BV-2 was purchased from ATCC (CRL-2469). BV-2 cells were cultured in high-glucose DMEM supplemented with 10% FBS, 1% glutamine, and 1% 100U/mL penicillin-streptomycin at 37°C in a 5% CO₂ atmosphere. After reaching 70-80% confluency, BV-2 cells were passaged and seeded in a new plate. Media was changed every two days.

For studies in Chapter 4, after reaching 70-80% confluency, BV-2 cells were passaged and 200,000 BV-2 cells were seeded in 35 mm poly-D-lysine coverslip bottom imaging dishes (Corning) with 2 mL cell culture media.

2.11 *In vitro* QD toxicity and cellular uptake in BV-2 cells by MTT assay and confocal microscopy

10,000 BV-2 cells were seeded in 96-well plates and cultured for two days prior to the experiment (n=3 wells per experimental group). Once cells reached 70% confluency, 0.01 μM QD-MPA, QD-PEG-OH, QD-PEG-OMe or 1xPBS were added to cells and incubated at 37°C and 5% CO₂ for 1, 2, 4, 6, and 24 h. The 0 h time point represents a baseline of only BV-2 cells, without the addition of QDs. At each time point, MTT (3-(4,5-dimethylthiazol-2-yl)-2,5-diphenyltetrazolium bromide) assay (ThermoFisher) was performed on 1 plate of cells according to manufacturer instructions to assess cell viability. Additionally, separate plates of cells had 4% formaldehyde added for fixation and staining. Staining of Iba1⁺ was performed with the above-mentioned primary and secondary antibodies. Stained BV-2 cells were imaged with a Nikon A1 confocal microscope at 10x magnification.

2.12 *In vivo* QD cellular uptake in *mglur5* model

Newborn *mglur5* KO, and age-matched, litter-matched WT rats were systemically intraperitoneal (i.p.) administrated 25 mg/kg of QD-PEG-OH on P7 (n=3 pups per group). Animals were euthanized at 4 h or 24 h post-administration and perfused with 1xPBS. Half of the brain was fixed in formalin for immunohistochemistry (IHC). Staining of Iba1 was performed with the above-mentioned primary and secondary antibodies. Z-stack images at 40x were taken with a Nikon A1 confocal microscope, and maximum-intensity images were formed in regions of interest, including the cortex, corpus callosum, hippocampus, and periventricular region (PVR), similar to the OWH slice study.

2.13 Isolation of EVs from human semen and rat brain

sEVs: sEVs were isolated based on published paper.⁶² Semen samples were obtained from this clinic or from the University of Washington Male Fertility Program. Written informed consent was obtained from each donor. All protocols were approved by the Institutional Review Boards of the University of Washington and the Fred Hutchinson Cancer Research Center (IR file numbers 5690 and 4323). Seminal plasma was separated from collected semen samples by a series of centrifugation followed by filtration through a 0.22 μ m syringe filter. sEVs were purified by ultracentrifugation over sucrose cushions. The 30% and 25% sucrose cushions containing the EV fraction were pooled and washed by centrifugation through an Amicon Ultracel 100 kD cellulose centrifugal filter and concentrated to a final 425 μ L-3.2 mL. To deplete proteins in sEVs for later QD-sEV conjugation, qEV column (iZon) was used to further purify sEVs.

bEVs: This study was performed in strict accordance with the recommendations in the Guide for the Care and Use of Laboratory Animals of the National Institutes of Health as mentioned above

in the section “Animal work and ethics statement”. The ordering, housing, and handling of animals are also described above. P14-16 healthy SD rats were decapitated after euthanasia by a pentobarbital overdose $> 100 \text{ mg kg}^{-1}$. Brains were frozen at -80°C until bEV extraction.

bEVs were isolated from the whole rat brain tissue based on adaptations from a published protocol.⁶³ Frozen rat brain was sliced on ice to generate 2-3 mm wide sections of brain. The cut tissue was transferred while partially frozen to a 50 mL tube containing 75 U/mL of collagenase type 3 (Worthington Biomedical) in Hibernate-E at a ratio of 800 μL per 100 mg of brain. The tissue was incubated in a water bath at 37°C for a total of 20 min, with a mix of gentle inversion and gentle pipetting during the incubation. The tissue was returned to ice immediately after incubation and PBS protease inhibitor containing EDTA (PI, Sigma) and PhosSTOP (PS, Sigma) were added to tissue homogenate to a final concentration of 1X. The dissociated tissue was spun at 300xg for 5min at 4°C , following transfer of the supernatant to a fresh tube and spun at 2000xg for 10 min at 4°C . Then the supernatant was spun at 10,000xg for 30 min at 4°C . The collected supernatant was further purified through a qEV size exclusion chromatography (SEC) column (iZon) following vendor specifications. Fractions (f) 5-15 were collected for characterization.

2.14 Quantification, size distribution, and purity characterization of EVs

Nanoparticle Tracking Analysis (NTA): Isolated EVs quantification and size were determined by NanoSight NS300 (Malvern Panalytical). EVs were gently vortexed and serially diluted to a concentration that allow 20-50 particles/frame in NanoSight. Each sample analysis was conducted for 60 s using NanoSight automatic analysis settings and were evaluated in triplicate.

EV Purity Analysis: The purity of isolated EVs was determined based on accepted EV concentration/protein concentration ratio.⁶⁴ The EV concentration was determined by NTA as

described above, and the protein concentration in the EV samples was measured by the bicinchoninic acid assay (BCA assay) (ThermoFisher). A simple calculation was conducted to a final unit of particle/ μg and the calculated ratio was compared with the standard set by the literature.⁶⁴

2.15 Conjugation of QDs to sEVs or bEVs

QDs functionalized with PEG-NH₂ (QD-PEG-NH₂) (ThermoFisher) were conjugated to EVs *via* a modified version of a previously published protocol,³⁴ as outlined in Figure 1. Briefly, 8 μM QD-PEG-NH₂ was quickly mixed with 1.25 mg Sulfo-S-4FB (TriLink BioTechnologies) in 1xPBS to make a 500 μL mixture and incubated for 2 h at room temperature to modify 4FB ligand on QDs (QD-4FB). 6×10^{12} EVs were quickly mixed with 0.5 mg Sulfo-S-HyNic (TriLink BioTechnologies) in 1xPBS to make a 700 μL mixture and incubated for 2 h at room temperature to modify HyNic ligand on EVs (sEV-HyNic). After incubation, QD-4FB was purified by NAP-5 column (GE Healthcare) following manufacturer instruction to remove excess unreacted Sulfo-S-4FB. EV-HyNic was purified by Amicon 100 kD centrifugal filter unit (Millipore) at 3,000xg for 30 min (sEV) or Amicon 50 kD centrifugal filter unit (Millipore) at 3,000xg for 15 min (bEV) to remove excess Sulfo-S-HyNic (Millipore Sigma). Purified QD-4FB and EV-HyNic was mixed and reacted for 2 h at room temperature. After incubation, QD-EVs were separated from unconjugated QD-4FB by qEV SEC column (iZon). To identify QD-EV conjugate containing fractions, both QD-EVs and QD-4FB were excluded through qEV columns and f1-30 were collected, then fluorescence signal was measured at 585 with excitation at 405 nm. When a higher concentration of final QD-EVs were needed, Amicon 50 kD centrifugal filter units (Millipore) were used to concentrate the collected fractions at 3,000xg for 30 min.

2.16 Characterization of QD-EV conjugates

Characterization of QD-4FB by DLS: Modification of 4FB on the QDs was confirmed by a zeta potential shift measured by DLS, based on a previous literature.³⁴ Hydrodynamic particle size and zeta potential of both QD-PEG-NH₂ before modification and QD-4FB after modification and purification were determined by DLS.

Characterization of EV-HyNic by UV-vis Spectroscopy: Modification of HyNic on the EVs from both sEVs and bEVs was confirmed by the presence of an absorbance bond of 4FB-HyNic measured by UV-vis spectroscopy based on a previous paper.³⁴ Briefly, 125 μ L EV-HyNic was mixed with 1xPBS to make a final 300 μ L suspension, and 0.3 mg Sulfo-S-4FB was mixed with 1xPBS to make a final 300 μ L 4FB suspension. Half of the EV solution and half of the 4FB solution were mixed well, and another 150 μ L of 1xPBS was added into EV-HyNic and 4FB solution, respectively, to make a final 300 μ L. The 3 samples and 1xPBS were added to 96-well plate in triplicate with 95 μ L in each well, and the absorbance of the 4FB-HyNic bond was measured every 5 min at 354 nm by the SpectraMax M5 Microplate Reader (Molecular Devices), up to 30 min.

Characterization of QD-EV by TEM: Preparation for TEM analysis was done with small modification of a described method.⁶⁵ In brief, EV samples were mixed with an equal volume of 4% PFA and deposited by airfuge onto Formvar/Carbon coated EM grids (Ted Pella). Samples were contrasted and embedded by treatment with uranyl-oxalate solution (Electron Microscopy Services) for 5 min, followed by methyl-cellulose-uranyl-acetate (Sigma) on ice for 10 min.

Characterization of the Hydrodynamic Size and Zeta Potential: The size and size distribution of EV-HyNic and QD-EVs were characterized by NanoSight, as described above. The zeta potential of EV-HyNic and QD-EVs were characterized by DLS in 1xPBS.

Characterization of the Fluorescence Spectra: The fluorescence intensity of 200 μL 0.8 nM QD-PEG-NH₂ and 200 μL QD-sEV conjugates were measured every 5 nm from 400 nm to 700 nm using a Cytation 3 Imaging Reader (BioTek). The intensities were normalized to the highest value.

Calculation of QD-EV Labeling Efficiency: The QD-EV labeling efficiency was characterized by the percentage of QDs remaining in QD-EV conjugates and the percentage of EVs remaining in QD-EV conjugates. A QD-PEG-NH₂ calibration curve was made by measuring the fluorescence at 585 nm for various QD concentration. By measuring the final QD-EV conjugates fluorescence at 585 nm, the concentration of QDs retained in the conjugates were determined and the percentage was calculated through $\% \text{QDs retained} = \frac{\text{QDs in conjugates}}{\text{Input QDs}}$. The amount of the EVs retained in QD-

EV conjugates were quantified by NTA and the percent of EVs retained was calculated through $\% \text{EVs retained} = \frac{\text{EVs in conjugates}}{\text{Input EVs}}$. The final average QD:EV ratio in QD-EV conjugates was

estimated through $\text{QD:EV} = \frac{\text{QDs in conjugates}}{\text{EVs in conjugates}}$.

2.17 Optimization of QD-EV conjugation

Optimization of QD Distribution on EVs by Altering Initial QD:EV Ratio: QD-sEV conjugates were made in varying ratios of QD to sEVs: 40:1, 70:1, and 100:1. 5 μL 8 μM QD-PEG-NH₂ was reacted with 0.5 mg Sulfo-S-4FB (QD-4FB1) and 12.5 μL 8 μM QD-PEG-NH₂ was reacted with 1.25 mg Sulfo-S-4FB (QD-4FB2) for 2 h. 6×10^{12} sEVs were mixed with 0.5 mg Sulfo-S-HyNic as described above. After NAP-5 column purification of QD-4FB, 500 μL QD-4FB1 was mixed with 500 μL of sEV-HyNic (40:1), 350 μL QD-4FB2 was mixed with 500 μL of sEV-HyNic and 150 μL of 1xPBS (70:1), and 500 μL QD-4FB2 was mixed with 500 μL of sEV-HyNic (100:1).

After reaction, QD-sEV conjugates were imaged by TEM as above to determine the distribution of QDs on sEVs.

Optimization of 4FB-HyNic Reaction Efficiency by Catalysts: 3,5-diaminobenzoic acid (3,5-DABA) and 2-amino-5-methylbenzoic acid (5-MA) were tested as catalyst for hydrazone formation.⁶⁶ 3,5-DABA and 5-MA were dissolved in DMSO to 500 mM and 50 mM. 1.25 mg Sulfo-S-4FB (final concentration 3.58 mM) and 0.5 mg Sulfo-S-HyNic (final concentration 1.27 mM) were mixed in 1 mL 1xPBS, and immediately distributed to 50 uL/well in a 96-well plate for baseline absorbance at 354 nm by a UV-vis spectrophotometer. 3,5-DABA and 5-MA were quickly mixed in the sample to make a final 10 mM, 5 mM or 1 mM catalyst concentration. The absorbance at 354 nm was monitored every 10 min for 3 h. In addition, effect of pH was tested by changing the 1xPBS pH to 7.4, 6.89, and 6.09 by adding 2 mM HCl prior to addition of Sulfo-S-4FB or Sulfo-S-HyNic. The pH was measured by a pH meter (Fisher). When making QD-sEV conjugates using catalysts, 5-MA was quickly added into the mixture of QD-4FB and sEV-HyNic to make a final 1 mM concentration at the start of 2 h QD-EV reaction. After incubation, Amicon 100 kD centrifugal unit was used to filter out excess catalysts.

2.18 SYTO RNASelect staining and fluorescence imaging of QD-sEV conjugates

QD-sEV conjugates were mixed with 1 mM RNASelect Green Fluorescent Cell Stain (ThermoFisher) at a ratio of 1 μ L RNASelect stock per 100 μ L sample. The stained sample was incubated for 20 min at 37°C. The sample was then washed by centrifugation using an Amicon 100 kD centrifugal filter unit at 3000xg for 20 min and eluted by centrifuging at 1000xg for 2 min. 1 drop of stained sample was dropped on imaging slide and dried for 1 h. Dako mounting media

was used to mount the slide. A coverslip was then added to the slide. Imaging was performed using a Nikon A1 confocal microscope (Nikon Inc) at 10x magnification.

2.19 Characterization of QD-EV bond stability under biological and storage conditions

1.25 mg Sulfo-S-4FB (final concentration 3.58 mM) and 0.5 mg Sulfo-S-HyNic (final concentration 1.27 mM) were mixed in 1 mL 1xPBS and reacted at room temperature for 2 h. After 2 h, the 4FB-HyNic mixture was diluted to 1xPBS, aCSF (119 mM NaCl, 26.2 mM NaHCO₃, 2.5 mM KCl, 1 mM NaH₂PO₄, 1.3 mM MgCl₂, 10 mM glucose, 2.5 mM CaCl₂, adjusted to pH 7.4), and 1xPBS+10%FBS, respectively, at 1:10 ratio. The samples were stored at 4°C, 23°C, or 37°C up to 1 week. At 0 h, 4 h, 24 h, 48 h and 1 week, the absorbance of 50 µL of each sample at 354 nm was measured by the SpectraMax M5 Microplate Reader (Molecular Devices). The experiment was run in triplicate.

2.20 QD-sEV treatment of *ex vivo* human vaginal epithelial sheets

Tissues routinely discarded from vaginal repair surgeries were harvested from otherwise healthy adult women, placed in ice-cooled calcium- and magnesium-free PBS containing 100 U/mL penicillin, 100 µg/mL streptomycin and 2.5 µg/mL Fungizone (Life Technologies), and transported to the laboratory within 1 h of removal from the donor. Tissue harvesting and experimental procedures were approved by the Institutional Review Board of the Fred Hutchinson Cancer Research Center (IR file 4323). The deep submucosa was removed with surgical scissors and the remaining vaginal mucosa was cut into 5 x 5 mm pieces, which were incubated at 4°C for 18 h in 5 mL of a 12.5 U/mL dispase solution (354235; BD Biosciences). The epithelial sheets were dissected away from the underlying stroma with a dissecting microscope and placed in tissue

culture dishes. Solution of QD-sEVs or purified QDs (pQDs, f7-f9 collected from qEV column purified QD-4FB that served as negative control which did not contain EVs) were added to each well and incubated overnight. The next day, tissues were extensively rinsed with PBS and fixed overnight with 4% PFA in PBS with 1mM EDTA. After rinsing nuclei were counterstained with TOPRO-3 Iodine (ThermoFisher) and mounted on slides with Dako mounting media. Epithelial sheets were imaged on an EVOS FL Auto Imaging System (ThermoFisher).

2.21 Confocal imaging and time-lapse tracking of QD-bEVs on BV-2 cells

Confocal Imaging of QD-bEVs Interaction with BV-2 Cells: The BV-2 cells were ready for confocal imaging study after 1-2-day culturing on 35 mm imaging dish. 50 μ L of QD-bEVs were mixed with 1,950 μ L of cell culture media and added to 1 dish of BV-2 cells. 50 μ L of pQDs were mixed with 1,950 μ L of cell culture media and added to 1 dish of BV-2 cells, as the negative control. BV-2 cells were incubated at 37°C in a 5% CO₂ atmosphere for 24 h, fixed with 10% buffered formalin (ThermoFisher) for 10 min, and then washed twice with 1xPBS. The cells were then stained with DyLight 488 Labeled Lycopersicon Esculentum (Tomato) Lectin (Vector Laboratories) at 1:1000 ratio in 1xPBS for 1 h. Cells were then imaged by a Nikon A1 confocal microscope (Nikon) under same camera and laser setting. Z-stack images at 60x or 4-time zoom in at 60x were taken, and maximum-intensity projection were formed.

Time-Lapse Tracking of QD-bEVs Interaction with BV-2 Cells: After 1-2 day of BV-2 cell culturing on 35 mm imaging dish, the cells were stained with DyLight 488 Labeled Lycopersicon Esculentum (Tomato) Lectin (Vector Laboratories) at 1:1000 ratio in pre-warmed cell culture media at 37°C in a 5% CO₂ atmosphere for 1h. The cells were then washed twice with cell culture media. 35 μ L of QD-bEVs were mixed with 950 μ L of cell culture media and added to 1 dish of

BV-2 cells. After 1 h and 4 h incubation at 37°C in a 5% CO₂ atmosphere, the 35 mm dish of BV-2 cells were quickly moved to an incubation chamber (37°C, 5% CO₂, and over 40% humidity) to perform time-lapse imaging. Images were taken at 60x every 5 min for 1 h at various locations in the chamber.

Quantitative Analysis of Time-Lapse Videos: The time-lapse videos were first image processed using Fiji software. Briefly, Images were split into two channels. The MinError threshold was applied to cell channels and QD channels were adjusted for brightness first, then filtered for noise by Gaussian Blur with a radius of 1 pixel. The Otsu threshold was applied to QD channels for converting to binary images. Two processed channels were merged. For each individual cell that existed in more than 80% of the frames of the video, the interaction of QD-bEVs with the cell were counted in each frame and summed together as the cumulative count of bEV-cell interaction for each cell.

2.22 Photostability comparison of QD-bEVs and DiI-bEVs

2 µL of 2.5 mg/mL DiI (ThermoFisher) were mixed with bEVs and incubated at room temperature for 20 min, followed by SEC through qEV column. 50 µL of QD-bEVs or DiI-bEVs were mixed with 1,950 µL of cell culture media and added to BV-2 cells cultured on 35 mm imaging dishes, respectively. Treated BV-2 cells were incubated at 37°C in a 5% CO₂ atmosphere for 24 h, fixed with 10% buffered formalin (ThermoFisher) for 10 min, and then washed twice with 1xPBS. The cells were then imaged using Nikon A1R confocal microscope (Nikon). Time-lapse imaging with No Delay (continuous laser exposure) was performed on cells for 10 min with perfect focus turned on to keep the z-plane consistent during the imaging. Time measurement was performed real-time on each region of interest to measure the fluorescence intensity change over time. Laser 405 was

used for QD-bEVs and laser 561 was used for DiI-bEVs, with the laser power held the same for both samples. The intensity was normalized by the intensity at 0 min.

2.23 Statistical analysis

In Chapter 3, data were displayed using the mean value \pm the standard error of the mean (SEM) for the colloidal stability study, and using the median value \pm 95% confidence intervals for the *in vitro* cell study, *ex vivo* OWH slice study, RT-qPCR, and toxicity study. Statistical analysis was performed using the unpaired *t*-test without correction. Statistical significance was determined under type I error at $p < 0.05$. Any difference corresponding to $p < 0.05$ (*) and $p < 0.01$ (**) was marked on the graph. The change in hydrodynamic size of QD-MPA, QD-PEG-OH, and QD-PEG-OMe during the 2000-second aggregation kinetics study was smoothed using a locally weighted scatterplot smoothing (LOWESS) approach with a window size of 10. All statistical analyses were conducted using GraphPad Prism 7.01 (GraphPad Software Inc).

In Chapter 4, data were displayed using the mean value \pm SEM for the DLS, NanoSight and absorbance studies, and using the median value with interquartile range for the bEV-cell interaction study. Statistical analysis of DLS data was performed using the sample unpaired *t*-test. Statistical analysis of cumulative counts of bEV-cell interaction was performed using the Mann-Whitney U-test. Statistical significance was determined under type 1 error at $p < 0.05$. Any difference with $p < 0.05$ (*), $p < 0.01$ (**) and $p < 0.0001$ (****) was marked on the graphs. All statistical analyses were conducted with GraphPad Prism 7.01 (GraphPad Software Inc).

CHAPTER 3: Quantum dot cellular uptake and toxicity in the developing brain:

Implications for use as imaging probes

3.1 Introduction

The current lack of a comprehensive assessment of QD behavior in the brain could hinder further investigation and translation of QD-based neurological imaging probes. Toxicity is a common concern for QDs, due to either the leaching of inorganic ions from the QD crystal,⁶⁷ or loss of QD colloidal stability and subsequent micrometer-scale aggregate formation upon administration, leading to inflammation and granuloma formation.^{7, 8, 68} Moreover, different QD surface coatings can have different cell- or tissue-targeting effects,⁶⁹ and lead to diverse cell cytotoxicity,⁷⁰ with varying degrees of injury and *in vivo* biodistribution.⁷¹ It has also been reported that various terminal end groups on functionalized QDs can result in a variable level of inflammatory responses.⁷² Despite the focus on QD engineering, a failure to adequately consider the physiological environment has also limited the application of QD-based nanoparticles.⁷³ A systematic evaluation of QDs focused on both nanoparticle engineering and physiological variance in the tissue environment is therefore essential.

Hence, we investigated QD stability, cellular uptake, and toxicity with three surface end groups in relevant brain environments, including *in vitro*, in cultured brain slices (*ex vivo*), and *in vivo*. An

array of efficient, red-emitting ($\lambda_{max} > 600$ nm), aqueous-dispersible QDs with three custom surface functionalities were targeted: 3-mercaptopropionic acid (MPA), poly(ethylene glycol) (PEG)-5000k-methoxy (PEG-OMe), and (PEG)-5000k-hydroxyl (PEG-OH). A core-shell CdSe/CdS QD architecture was selected in order to maximize luminescence efficiency,^{14, 54, 55, 74} while care was taken to keep the overall diameter of the inorganic nanocrystal

below 8 nm, such that the overall hydrodynamic diameter of the functionalized QDs would be below ~20 nm (accounting for a ~6-nm-thick ligand corona). We have previously shown that this size range facilitates efficient transport within the brain environment.^{28, 75} CdSe nanocrystal cores were synthesized with a protective shell of CdS to facilitate efficient luminescence (quantum efficiencies of up to 60% were achieved), and custom, red-emitting core-shell QDs were then generated *via* functionalization with the desired ligand and transfer to aqueous media. Numerous replicates of the optimized core-shell synthesis were carried out in order to produce sufficient quantities of functionalized QDs for the *in vitro*, *ex vivo*, and *in vivo* studies described in this study. QD colloidal stability and aggregation kinetics were evaluated in PBS and aCSF. QD cellular uptake was measured in organotypic brain slices, and QD toxicity was monitored in both *in vitro* microglia cells and organotypic brain slices, along with changes in expression levels of cytokine and oxidative stress markers. QD cellular localization was evaluated following i.p. administration in a newborn rat model with hallmarks of neuroinflammation, and real-time imaging was utilized to show QD internalization and trafficking in cells. The combination of *in vitro*, *ex vivo*, and *in vivo* models allows for investigation of QD-cell interactions in a three-dimensional (3D) environment that captures the complexity of the brain microenvironment.^{56, 76} Importantly, incorporating the effect of the brain microenvironment enables the development of QD-based imaging probes that could target regions of interest in the CNS and alter localization and cellular interaction based on the intended outcome.

3.2 Results and discussion

3.2.1 Physicochemical characterization of core-shell CdSe/CdS QDs

The physicochemical properties of the core-shell CdSe/CdS QDs were characterized as a function of surface functionality in 10 mM NaCl (Table 2). Details of the QD synthesis and surface functionalization are provided in the Methods section. QD-MPA particles exhibited hydrodynamic diameters of 11.3 ± 1.7 nm, with a surface charge (zeta potential, ζ -potential) of -30.1 ± 5.5 mV, confirming the presence of negatively-charged surface carboxylate groups. QD-PEG-OH and QD-PEG-OMe particles exhibited hydrodynamic diameters of 23.9 ± 2.0 nm and 17.3 ± 0.8 nm respectively, corroborating the attachment of 5000 Da PEG, which added an additional 5-6 nm to the hydrodynamic diameter of the particle, as compared to the non-PEGylated QD-MPA particles. PEG-functionalized QDs with an inert (methoxy) pendant functional group (QD-PEG-OMe) exhibited surface potentials of -8.3 ± 3.7 mV, while PEG-functionalized QDs with pendant hydroxyl functional groups (QD-PEG-OH) exhibited zeta potentials of -13.1 ± 1.5 mV. Since PEG is an uncharged hydrophilic polymer, PEG-functionalized QDs exhibited a more near-neutral net surface charge, as compared to the carboxylate-functionalized QD-MPA particles (-30.1 ± 5.5 mV).

Table 2. CdSe/CdS QD characterization in 10 mM NaCl.

QD hydrodynamic diameter was measured in 10 mM NaCl at pH 7.4 and 23°C using DLS. Measurements were made in triplicate for n = 3 batches with the SEM reported below. ζ -potential were measured using laser Doppler anemometry.

Particle	Surface Functionality	Size \pm SEM	ζ -potential \pm SEM
QD-MPA	MPA	11.3 ± 1.7	-30.1 ± 5.5
QD-PEG-OH	PEG-OH	23.9 ± 2.0	-13.1 ± 1.5
QD-PEG-OMe	PEG-OMe	17.3 ± 0.8	-8.3 ± 3.7

Both CdSe nanocrystal cores and core-shell CdSe/CdS QDs have a roughly spherical morphology (Figure 1), with CdSe nanocrystal cores exhibiting diameters of 3.4 ± 0.4 nm and final core-shell CdSe/CdS QDs exhibiting diameters of 6.7 ± 0.5 nm (Figure 1B), excluding the outer ligand corona. The spectral profiles of the QDs (Figure 1) remained largely unperturbed, irrespective of which surface ligation was selected. Additional physicochemical evidence of successful surface functionalization *via* attenuated total reflectance Fourier transform infrared (ATR-FTIR) spectroscopy can be found in the Appendix A (Figure A1). Both PEGylated QD samples exhibit all of the expected characteristic FTIR peaks,⁷⁷⁻⁷⁹ with the QD-MPA samples exhibiting clear carboxylate (COO^-) stretches at 1560 and 1410 cm^{-1} ,^{80,81} indicating full deprotonation of the MPA ligands.

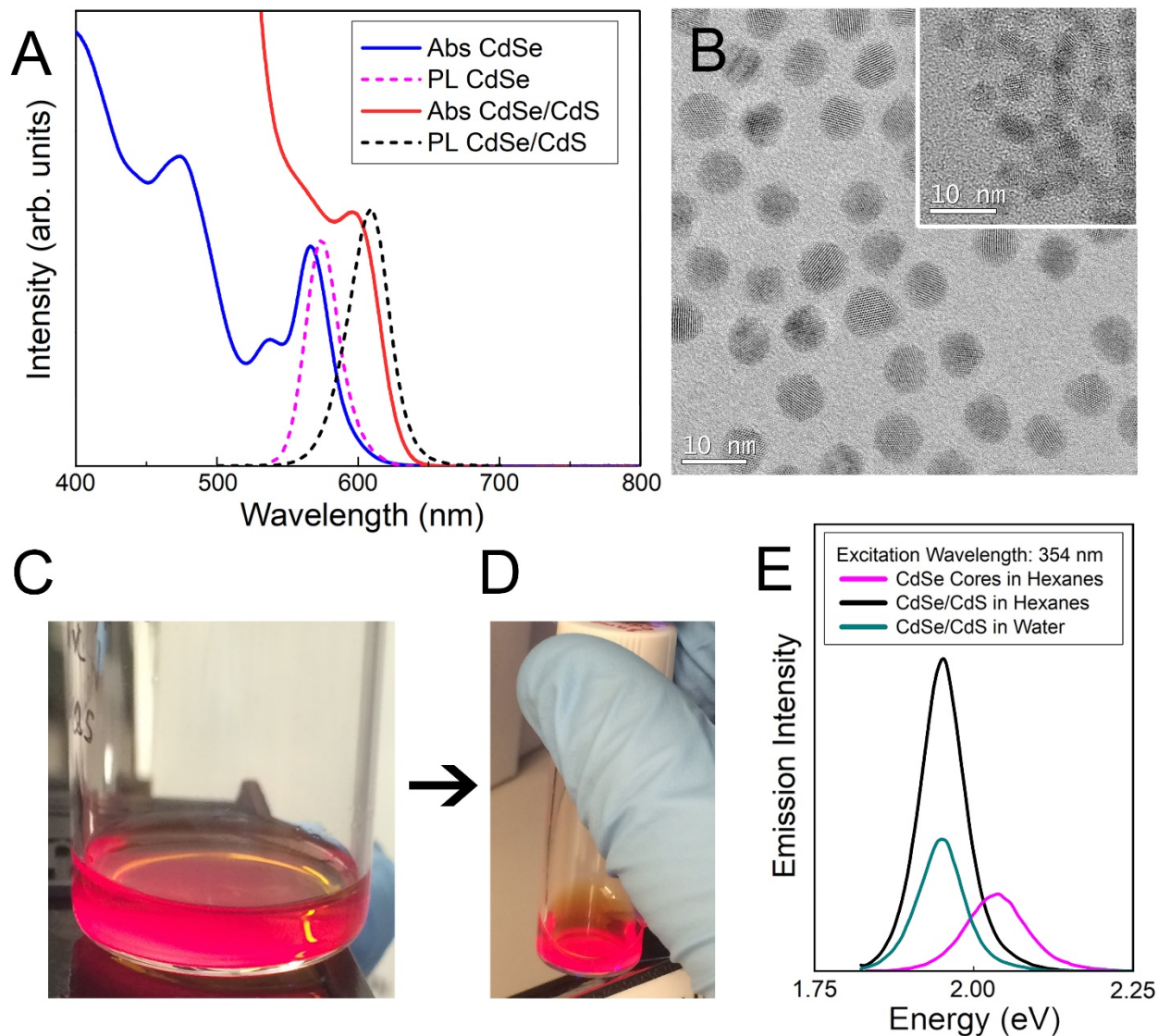


Figure 1. Surface functionalization and characterization of CdSe-CdS core-shell QDs.

(A) Absorbance and photoluminescence of CdSe nanocrystal cores (blue and pink) and final core-shell CdSe/CdS QDs (red and black) with 60% quantum yield. (B) TEM images of final 6.7±0.5-nm-diameter core-shell QDs and initial 3.4±0.4-nm-diameter nanocrystal cores (inset). (C,D) Images of QD dispersions under UV excitation (C) before and (D) after surface functionalization and transfer to aqueous media. (E) Relative emission intensity of initial nanocrystal cores (pink), and final core-shell QDs before (black) and after (green) surface functionalization and transfer to aqueous media. Data provided courtesy of Brittany Bishop and Nicole Thompson.

3.2.2 Colloidal Stability of QDs in neurophysiologically relevant fluids.

QD-based nanoparticle probes must be both stable and monodisperse to be effective as biomarkers, particularly for applications in the brain. As such, we conducted both long-term and short-term QD stability studies under neurophysiologically relevant conditions. We first monitored the hydrodynamic diameter of the core-shell CdSe/CdS QDs with different surface functionalities in 1xPBS and aCSF at 0 h, 4 h, and 24 h at 37°C, using DLS to evaluate any long-term tendency toward aggregation in brain-related fluids at physiological temperatures. Hydrodynamic diameters measured from dispersions of QD-MPA particles increased dramatically from 20 nm to more than 200 nm over 24 h in 1xPBS, while QD-PEG-OH and QD-PEG-OMe retained an unchanging hydrodynamic diameter (20-30 nm) over the entire measurement period (Figure 2A). When transferred to aCSF – a more complex and more brain-representative media – QD-MPA particles tended to aggregate immediately (hydrodynamic diameter > 1500 nm) (Figure 2B). In contrast, QD-PEG-OMe particles were relatively stable in aCSF over the entire 24-hour period, while QD-PEG-OH showed a statistically increased hydrodynamic diameter at 24 h but remained below 100 nm in total hydrodynamic size (Figure 2B).

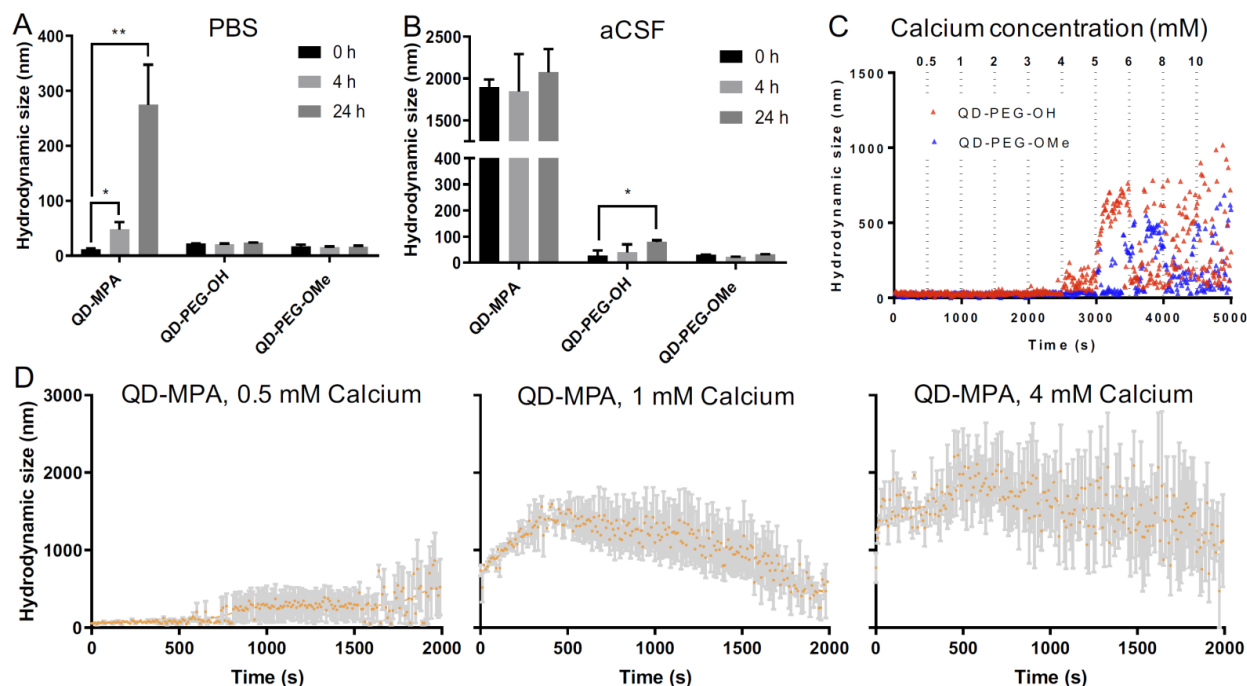


Figure 2. Colloidal stability of QDs at 37°C in neurophysiological-relevant fluids.

(A) QD hydrodynamic diameter at 37°C in 1xPBS at 0, 4, 24 h (n=3 measurements per particle type). (B) QD hydrodynamic diameter at 37°C in aCSF at 0, 4, 24 h (n=3 measurements per particle type). (C) Initial aggregation kinetics of QD-PEG-OH and QD-PEG-OMe at 37°C in aCSF with incremental addition of CaCl₂ every 500 sec, up to a 10 mM Ca²⁺ concentration. (D) Initial aggregation kinetics of QD-MPA at 37°C in CaCl₂ solution with 0.5, 1, and 4 mM Ca²⁺ over a period of 2000 sec (n=3 measurements per particle type). Trendlines showing initial QD-MPA aggregation were generated using a LOWESS regression in GraphPad.

To further explore media components that can give rise to rapid aggregation, we then evaluated the initial aggregation profiles of each functionalized QD in aCSF with different concentrations of calcium over a period of 30 min. Calcium ions play a significant role in the brain as a universal messenger of extracellular signals in a variety of cells, and pathological changes in calcium homeostasis could cause alterations in neuronal function and have been associated with brain aging and Parkinson's disease.^{82, 83} Calcium is a prevalent component in CSF and has been shown to lead

to significant aggregation of colloidal particles.⁶⁰ As such, we investigated how QD stability changes in aCSF with different Ca^{2+} concentrations in order to gain preliminary insight into nanoparticle behavior in the brain microenvironment. QD-MPA was observed to aggregate in aCSF with Ca^{2+} concentrations as low as 0.5 mM and exhibited increased rates of aggregation with 1 mM and 4 mM Ca^{2+} concentrations (Figure 2C-D). Sedimentation was observed after initial QD-MPA aggregation, where particles aggregated to sizes greater than 1000 nm and then sedimented to the bottom of cuvette, resulting in a decrease in DLS signal which manifests as a drop in the *apparent* hydrodynamic diameter reported by the instrument. When Ca^{2+} levels were increased, QD-MPA aggregation kinetics shifted from gradual aggregation to much more rapid aggregation followed by particle sedimentation (Figure 2D, Figure A2A), demonstrating a more severe instability of QD-MPA in an environment with a stronger ionic strength. Decreasing the system temperature slowed the aggregation kinetics of QD-MPA, although aggregation was still clearly present (Figure A2B-C). In contrast, both QD-PEG-OH and QD-PEG-OMe remained stable at room temperature and at physiological temperature in 1xPBS and aCSF for up to 24 h, supporting the use of PEG functionalization to provide steric stabilization.⁸⁴ QD-PEG-OH was stable up to a Ca^{2+} concentration of 4 mM, but exhibited significant aggregation above 5 mM Ca^{2+} (Figure 2C). QD-PEG-OMe showed a similar trend, with stable dispersions up to a 5 mM Ca^{2+} concentration with signs of aggregation at higher concentrations. Considering that the Ca^{2+} concentration in the human brain is on average 2 mM, these data suggest that the application of PEGylated QD particles to the brain is viable.

Importantly, in aCSF we see no dissolution of QDs into appreciable amounts of Cd ions. Using ICP-MS analysis, we measured Cd-ion concentrations following incubation for 0 and 24 h in aCSF. Cd-ion concentrations were stable for all QDs across the experimental time frame, and

remained less than 10 parts per billion (ppb) (Figure A3A). We also incubated 0.1 μ M QDs in aCSF at 37°C for 24 h, and measured the luminescence intensity of the QD suspensions at 0 h, 1 h, 4 h, and 24 h of incubation (Figure A3B). The photoluminescence (PL) of the QD-MPA particles remained stable over 24 h, while the PL intensity of the PEGylated QDs decreased over time. This likely occurs because the well-dispersed PEGylated QDs are completely exposed to the aCSF environment, while the non-PEGylated QDs (QD-MPA) aggregate quickly (Figure 2A), resulting in a lower initial PL intensity, but a less rapid decrease in PL intensity since the QD-MPA particles contained within the aggregate are protected from aCSF exposure. Independent of the change in PL, all confocal imaging studies have clear QD detection at low laser power with high signal to noise in the *in vitro* cell culture, *ex vivo* brain slices, and *in vivo* tissue sections.

Both long-term and short-term QD stability studies indicated a significantly different aggregation pattern for non-PEGylated QDs (QD-MPA) as compared to PEGylated QDs (QD-PEG-OH and QD-PEG-OMe). PEGylated QDs were found to be stable at different temperatures and in different neurophysiologically relevant fluids, while non-PEGylated QDs were very sensitive to changes in media conditions, with decreased stability at higher Ca^{2+} concentrations or longer incubation time.

3.2.3 Ex vivo QD cellular uptake and time-lapse internalization imaging.

A comprehensive understanding of cellular uptake is critical when discussing the interpretation of QD-based biomarkers. Thus, the cellular uptake of QDs in OWH slices was evaluated as a function of surface functionality, brain cell type, and brain region. Independent of surface chemistry, all QDs were found localized primarily in microglia in the neonatal rat brain, particularly in the corpus callosum and hippocampal regions (Figure 3A). Microglia – the innate immune cells of the brain – become activated in response to injury and uptake invading foreign bodies by phagocytosis.⁵⁶

Our cellular uptake findings not only further support previous observations that QDs are preferentially taken up by microglial cells,²⁰ but also indicate that there is region-specific microglial uptake of QDs, as seen in our organotypic slice and *in vivo* studies. Our observations that QDs preferentially localize in the corpus callosum could be due to the abundance of proliferative and phagocytic amoeboid microglia cells in the corpus callosum in the developing brain.⁸⁵

QD-MPA, as compared to QD-PEG-OH and QD-PEG-OMe, had significant aggregation in the extracellular space (ECS) in the OWH slice model (Figure A4), consistent with the aggregation observed in aCSF and PBS. In this case, the tendency of QD-MPA toward aggregation inhibited successful distribution to all the microglial cells spread throughout the tissue. Confocal images acquired at 60x magnification and 4-fold zoom enabled a closer look at QD internalization in microglia at the single-cell level. Although several QD-MPA aggregates were still observed to uptake in the microglia, the QD-PEG-OH and QD-PEG-OMe uptake was much more distinctive and diffuse in the microglial cytosol (Figure 3A inset). This observation led us to further explore the intracellular destination of the internalized QDs.

Upon staining live OWH slices with LysoTracker, we clearly observed both PEG-OH and PEG-OMe QD localization with lysosomes 120 min after QD introduction (Figure 3B, Movie A1 of QD-PEG-OH and Movie A2 of QD-PEG-OMe). Our observation of PEGylated QDs colocalizing with lysosomes supports the previously identified endocytic mechanism of QD cellular uptake and the degradation of QDs in the lysosomes of glial cells.^{86, 87} Importantly, the QDs were also found to be stable in low-pH environments (Figure A5), equivalent to those found in lysosomes.⁸⁸ Additional studies involving the manipulation of entry pathways and intracellular trafficking

through the use of inhibitors are needed for deeper understanding of QD intracellular trafficking, and eventual exocytosis or breakdown, in glial cells.

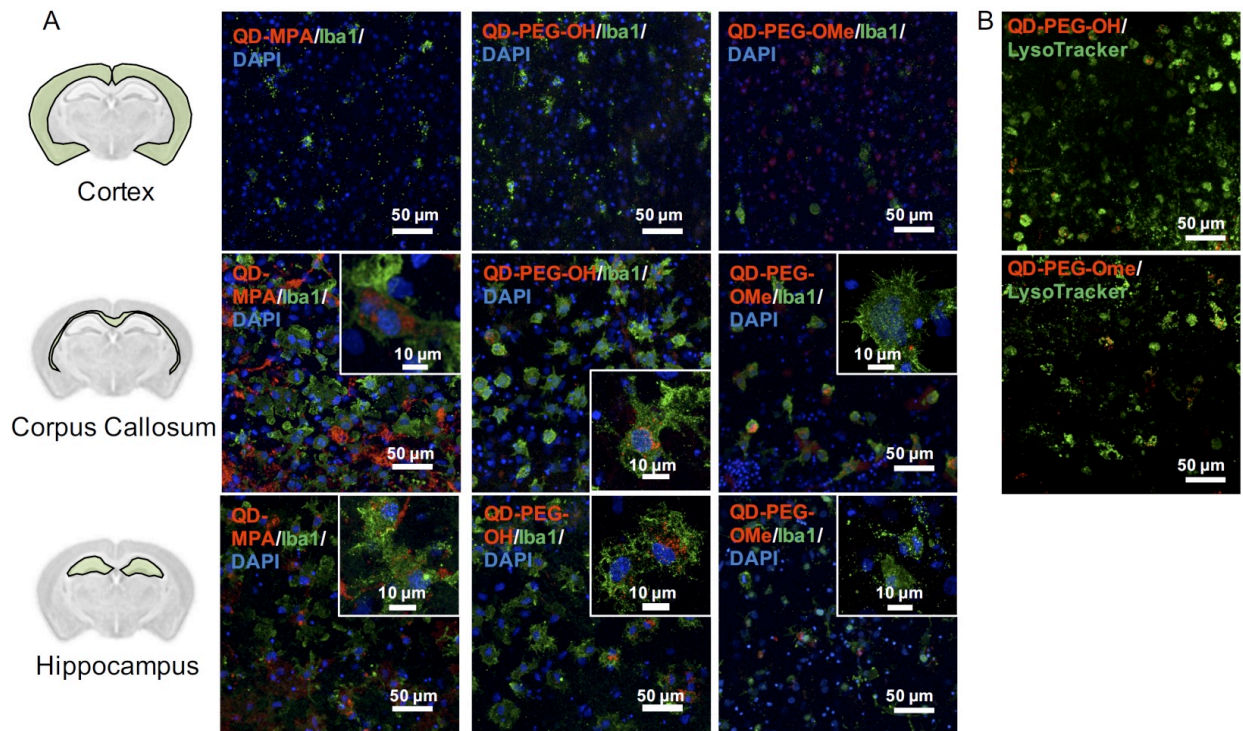


Figure 3. Iba1+ microglia and lysosome uptake of QDs in ex vivo OWH slices.

(A) Representative 40x magnification images of QD-MPA, QD-PEG-OH, and QD-PEG-OMe distribution and Iba1+ cellular uptake in the cortex, corpus callosum, and hippocampus in P14 SD rat OWH slices (300- μ m thickness). QDs (red, all images) were found internalized into Iba1+ microglia (green, all images), especially in the corpus callosum and hippocampus regions. Representative high-magnification images of QD-MPA, QD-PEG-OH, and QD-PEG-OMe localization inside Iba1+ cells are shown as insets. Cell nuclei were stained with DAPI and display blue luminescence. (B) Representative 40x magnification images of QD-PEG-OH (red) and QD-PEG-OMe (red) internalization into LysoTracker-stained lysosomes (green) in the corpus callosum region in a live OWH slice after 2 h of QD exposure.

The internalization of QDs into microglia was further demonstrated by time-lapse imaging in OWH slices, where QDs were observed to uptake into CD11b+ microglia in the corpus callosum

within the first 4 h of exposure, irrespective of surface functionality (Movies A3 – 5). To our knowledge, these live-tissue, time-lapse imaging studies provide the first direct observations of real-time QD internalization in *ex vivo* brain slices, and further confirm microglial targeting of QDs (Movies A3 - 5). QD-MPA rapidly formed large aggregates in the ECS, which prevented further internalization into microglia (Movie A3), although non-aggregated QD-MPA did show some microglial uptake. In order to understand whether QD trafficking into microglia is surface functionality dependent, we quantified the fraction of Iba1+ cells containing QDs in the corpus callosum region – the region where we saw the highest levels of QD internalization into cells. It was observed that the fraction of Iba1+ cells that uptake QDs after 24 h of QD exposure was in the range of 55% to 66% and was not significantly different between the three QD surface functionalities (Figure A6). Representative cross-sectional 240x z-stack images of QD internalization also show localization with Iba-1+ microglial cells in brain slices (Figure A7). Previous literature has shown that aggregates greater than 1000 nm in size preclude uptake into microglia and directly impact cellular responses.⁸⁹ However, if only non-aggregated QDs are considered, the extent of microglial QD internalization was independent of surface functionality. Although rarely observed in our study, on occasion some QDs also interacted with neurons, mostly in the cortex and hippocampus region (Figure 4). QDs were not observed to interact with or be internalized into oligodendrocytes (Figure A8). The distribution pattern of all QDs in neurons (Figure 4) is similar to previous studies done in organotypic hippocampal cultures, showing a potential interaction with the neuronal membrane and along the synapse.¹⁸ QD interactions with neurons may be due to the negative charge on the surface, which leads to an association with the electrophysiological activity of neuronal cells.¹⁹ Dante *et al.* observed that QDs stained along a synapse and associated with the neuronal membrane, when administered at a low dose (10 nM) on

primary neuron cultures, and Walters *et al.* observed that QDs interact with neurons in a sparse and distributed pattern.^{18, 19} Sophisticated engineering of QD ζ -potential should be taken into consideration, as Dante *et al.* found that strong detectable interactions with neurons were only observed for QDs with zeta potentials less than -20 mV,¹⁹ while Walters *et al.* illustrated that positively-charged QDs interacted specifically with oligodendrocytes.¹⁸ It is worth mentioning that previous literature presents contradictory results, indicating that QDs were internalized into one or other cell types to different degrees – results that might be conflicting due to the different conditions used in each study.¹⁸⁻²⁰ The source of the study platform – either cell culture or organotypic brain slice – can result in the differentiation of QD-cell interactions due to differences in cytoarchitecture network or accurate ECS representation,⁹⁰ as we have demonstrated in the present study. The emphasis of our study on QD-cell interaction in side-by-side comparisons of *in vitro*, *ex vivo*, and *in vivo* models demonstrates that the chosen model platform can clearly impact the outcome of a particular investigation. For example, the presence of tissue barriers could lead to a difference in QD accessibility to cells, and the stability of particles in various fluids could alter the biological identity of the QDs when applied to the different models. This knowledge helps to understand QD-cell interaction in a more systematic way, and emphasizes the importance of carefully considering the biological microenvironment when interpreting particle behavior.

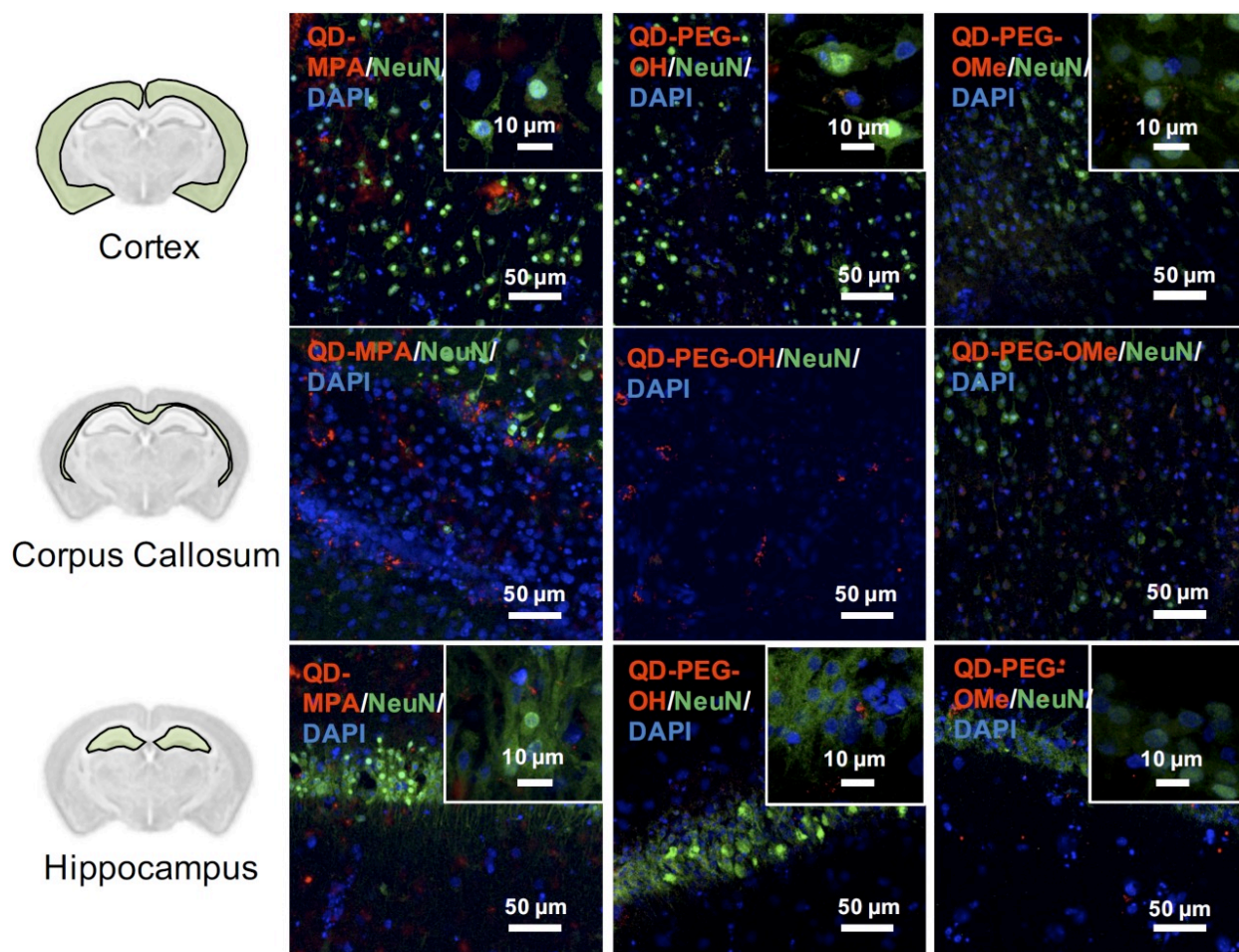


Figure 4. NeuN+ neuron uptake of QDs in *ex vivo* OWH slices.

Representative 40x magnification images of QD-MPA, QD-PEG-OH, and QD-PEG-OMe (red, all images) distribution and interaction with NeuN+ neurons (green, all images) in the cortex, corpus callosum, and hippocampus in P14 SD rat OWH slices (300- μ m thickness).

Representative high-magnification images of QD-MPA, QD-PEG-OH, and QD-PEG-OMe interaction with NeuN+ cells are displayed as insets. Cell nuclei were stained with DAPI (blue).

3.2.4 QD-induced toxicity, oxidative stress, inflammation and metal detoxification in OWH slices as a function of surface functionality.

The cytotoxicity of QDs has long raised concerns about the application of QDs in biomedical applications. To use QDs in a highly complex functional organ, such as the brain, their toxicity needs to be carefully and fully investigated.⁹¹ However, it is difficult to draw clear conclusions

from reported studies thus far because of the use of numerous different cell lines, which each have varying thresholds for QD-induced toxicity and only represent certain types of brain cells rather than the whole integrated neurological network.^{92, 93} By using 300- μm -thick organotypic brain slices, the toxicity of QDs can be examined in a representative 3D heterogeneous environment. To study the amount of QD-induced toxicity in OWH slices, we first evaluated whole-slice cytotoxicity caused by the QDs by measuring cell death after 24 h of QD exposure, as a function of QD surface functionality and QD concentration. To note, QD-MPA was not included in the OWH slice toxicity assessment due to the observed rapid aggregation in biological fluids and subsequent hindered penetration and cellular uptake in OWH slices. The overall toxicity of PEGylated QDs was found to be dose-dependent (Figure 5). At 0.01 μM and 0.1 μM concentrations, PEGylated QD-induced cytotoxicity was below 10%, and there was no significant difference between the non-treated (NT) group and either of the two PEG functionalities (PEG-OH and PEG-OMe). When the dose was increased to 1 μM , QD-induced cytotoxicity increased to around 15% for QD-PEG-OMe and slightly above 10% for QD-PEG-OH. The cytotoxicity of 1 μM QD-PEG-OMe was significantly higher than the NT group, starting at 4 h post-treatment, and remained statistically higher at 8 h and 24 h. The relatively low toxicity of QD-PEG-OH and QD-PEG-OMe at low concentration is likely imparted due to the PEG coating, which has been previously shown to effectively decrease cytotoxicity and maintain tissue viability.⁹⁴

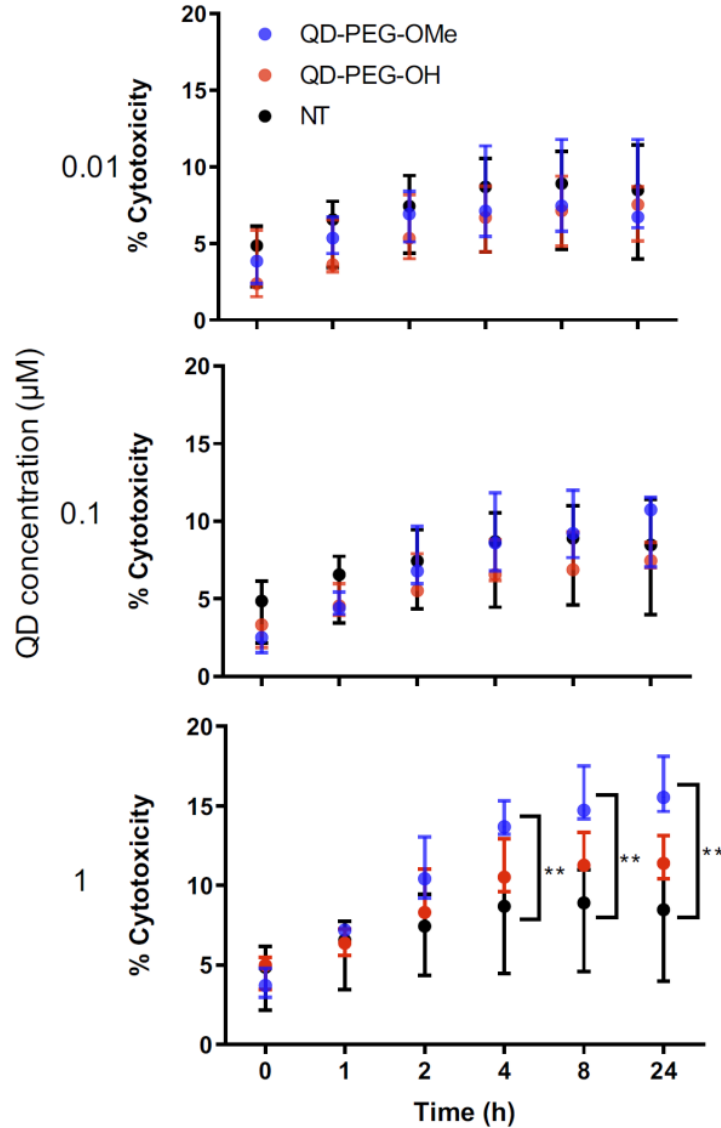


Figure 5. Dose-dependent toxicity of QD-PEG-OH and QD-PEG-OMe in *ex vivo* OWH slices.

Treatment of QD-PEG-OH (red) and QD-PEG-OMe (blue) at 0.01, 0.1, and 1 μM concentrations in P14 rat organotypic brain slices for 24 h. QD toxicity was determined by LDH assay at 0, 1, 2, 4, 8, and 24 h as follows. For each QD concentration, n=3 slices per QD per concentration condition were evaluated; for NT group (black), n=5 slices.

QD toxicity in the CNS can be due to multiple mechanisms, including intracellular QD breakdown^{70, 87, 92, 93, 95} and subsequent release of carcinogenic Cd^{2+} ions.⁶⁷ QD-induced inflammation or oxidative stress can also contribute to cell death and a cascade of function loss.

QDs with different functional groups were reported to induce different levels of proinflammatory effects *in vitro* on human lung epithelial cell lines as well as *in vivo* in mouse lung tissue following direct administration through intratracheal instillation.^{72, 96} For example, metallothionein proteins (MT, Mt for mRNA), which can sequester Cd ions and limit oxidative stress, have shown increased expression after QD treatment in kidney or lung cells.^{92, 97-99} However, no studies have been performed for the activation of MT in the brain following QD treatment. To investigate QD-induced inflammation, metal detoxification (Figure 6), and oxidative stress (Figure A9) in OWH slices, we also evaluated time-dependent mRNA profiles in response to QD exposure. MT-1, MT-2A, and MT-3 (different isoforms of MT) are protective against metal ion toxicity and oxidative stress, and are found in the CNS.^{100, 101} Strikingly, at 0.1 μM QD concentration, QD-PEG-OH and QD-PEG-OMe induced a significant 7.4- and 13.2-fold increase of Mt1 expression, respectively, in OWH slices after 6 h of incubation, and the Mt1 increase remained 3.5-fold higher after 24 h of QD-PEG-OMe incubation (Figure 6A). The significant increase in Mt1 mRNA expression 6 h after 0.1 μM QD exposure reflects the cellular response to activate metal detoxification pathways for Cd²⁺ exposure, which occurs rapidly upon localization in lysosomes, as observed in our study. The lysosomal localization could induce lysosomal dysfunction and oxidative stress, as previously suggested.¹⁰²

The pattern of surface functionality-dependent Mt1 increase is aligned with the pattern of surface functionality-dependent LDH release. QD-PEG-OMe induced the most significant expression-fold changes in Mt1, as compared to other QDs, and also had the highest LDH release. When the metal is in overloading conditions, the MT pathway becomes overwhelmed and can no longer effectively scavenge metals, resulting in cell death,¹⁰³ as we demonstrate with higher concentration (1 μM) QD-PEG-OMe exposure. Meanwhile, Mt2A and Mt3 did not show a significant increase in expression at any time point up to 24 h (Figure 6A). Mt3 is mainly present in neurons¹⁰¹ and would be less likely to be activated based on our observations that QDs internalize primarily in microglia. Although Mt2A showed a non-significant trend towards an increase in expression for QD-PEG-OMe, the expression increase is insignificant because Mt2A prefers binding Zn while Mt1 prefers Cd,¹⁰⁴ the main component of our QDs used in this study. To the best of our knowledge, our study is the first study to reveal QD-induced MT pathway activation in brain cells.

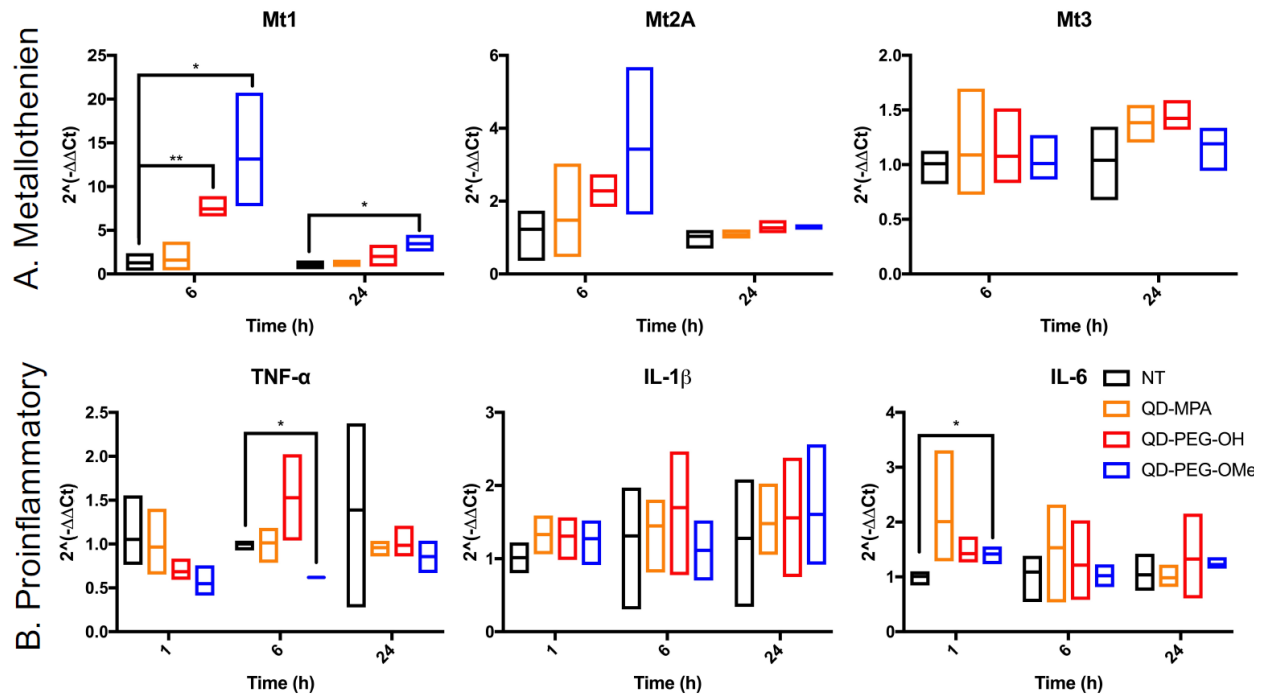


Figure 6. Time-dependent mRNA profiles of QD-induced metallothionein and proinflammatory markers in OWH slices.

Fold-changes in mRNA expression were measured at 1 h, 6 h, and 24 h of QD-MPA (orange), QD-PEG-OH (red), and QD-PEG-OMe (blue) exposure at 0.1 μ M concentration in OWH slices. The fold-changes were measured for (A) metallothionein isoforms Mt1, Mt2A, and Mt3 and (B) proinflammatory cytokines IL-6, TNF- α , and IL-1 β , and compared to NT slices (black). For 1 h, 6 h, and 24 h time points, $n = 3$ groups and $n = 3-6$ slices per group were evaluated for each experimental sample (except for the QD-PEG-OMe 6h proinflammatory sample, where $n = 2$ groups with $n = 6$ slices in total were evaluated). All data are reported as median values with 95% confidence intervals.

Interestingly, QD exposure resulted in almost no statistically significant inflammatory or other oxidative stress responses at the mRNA level. IL-6, TNF- α , and IL-1 β are pro-inflammatory cytokines and are central to neuroinflammatory processes.¹⁰⁵ BAX and Casp-3 are involved in neuronal death, oxidative stress, and apoptosis during brain pathology.^{106, 107} IL-10 and TGF- β 1 are both anti-inflammatory cytokines that play an important role in altering the function of

microglia,¹⁰⁸ and are highly influential in the developing brain.¹⁰⁵ Only QD-PEG-OMe showed a statistically significant 2.0-fold increase in IL-6 expression after 1 h incubation and a statistically significant 0.6-fold decrease in TNF- α expression after a 6 h incubation (Figure 6B). These changes were only present during early time points after initial QD exposure. Previous literature has suggested that PEGylated QDs can induce higher expression of proinflammatory cytokines, which was strongly associated with the functional groups at the end of PEG chain, leading to selective endocytosis.^{72, 96} In our studies, 0.1 μ M QD concentrations did not induce statistically significant cytotoxicity in OWH slices, activated a metal detoxification pathway, and led to a minimal inflammatory response in OWH slices over a 24 h period. This concentration was chosen to be representative of what cells would maximally be exposed to *in vivo* following systemic administration. Therefore, it is our conclusion that PEGylated QDs with pendant hydroxyl or methoxy groups used at this concentration exhibit microglia-dominant uptake and are not inducing inflammation or toxicity to brain cells within this particular timeframe. To further elucidate potential mechanisms of cellular response to QDs, higher doses could be tested in OWH slices to determine changes in mRNA expression, and further analysis on protein expression levels could be evaluated.

3.2.5 In vitro QD toxicity and cellular uptake on BV-2 cells.

The influence of the extracellular matrix (ECM) barrier on QD penetration and tissue distribution was observed in our *ex vivo* slice studies, which further impacted QD toxicity and cellular uptake. The LDH assay indicated similar cytotoxicity of QD-MPA across 0.01-1 μ M QD concentrations on OWH slices (Figure A10), which did not exhibit toxicity when compared with healthy NT slices. This result is different from what has been reported in previous literature, where non-

PEGylated QDs induce more immediate and significant cell death, while PEGylated QDs show minimal toxicity *in vitro*⁹⁵ due to the “stealth” ability of PEG. Consequently, we sought to understand the effect of QDs on microglial cells when cells are directly exposed to QDs and no penetration barrier is present. When applied directly to microglia, 0.01 μ M QD-MPA induced significant cell death starting at 1 h, as compared to a NT group treated only with 1xPBS. The viability of QD-MPA-treated cells was observed to drop below 50% before some recovery at 24 h (Figure 7). QD-PEG-OH, however, did not show any statistically significant decrease in cell viability, as compared with NT, except at 6 h (Figure 7). QD-MPA were immediately taken-up into BV-2 cells at the 1 h time point, with additional uptake continuing throughout the duration of the 24 h study (Figure A11). However, PEGylated QDs were not observed to uptake into BV-2 cells at any time point. This indicates that, when applied to an *in vitro* cell platform, PEG coatings did preclude particles from toxicity and cellular uptake. Considering the rapid instability of QD-MPA in biologically relevant fluids and their aggregation on the surface of OWH slices (Figures 15 and 17), QD-MPA are unlikely to overcome the penetration barriers introduced *via* the presence of the brain ECS and ECM in OWH slices.^{5, 76} This inability to penetrate tissue limits the interaction with cells throughout the tissue, whereas in the *in vitro* monolayer, QD-MPA had direct access to all cells. Due to the instability of QD-MPA, these particles are unlikely to be suitable for biomedical application or *in vivo* study.

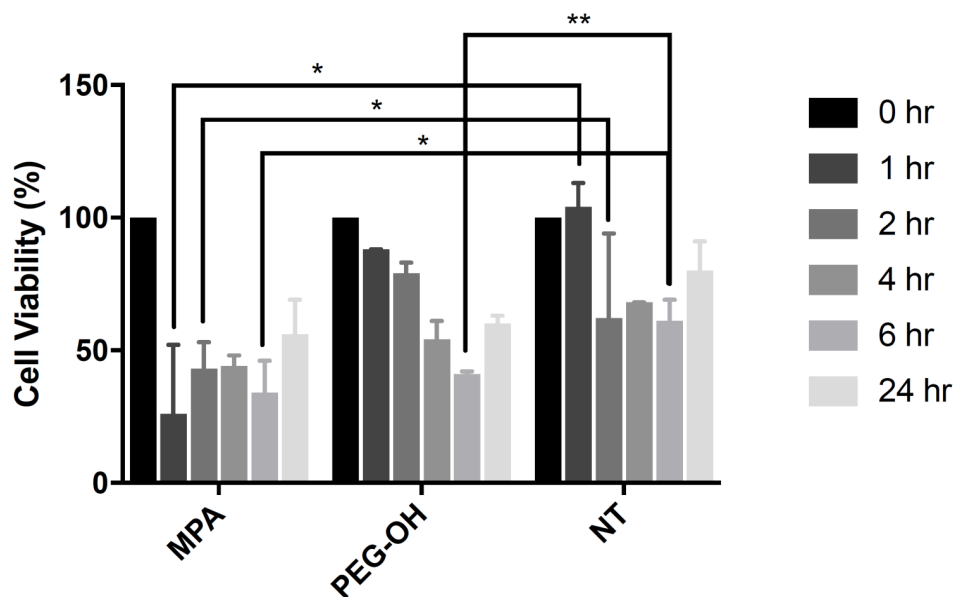


Figure 7. Toxicity of QDs on *in vitro* BV-2 cells.

Treatment of QD-MPA and QD-PEG-OH at 0.01 μM concentration on *in vitro* BV-2 cells for 1, 2, 4, 6, and 24 h, with reported % cell viability. For each condition, n=3 wells were evaluated with 10,000 cells per well when plated.

3.2.6 *In vivo* QD cellular uptake in *mglur5* neuroinflammatory rat model.

Lastly, we utilized the metabotropic glutamate receptor 5 (*mglur5*) neuroinflammatory rat model to evaluate QD uptake *in vivo*. In addition to studying QD behavior *in vitro* and *ex vivo*, we sought to explore how these findings translated to an *in vivo* environment in both normal and neuroinflamed tissue, through the use of a transgenic *mglur5* model. *mglur5* plays an important role in neuroinflammation,¹⁰⁹ especially with respect to microglia-associated inflammation and neurotoxicity.¹¹⁰ *mglur5* knock-out mice have been used recently as a model of neuroinflammatory diseases with hallmarks of Fragile X syndrome, schizophrenia, and autism spectrum disorder (ASD).¹¹¹ We utilized *mglur5* age-matched and litter-matched WT and KO rats to investigate QD behavior *in vivo* following systemic injection. We detected QD-PEG signal in the brain, at both 4 h and 24 h time points, after i.p. injection in P7 WT and KO rat pups. However, the QD signal was

minimal, due to the majority of the sub-20-nm QD-PEG being cleared rapidly.¹¹² Although the total quantity of QDs in the brain was low, we identified colocalization of QDs in microglia in various regions. QD-PEG-OH particles were found colocalized with Iba1+ microglia in both the WT and KO brain in the cortex, corpus callosum (Figure 8), hippocampus, and PVR (Figure A12), with the majority of accumulation in the corpus callosum region at 4 h post-injection (Figure 8). At 24 h post-injection, allowing for longer *in vivo* circulation, QD-PEG-OH were still found internalized in Iba1+ microglia (Figure A13), consistent with our observations in the OWH slices. Our findings in the WT neonatal brain – where we see comparable QD uptake to the KO brain – are supported by previously published work where QDs were observed to be present in brain vessels or epithelial cells or even to have permeated into brain parenchyma after systemic administration in healthy rodents.¹¹³⁻¹¹⁵ Although the mechanism of QD uptake in the healthy brain is still unknown, current findings suggest QD uptake occurs *via* transcytosis-mediated transport through the BBB and cellular uptake *via* phagocytosis and pinocytosis.¹¹³ The main regions of QD localization in our study included the corpus callosum and PVR, which are near to ventricles or nearby large blood vessels networks. Consequently, these areas experience high levels of fluid exchange, which can contribute to the distribution of QDs and internalization by cells in this region of the developing brain.

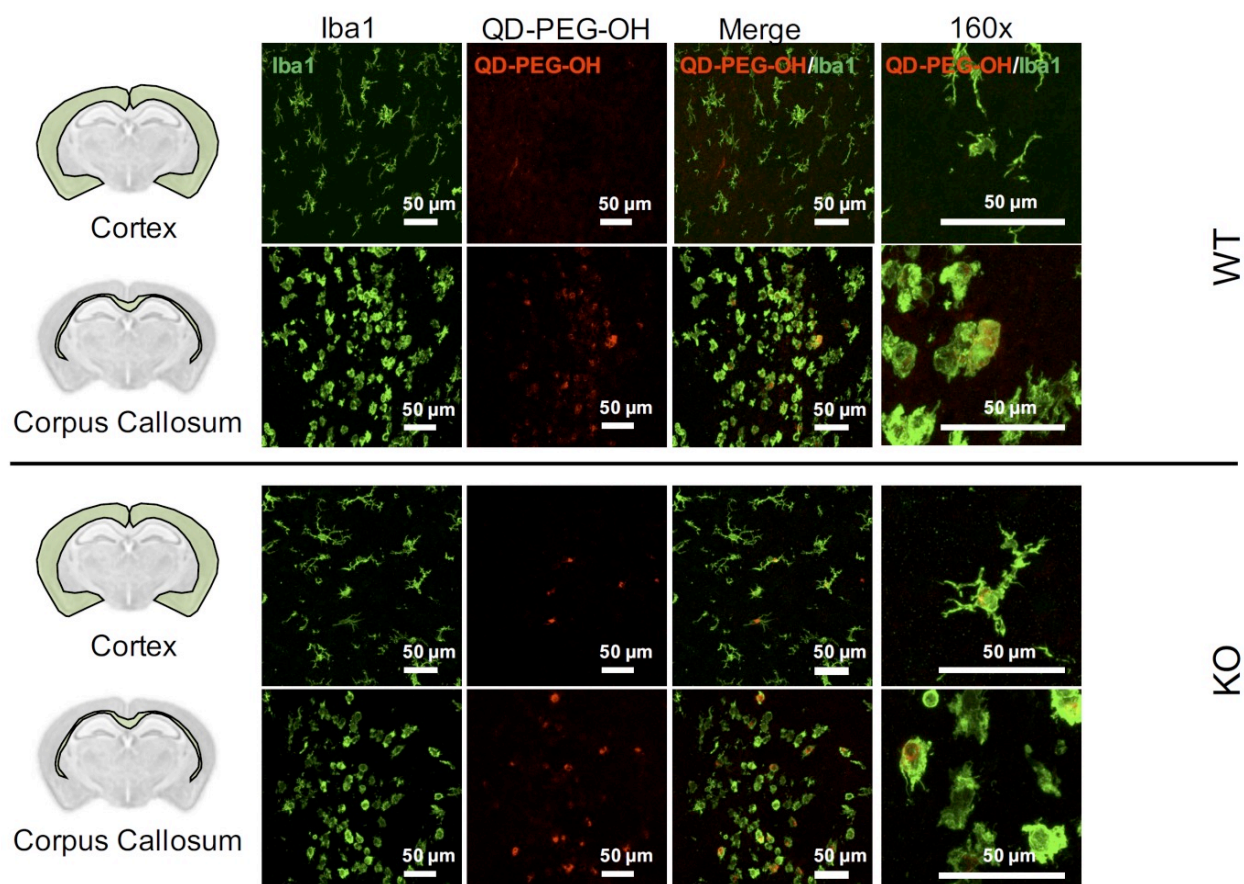


Figure 8. QD cellular uptake in P7 rats, 4 h post-administration.

Representative images of QD-PEG-OH (red, all images) colocalization with Iba1+ microglia cells (green, all images) in the cortex and corpus callosum regions in P7 *mglur5* WT and KO pup brains, 4 h after i.p. administration. 40x magnification images with 4-fold zoom (160x) are presented in the rightmost column to show QD-PEG-OH internalization in cells.

3.3 Conclusion

The implementation of engineered nanoparticles as biomarkers for CNS disease is a challenging task, requiring a comprehensive understanding of both nanoparticle engineering and the disease environment in which the nanoparticle will be applied. To develop QD-based biomarkers for application to the brain, it is necessary to better understand QD behavior in the brain environment. Here we comprehensively assessed the interaction of functionalized, core-shell CdSe/CdS QDs

with the brain microenvironment, including QD colloidal stability, toxicity, and cellular uptake *in vitro*, *ex vivo*, and *in vivo*. Importantly, stability, toxicity, and cellular uptake of QDs were dependent on one another, and dependent on the model used to evaluate the effect. We found that surface chemistry strongly influenced QD behavior in the brain. PEG-coatings improved QD stability in complex neurophysiological-relevant fluids, induced low cytotoxicity in brain slices, and led to stable, diffuse cellular uptake. QDs were preferentially taken up into microglia, especially in the corpus callosum, which was further confirmed *in vivo*. PEGylated QDs induced an increase in Mt expression in the OWH slices as a function of time and surface chemistry, but did not induce inflammatory and other oxidative stress pathways. Non-PEGylated QDs, however, destabilized rapidly when exposed to brain-relevant fluids, which prevented penetration into brain tissue. We also found that administration of functionalized QDs can result in dose-dependent toxicity in brain slices. Lastly, with a goal of reconciling seemingly contradictory findings in literature, our results clearly demonstrate the importance of considering the specific model system that is used to evaluate QD behavior. Importantly, this QD evaluation plays a critical fundamental role for further development of QD-based application in the brain environment, such as labeling and visualizing EVs, which we will discuss in details in Chapter 4.

CHAPTER 4: Quantum dot labeling and visualization of extracellular vesicles

4.1 Introduction

Direct visualization of EVs can be useful to understand EV trafficking and function between cells and within tissues. Current techniques for labeling and imaging EVs, however, have several challenges and limitations.¹¹⁶ Commonly used lipophilic dyes, including R18, DiI, PKH26, PKH67 or CellMask, target the lipid membrane of EVs; yet, these dyes can also form dye aggregates that are of similar size to EVs and therefore hard to distinguish.^{117, 118} Lipoproteins and other proteins co-isolated with EVs can also be stained with lipophilic dyes, which can transfer dye to the target cells, resulting in false positive stains that could imply EV uptake.¹¹⁸ RNA-based labeling methods have similar vesicle/dye aggregation challenges as lipophilic dyes.¹¹⁹ Optical reporters including green fluorescence protein (GFP) are successfully engineered to be fused to EVs within cells for EV labeling and are useful for studying the genesis and distribution *in vivo*;¹²⁰ however, GFP-transfected cells currently have limited translational potential to humans. In addition, these dyes often suffer from fast photobleaching. A universal, robust, high photoluminescent and easily controllable method is thus required to fill in the technological gap of direct EV tagging and visualization.

Here we propose using QDs to label and visualize EVs due to their great fluorescent imaging capabilities. There are numerous studies that utilize QDs to label and monitor molecules or cells of interest *in vitro*¹²¹ or *in vivo*.¹³ Our work in Chapter 3 shows QDs functionalized with PEG exhibit minimal toxicity (<15%) in the developing brain, are stable in biological aqueous settings, and can be easily imaged in tissues.¹²² Here, we use 4-formylbenzoate (4FB) to 6-hydrazinonicotinate acetone hydrazone (HyNic) click chemistry to label EVs with QDs. 4FB-

HyNic click chemistry can provide control over nuanced stoichiometry and labeling efficiency for QD conjugation.¹²³ We investigate the optimization of the formation of the QD-EV bond to design the most reproducible and stable QD-EV conjugate for imaging *in vitro* and *ex vivo*. We compare the photostability of QD-EV conjugates and DiI labeled EVs to demonstrate the advantages of QD-EV conjugates over traditional EV labeling method. We also explore the universality of this QD-EV conjugation by applying QD modification to diverse EV sources, including EVs isolated from human semen (sEVs) and the whole rat brain (bEVs). Moreover, we utilize QD-sEV conjugates on human vaginal epithelial sheet and QD-bEV conjugates on BV-2 murine microglial cells to image cellular interaction of EVs. This comprehensive approach establishes a robust system for individual EV visualization, which can benefit fundamental understanding of EV function and further the potential clinical application of EVs.

4.2 Results and discussion

4.2.1 Chemistry for QD-EV conjugation

The method for linking nanoparticles to EVs needs to be carefully chosen to be easily tailored and to minimally disrupt EV structural integrity. QDs have been previously tagged to EVs *via* immune-reaction either through cell-specific molecules¹²⁴⁻¹²⁸ or EV-characteristic antigens such as CD63.¹²⁹⁻¹³² However, EVs labeled with antibodies may become immunogenic,^{133, 134} and the QD coupled to the antibody can be far from the EV surface.^{131, 135} More importantly, molecules such as CD63 are not present on all EV populations,¹³⁶ so any method based on immunoaffinity would only capture a subpopulation of EVs. Another approach of nanotechnology-based EV labeling involves internalizing either gold,¹³⁷ iron oxide nanoparticles,^{138, 139} or QDs^{140, 141} into EVs, which can be non-uniform, diffusion driven, and disruptive to EV biofunction.

We chose a hydrazine-aldehyde based strategy to label EVs with QDs through the click chemistry 4FB to HyNic (Figure 9). This chemistry is reactive under mild conditions and is tailorable, resulting in high labeling efficiency and preservation of QD optical properties and biological target function.³⁴ The 4FB-HyNic coupling reaction has successfully linked different molecules in previous studies,^{142, 143} including linking antibodies to polymersomes,¹⁴⁴ and QDs to viruses,³⁴ which share comparable size and structure with EVs.¹⁴⁵ We used Sulfo-S-4FB and Sulfo-S-HyNic because they contain Sulfo-NHS esters, making this linker water soluble without needing organic solvent, which might be harmful to EVs. We modified commercially available QD-PEG-NH₂ with 4FB, and EVs with HyNic utilizing the amine-reactive NHS-ester. The protein enriched membrane of EVs is an advantage for amine-based coupling of HyNic, which can be generic to all sources of EVs.

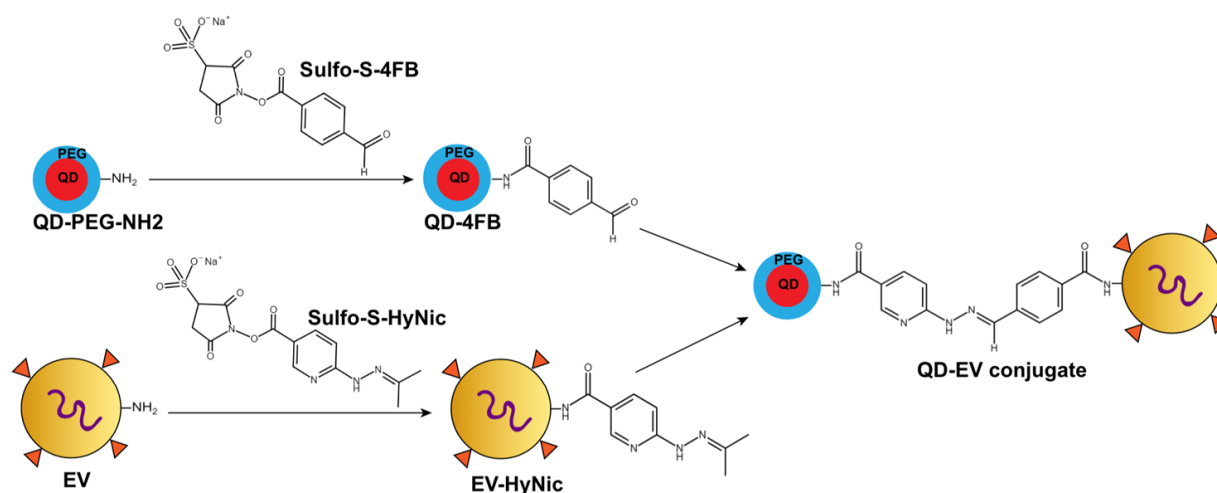


Figure 9. Schematic of QD-EV conjugation chemistry

PEG-NH₂ modified QDs are first conjugated with Sulfo-S-4FB (QD-4FB). EVs, which contain a surface rich in primary amines, are modified with Sulfo-S-HyNic (EV-HyNic). Under mild conditions at room temperature, the QD-4FB and EV-HyNic are reacted together to form a stable bis-aryl bond.

4.2.2 Characterization of Purified sEVs and QD-sEV conjugates

We first chose human sEVs to study the QD-EV conjugation because they are isolated from a body fluid and have been studied quite extensively. We isolated sEVs from healthy male volunteers by ultracentrifugation over sucrose cushions and characterized sEVs *via* Western blot and TEM.⁶² One concern for our QD-EV conjugation chemistry is that the NHS-ester used for QD and EV modification can react with any primary amine, which are abundant on proteins that can be co-isolated with EVs purified by ultracentrifugation.¹¹⁸ Therefore, we took into account that co-isolated proteins were smaller than EVs and separated them by SEC before conjugation (Figure 10A). We used the qEV column to further purify ultracentrifuge-isolated sEVs, and collected f1-25 to test the sEV particle quantity and protein concentrations. It has been previously established that purity of isolated EVs can be defined by the EV particle/protein ratio.⁶⁴ Based on the sEV and protein distribution measured in f1-f25, f7-11 contained 97% of the sEVs, while f14-23 contained 86% of proteins without detectable sEVs (Figure 10A). To minimize labeling of non-EV protein particles for QD-EV conjugation, we used f7-f10 that contain high purity sEVs.

During the QD-EV conjugation reaction, we first characterized the modification of QD-4FB and EV-HyNic, to ensure the labeling of EVs and QDs was successful. We confirmed the existence of HyNic on sEVs by successfully reacting with 4FB and forming a detectable bond that can be measured by absorbance at 354 nm.³⁴ Using UV-vis spectroscopy, we observed an increased absorbance signal at 354 nm after mixing of sEV-HyNic and free Sulfo-S-4FB during the first 30 min (Figure 10B). This matches the trend shown by conjugating free Sulfo-S-4FB to free Sulfo-S-HyNic (Figure 10C). Previous literature has shown a decrease in zeta potential indicates 4FB conjugation to a free amine group.³⁴ We confirmed the modification of QD-PEG-NH₂ with Sulfo-S-4FB by a decrease in zeta potential of QD-4FB (-3.7 mV) compared with QD-PEG-NH₂ (0.9

mV) (Figure 10D). This reduction of zeta potential is likely due to the conversion of a few protonated PEG-NH³⁺ to 4FB after modification. The average hydrodynamic size of QD-PEG-NH₂ and QD-4FB was 17.0 nm and 17.4 nm, respectively (Figure 10D), which indicates the modification of 4FB on QDs did not change the size of QDs.

To remove free QDs (~10-20 nm) from the QD-EV (~80-200 nm) conjugates and reduce signal from unconjugated QDs, we took advantage of the conjugate size difference and utilized SEC for further separation. We confirmed the successful separation of unconjugated QDs from conjugated QD-EVs after SEC by fluorescence spectroscopy. QD signal appeared in f7-10 and f11-28 for QD-sEV conjugate samples, while QD alone samples only showed fluorescent signal in f10-28 (Figure 10E). Since we identified f7-10 as the fractions that contain the majority of sEVs (Figure 10A), the QD signal in f7-10 detected from QD-sEV conjugate samples was considered to be derived from the QD-sEVs rather than unconjugated QDs. To minimize the retention of unconjugated QDs that can interfere with the signal from QD-sEVs, we only collected f7-9 for further analysis and application.

We then measured the size and zeta potential of sEV-HyNic and QD-sEV conjugates after conjugation (Figure 10F,G). The average size of sEV-HyNic was 159.7 nm and the average size of QD-sEV was 164.0 nm, characterized by NanoSight (Figure 10F). The zeta potential, characterized by DLS, was -7.7 mV for sEV-HyNic and -9.1 mV for QD-sEVs (Figure 10G), as compared to the -3.7 mV for QD-4FB (Figure 10D). These zeta potentials are all near-neutral.⁵ We confirmed the fluorescence spectra of QDs remained the same before and after conjugating to EVs (Figure 10H). This result further supports previous studies that the application of 4FB-HyNic chemistry does not diminish QD optical properties.³⁴ Based on these findings and prior literature,

we do not expect the optical properties of QDs to be significantly different before and after EV labeling.

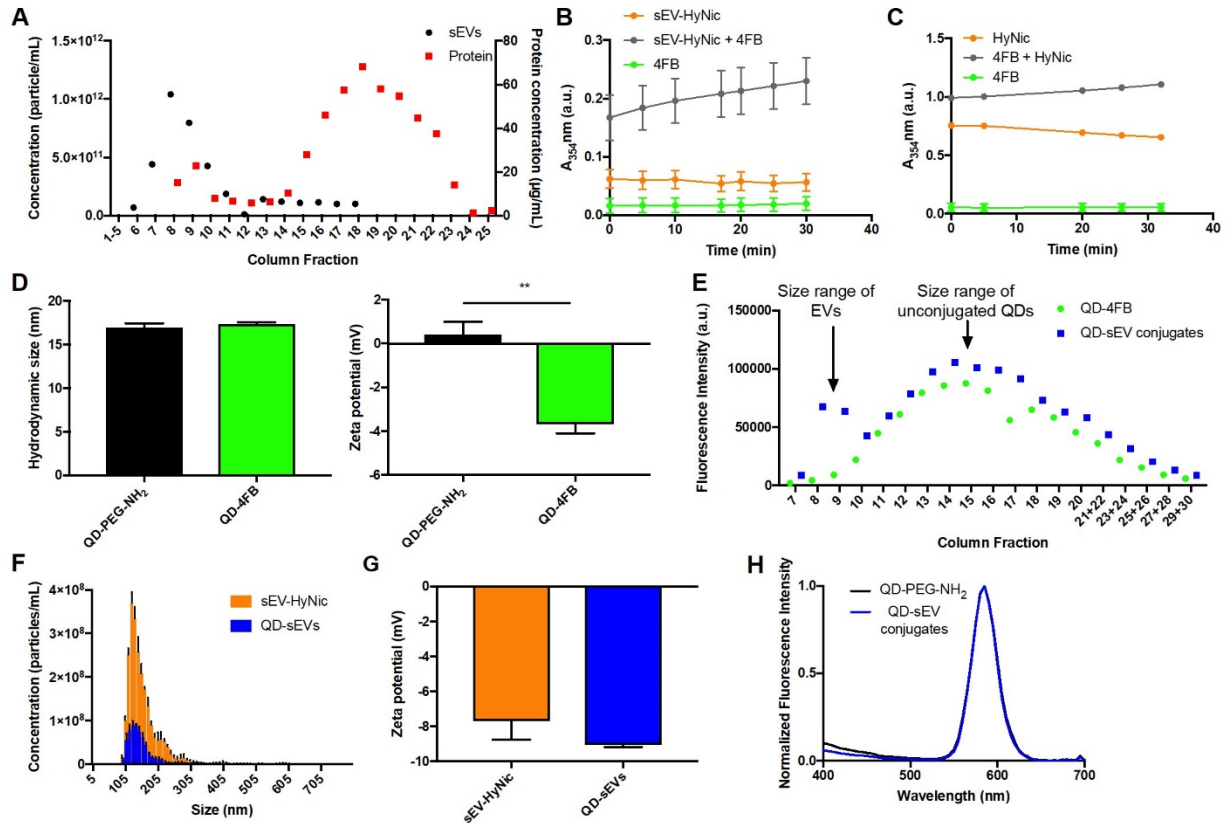


Figure 10. Characterization of purified sEVs and QD-sEV conjugates.

(A) Representative data of sEV particle quantity (black) and protein concentration (red) distribution in elution f1-25 of qEV column purification. f7-11 contain ~97% of EVs with only 11% of protein, while f14-23 contain 86% of protein. Data provided courtesy of Dr. Lucia Vojtech. (B) Absorbance intensity at 354 nm of Sulfo-S-4FB (green), sEV-HyNic (orange), and sEV-HyNic + Sulfo-S-4FB (grey) during the first 30 min after chemical addition and mixing. sEV-HyNic modification was confirmed by increased absorbance at 354 nm (n=3). (C) Absorbance intensity at 354 nm of Sulfo-S-4FB (green), Sulfo-S-HyNic (orange) and Sulfo-S-4FB + Sulfo-S-HyNic (grey) during the first 30 min after chemical mixing (n=3). (D) Hydrodynamic sizes (left) and zeta potential (right) of QD-PEG-NH₂ (black) and QD-4FB (green) in 1xPBS (n=3). (E) Representative data of QD-sEV conjugates (blue) and QD-4FB alone (green) fluorescence intensity at 585 nm in elution f7-30 of qEV column purification of QD-sEV conjugates. Data provided courtesy of Dr. Lucia Vojtech. (F) Size distribution of sEV-

HyNic and QD-sEV (n=3) – black lines represent SEM for each size reported. (G) Zeta potential of sEV-HyNic and QD-sEV conjugates in 1xPBS (n=3). (H) Representative fluorescence spectra of QD-PEG-NH₂ and QD-sEVs.

4.2.3 Visualization, confirmation, and stability of QD-sEV conjugates

We directly visualized QD-EV conjugates through TEM and fluorescent imaging to confirm successful labeling. TEM images show colocalization of QD and sEVs, with QDs on the surface of sEVs (white arrow, Figure 11A). QDs presented as black dots with great contrast (Figure 11A left panel), while sEVs presented as cap or circular shape membrane structures (Figure 11A middle panel), as described in literature.³⁶ QD-sEV conjugates presented as low contrast EVs with size 100-200 nm containing black dots of QDs (Figure 11A right panel). At a higher resolution, QDs were shown to be distributed around the surface of an individual EV (Figure 11A right panel insert). sEVs displayed similar morphology before and after QD tagging. Colocalization of QD-sEVs was also confirmed with fluorescence microscopy by visualizing overlapping signals of SYTO RNASelect stained sEVs (green) and the QDs (red) (Figure B1). Additionally, we visually confirmed QD-sEVs can be imaged in a biologically relevant system. QD-sEV treated human vaginal epithelial sheets presented distinctive fluorescent dots (Figure B2A). Tissue treated with pQDs, taken from f7-f9 from SEC on QD-4FB samples, did not show signal (Figure B2B). Note the vaginal tissue has autofluorescence which can be detected as diffuse signal under the same laser setting as QDs. However, compared to tissue autofluorescence, QD-sEVs were punctate and brighter in fluorescence intensity.

The QD-EV conjugates must remain stable in physiological media over a time relevant to imaging applications. In addition, the QD-EV conjugates need to be stable during storage. Our previous publication indicates PEGylated QDs should remain stable without significant aggregation at

physiological temperature for at least 24 h.¹²² Previous literature shows EVs are physically stable when stored at 4°C for months.^{146, 147} We confirmed sEVs remain stable at 4°C after a 25-day storage period (Figure B3). In addition to the stability of QDs and EVs, the bonds that connect QDs and EVs should remain intact during application or storage. We tested the 4FB-HyNic bond stability by measuring the change of bond quantity, which was indicated by the ratio of the bond detected at different time points to the bond detected at 0 h. We tested the bond stability in three different media, including 1xPBS, 1xPBS+10%FBS as a serum-rich environment, and in aCSF for a more complex multi-ion condition. Stability was tested at 4°C, 23°C and 37°C temperature for all media (Figure B4). The 4FB-HyNic bond was relatively stable in all conditions over 1 week of incubation or storage (Figure B4A-C). In several testing conditions, we found an increase in bond quantity over the initial 24 hours, which could be due to the continuous 4FB and HyNic reaction (Figure S4D-E). In 1xPBS+10%FBS conditions, the %bond began to drop at 2 d (Figure B4B), while in 1xPBS conditions, especially at 4°C, the %bond remained approximately the same, with a slight increase from 1 d to 1 week (Figure B4A). The decrease in the % bond after 1 d at 37°C is likely due to hydrolysis of hydrophilic Sulfo-NHS ester, which results in an unstable sulfo-NHS reactive group. When the sulfo group is hydrolyzed, the bis-aryl hydrazone becomes more hydrophobic, decreasing hydrazone stability in solution. However, when there is an amine present during QD-EV conjugation, a stable amide linker will be formed,¹⁴⁸ minimizing the effect of hydrolysis. Although this stability study was only done on the bonds without QDs or EVs present, the results indicate that QDs and EVs should remain conjugated with a stable 4FB-HyNic bond in storage conditions such as 1xPBS at 4°C for at least 1 week. Moreover, QDs and EVs should remain stably-labeled during imaging on cells or *ex vivo* tissue, or even *in vivo*, in a physiological preferred environment in a 24-hour window.

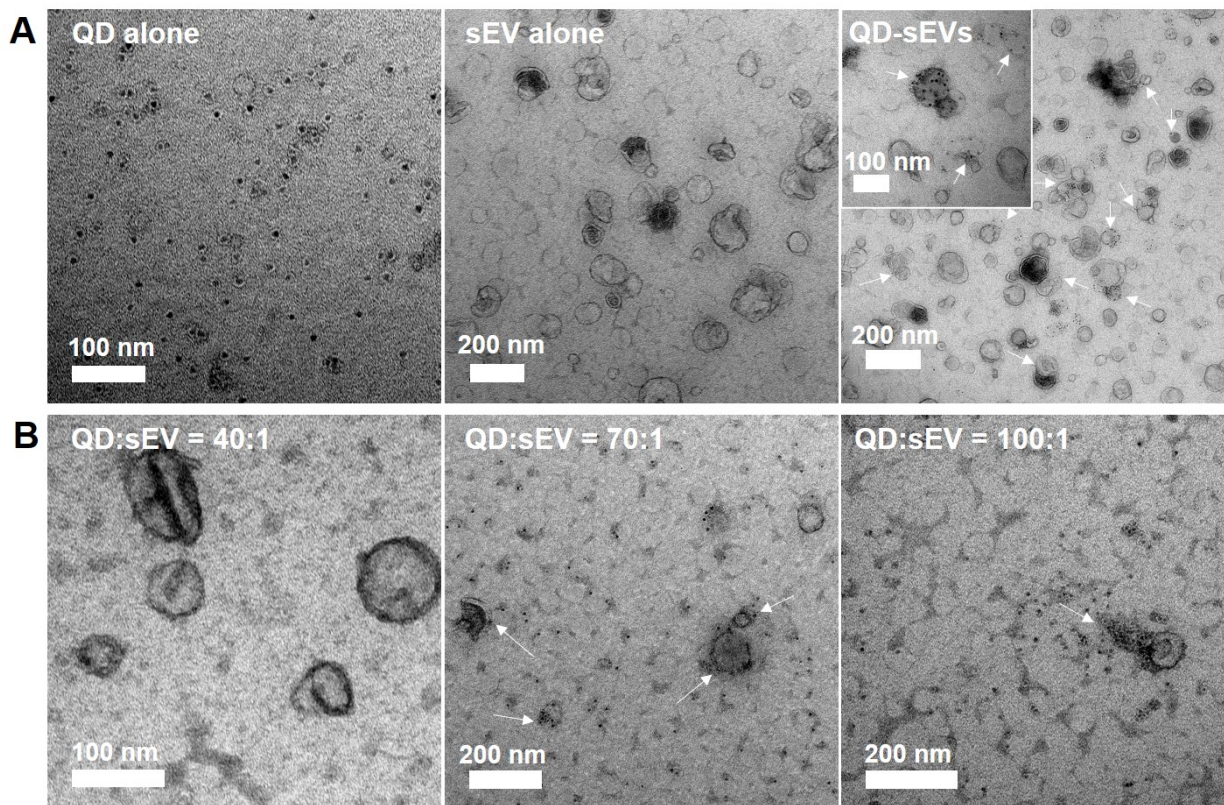


Figure 11. TEM imaging of QDs, sEVs, and QD-sEVs.

(A) QDs, sEVs, and QD-sEVs conjugates were imaged using TEM. QDs alone (left panel), sEVs alone (middle panel) and QD-sEV conjugates (right panel) were presented. QDs on the surface of sEVs are pointed out by white arrows. A magnified TEM image further indicates colocalization of QDs and sEVs at the single EV level (right insert). Scale bar: 100 nm in left panel, 200 nm in middle and right pane, and 100 nm in right insert. (B) QDs were conjugated to sEVs using click chemistry in varying ratios of QD to sEV and imaged using TEM. QD:sEV ratios of 40:1 (left), 70:1 (middle), 100:1 (right) were evaluated. Altering QD:sEV ratio changes the uniformity of QD distribution on the sEV surface. White arrows point out QDs on the surface of sEVs. Scale bars: 100 nm in left panel, 200 nm in middle and right panel.

4.2.4 Optimizing QD-EV conjugation by altering QD distribution on EVs and increasing reaction efficiency

For optimal performance of QD-EV conjugates in biological applications, we proposed that the QD distribution on EVs needs to be uniform and non-aggregated. We hypothesized the QD to EV

ratio may influence the final QD-EV conjugate distribution. To look at this, we engineered the stoichiometric ratio of input QD-PEG-NH₂ and sEVs as 40:1, 70:1, 100:1. To make the ratio of QDs to sEVs the only variable throughout the experiment, we kept the number of Sulfo-S-4FB per QD (3.58×10^5) and Sulfo-S-HyNic per EV (1.28×10^6) constant across all three experimental groups during reaction. TEM images were taken to identify the QD distribution on sEVs (Figure 11B). No QD-sEV conjugates were visualized in the 40:1 sample (Figure 11B left panel), while a rather uniform distribution of QDs to sEVs was achieved in the 70:1 sample, as indicated by the white arrows showing fully intact sEVs with QDs present (Figure 11B middle panel). At higher QD:sEV ratios (100:1), aggregation of QDs on the sEV surface occurred, as indicated by the white arrow (Figure 11B right panel). These findings indicate that altering QD to EV ratio can change the QD distribution on sEVs. For further experiments in this study, we used the 70:1 ratio during QD-EV conjugation due to the uniform distribution of QDs on the EV surface achieved at that ratio.

We next explored the use of catalysts to increase the conjugation efficiency. We used two catalysts in the reaction: 3,5-DABA and 5-MA, both of which accelerate the hydrazone formation process.⁶⁶ We tested catalyst impact on the 4FB-HyNic bond formation efficiency by monitoring the absorbance at 354 nm for 2 h as an indicator of quantity of bonds. High concentration (10 mM) of both catalysts accelerated the reaction immediately and increased the final bond yield 2-fold, while low concentration (1 mM) of both catalysts gradually increased bond formation during 2 h of testing, with a doubled bond yield at the end of the incubation window (Figure B5A). We found 10 mM 5-MA resulted in precipitation during 3 h incubation with the 4FB and HyNic mixture, thus we chose to pursue the catalyst study with 1 mM of both catalysts. We then evaluated the impact of pH on 4FB-HyNic bond formation at a pH range of 6-7 (Figure B5B,C). A wider range

of pH was not tested due to potential impact on EV integrity.¹⁴⁹ No significant difference in bond formation efficiency was observed at different pH values. Therefore, we chose the combination of pH 7.4 and 1 mM 5-MA as the catalyst condition. We estimated an average 6.5 QDs on each sEV with a catalyzed reaction, which is a 3-fold increase QD to EV ratio compared to QD-sEV conjugates without catalyst (an average of 2 QDs on each sEV). However, because an additional purification step was needed for catalyzed QD-EVs to separate out excess catalysts, final sEV retention – the amount of sEVs in the final conjugate compared to the initial input of sEVs – in catalyzed QD-EV conjugates was only 2.7%, which is 2-fold lower compared to a recovery of 4.4% in uncatalyzed QD-EV conjugates. Considering that it is necessary to reduce conjugate loss following the conjugation process, we proceeded to conjugate QDs and EVs without catalyst for further study. Nevertheless, for QD-EV applications that require higher conjugation efficiency, utilizing catalysts such as 1 mM 5-MA to boost hydrazone formation is an option.

4.2.5 Investigating bEVs interaction with BV-2 cells through QD-bEV conjugates

After confirming QD-EV conjugates are tailorable and stable, we expanded the investigation to imaging capability. We demonstrated the ability to tag QDs on EVs using human sEVs as model EVs. We next sought to confirm that our conjugation scheme could be applied to other EV populations. Here, we isolated bEVs from excised whole rat brain using a modified protocol,⁶³ detailed in our methods. Isolating EVs from the whole animal brain is different from commonly studied cell- or fluid-derived EVs, but enables us to study tissue-based EVs representative of heterogeneous EV populations. Sucrose density gradient purification of EVs often suffers from protein contamination¹⁵⁰ that could lead to false positive signals, so we opted to use SEC for final purification of bEVs.¹¹⁹ Thus, we opted to use SEC for final purification of bEVs. f7-f10 contained

the majority of bEVs (Figure 12A) and also had the highest particle to protein ratio (Figure 12B). We confirmed successful modification on bEV-HyNic by UV-vis spectroscopy; similar to sEV-HyNic (Figure 12B), an increase of absorbance of bEV-HyNic + 4FB was observed (Figure 12C). The average size of bEV-HyNic measured by NanoSight was 195.8 nm and the average size of QD-bEVs was 277.9 nm (Figure 12D). The broad size distribution of bEV-HyNic and QD-bEVs could be due to the heterogeneities of tissue-based EVs (Figure 12D). The zeta potential of bEV-HyNic was -16.4 mV and the zeta potential of QD-bEV was -10.6 mV (Figure 12E).

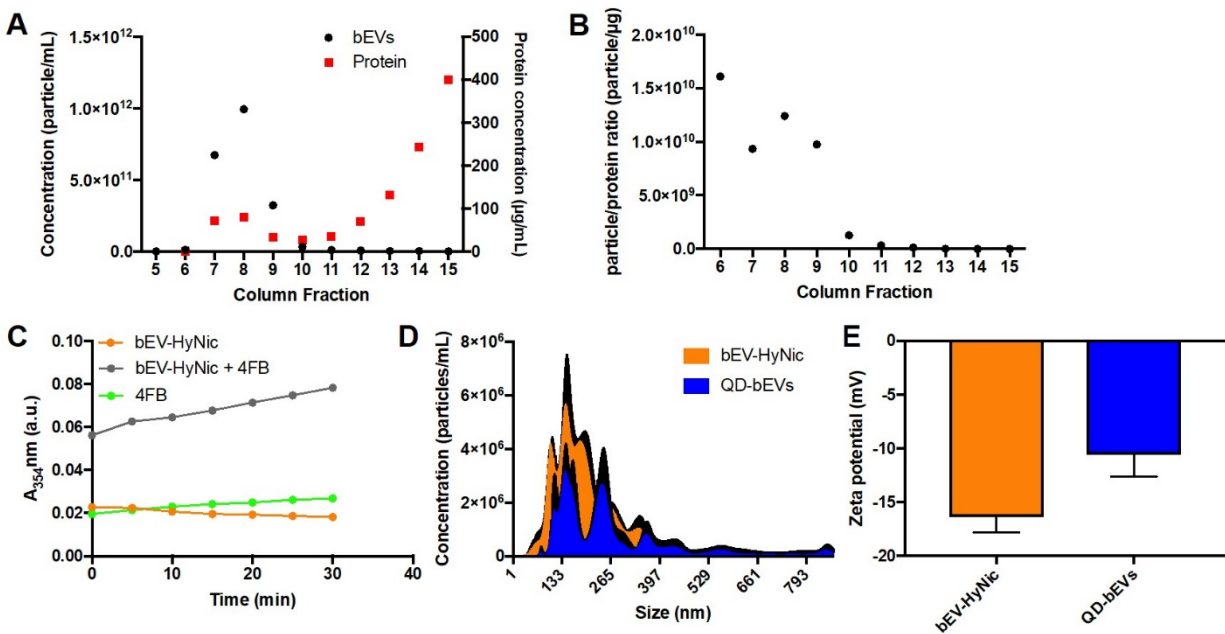


Figure 12. Characterization of QD-bEV conjugates.

(A) Representative data of bEV particle quantity (black) and protein concentration (red) in f5-f15 of qEV column purification. f7-f10 contained both bEVs and proteins while f12-f15 only contain proteins. (B) Representative data of particle/protein ratio of bEVs in f6-f15. f7-f10 contain the majority of pure bEVs and were collected for further conjugation experiments. (C) Absorbance intensity at 354 nm of Sulfo-S-4FB, bEV-HyNic and Sulfo-S-4FB + bEV-HyNic during the first 30 min after chemical mixing (n=3). bEV-HyNic modification was confirmed by increased absorbance at 354 nm. (D) Size distribution of bEV-HyNic and QD-bEV (n=3) – black lines represent SEM for each size reported. (E) Zeta potential of bEV-HyNic and QD-bEV conjugates in 1xPBS (n=3).

The greatest advantage of using QDs for bioimaging over traditional organic dye is the strong resistance to photobleaching.¹² To further investigate this, we compared the photostability of QD-bEVs and bEVs labeled with the commonly used lipophilic membrane dye DiI (DiI-bEVs). Both labeled bEVs were incubated with BV-2 cells for 24 h, followed by 10 min imaging under continuously laser exposure. The fluorescence intensity of QD-bEVs remained the same, while the intensity of DiI-bEVs dropped ~50% during the imaging window (Figure 13A,B). This shows that QD-EV conjugates could favor *in vitro* or *in vivo* studies that necessitate long-term or repetitive imaging.

As an example, QD labeling of bEVs can contribute to studying single bEV-single cell interaction with cells in the CNS. Brain-derived EVs play an important role in modulating neuroinflammation and the progression of neurological diseases,⁴⁴⁻⁴⁸ necessitating the study of brain EVs for potential treatment or early diagnosis of brain disorders. Within the CNS, microglia are the brains' innate immune cells and are known regulators of neuroinflammation,⁵⁶ which are of particular interest for studying CNS diseases and neurotherapeutic targets. These cells also serve as an important source for and recipient of EVs in the brain.¹⁵¹ We chose microglial BV-2 cells, a commonly-used murine microglia cell line, to study the interaction with QD-bEVs. When applied to BV-2 cells, QD-bEVs were observed as individual bright dots well-distributed on the surface of BV-2 cells after 24 h of incubation (Figure 13C,D). To determine if unconjugated QDs were able to elute in EV fractions during SEC, we also treated BV-2 cells for 24 h with pQDs. As expected, pQD treated BV-2 cells did not present any distinctive QD signals under the same imaging settings compared to QD-bEV treated BV-2 cells (Figure 13E). This indicated that SEC successfully separates QD-EVs and unconjugated QDs, resulting in SEC purified QD-EVs that can be used for imaging

without unconjugated QDs generating false positive signals. In addition, we were able to visualize bEVs co-localizing with the BV-2 cell membrane at a single cell resolution (Figure 13D).

Another beneficial application of the QD-EV conjugate is for live sample imaging, which can monitor the interaction of QD-EVs with cells under a microscope over hours. To gain a preliminary insight into the ability to time-lapse image QD-EV conjugates, we acquired time-lapse videos of QD-bEVs interaction with microglial cells at multiple time points of incubation. QD-bEVs were observed to move towards BV-2 cells and interact with the cell surface within 1 h of incubation, while a subfraction of bEVs were found already associated with BV-2 cells (Movie B1, Figure B6A). After 4 h of incubation, QD-bEVs continued to associate with BV-2 cells (Movie B2, Figure B6B). Moreover, BV-2 cells that have QD-bEVs associated on their surface continued to migrate, indicating QD-bEVs did not interfere with the mobility of BV2 cells (Movie B3, Figure B6C). Quantitative analysis of these videos indicated bEVs exhibited a significantly higher cumulative interaction with BV-2 cells at 4 h compared to 1 h of contact (Figure B7). More studies need to be done to further investigate the mechanism of this time-dependent EV-cell interaction, including considering cell proliferation, synthesis and release of new QD-EVs after QD-EVs integration on cell membrane, and potential QD degradation in lysosomes. Future use of QD-EV conjugates can also include single or multiple particle tracking of QD-labeled EVs at high frame rates, which can capture the kinetic profile of EV mobility as well as more detailed interaction with cells. The high photostability of QD-EVs compared to traditionally labeled EVs thus could be a benefit for this application.

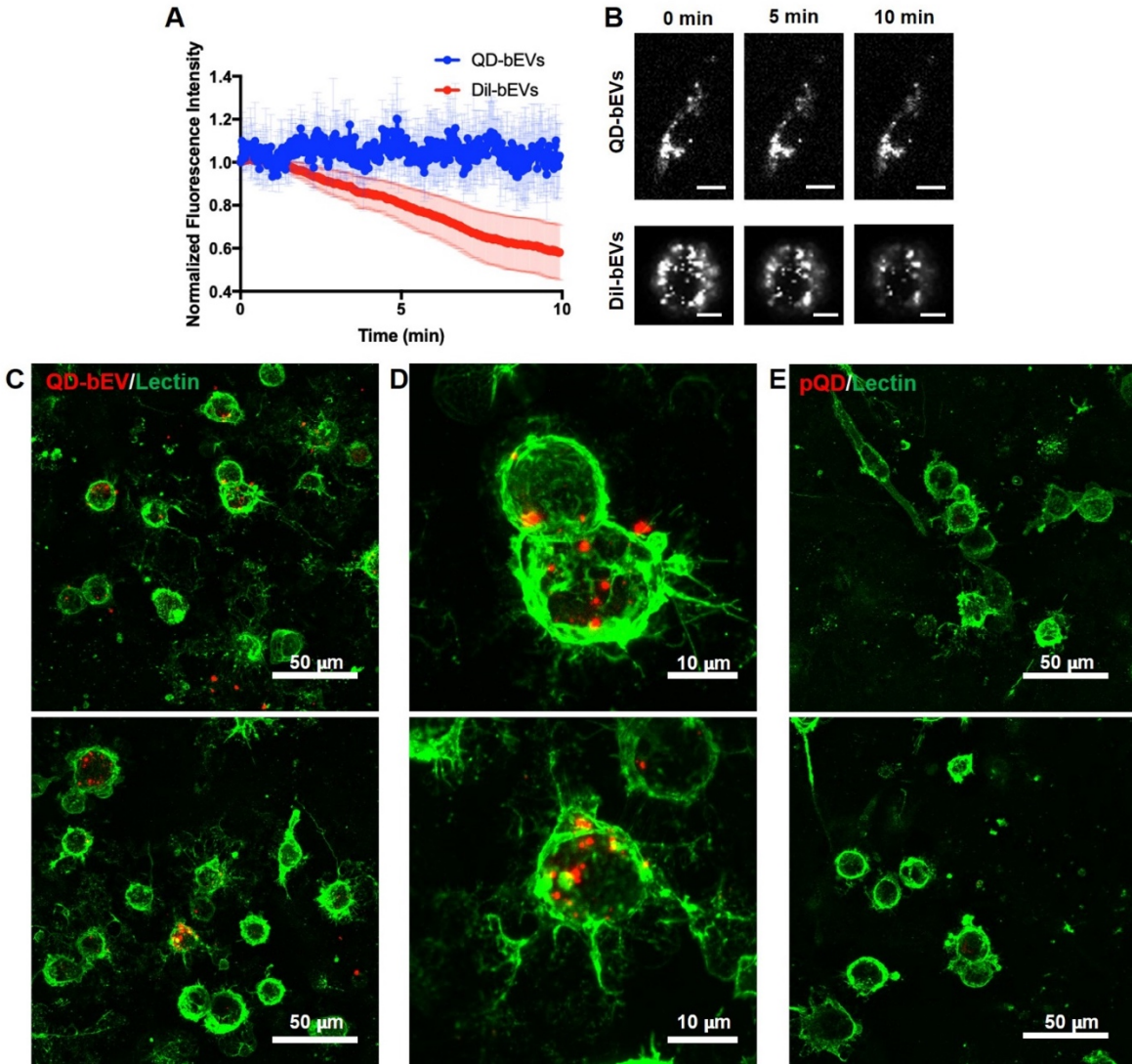


Figure 13. Photostability and imaging of QD-bEVs on BV-2 cells.

(A) The fluorescence intensity of QD-bEVs (n=6) and DiI-bEVs (n=3) during 10 min laser exposure under the same laser power. (B) Representative images of QD-bEVs on single BV-2 cell (top) and DiI-bEVs on single BV-2 cell (bottom) at 0 min, 5 min, and 10 min of laser exposure. Images were converted to grayscale for better visualization. Scale bars: 10 μ m. (C) Representative 60x maximum intensity projection images of QD-bEVs (red) distribution and cellular interaction on Lectin stained BV-2 cells (green). Scale bars: 50 μ m. (D) Higher magnification of an area in (C). QD-bEVs localized on the BV-2 cell membrane and throughout the individual cell. Scale bars: 10 μ m. (E) Representative 60x maximum intensity projection images of pQDs (red) negative control distribution and cellular interaction on Lectin stained BV-2 cells (green). No obvious QD signals were found on BV-2 cells using the same laser power and

imaging settings as (C-D), indicating unconjugated QDs can be successfully removed through SEC purification. Scale bars: 50 μm .

4.3 Conclusion

Using 4FB-HyNic click chemistry, we were able to develop a robust, universal, controllable, and biologically stable QD-EV conjugate. This QD-EV conjugate showed greater resistance to photobleaching compared to EVs labeled with DiI, a commonly used EV staining dye. The successful conjugation of QDs and EVs was confirmed through TEM, UV-vis spectroscopy, DLS, and confocal microscopy. The QD-EV conjugation can be optimized through altering the initial QD to EV ratio as well as utilizing catalysts for accelerating the hydrazone formation process. The QD-EV conjugation bonds were stable in various biological media and storage conditions for at least a week, providing flexibility for applications. In addition, we showed that SEC was able to separate EVs from free proteins, as well as QD-EV conjugates from unconjugated QDs. More importantly, the QD-EV conjugates demonstrated high resolution live imaging ability on EVs *in vitro* and fixed imaging ability *ex vivo*. We were able to live image the association of bEVs with BV-2 microglial cell membrane, and image the co-localization of sEVs with human vaginal cells in fixed tissue sections. This method of labeling EVs provides a new way of visualizing and studying EV behavior, which can be an important tool for the fundamental understanding of EVs and their potential clinical application.

CHAPTER 5: Research Summary

5.1 Quantum dot labeling and visualization of extracellular vesicles

Zhang M, Vojtech L, Ye Z, Hladik F, Nance E*. *ACS Applied Nano Materials*. (2020) 3(7), 7211-7222.

*Corresponding author

Extracellular vesicles (EVs) are important mediators of intercellular communication. Their role in disease processes, uncovered mostly over the last two decades, makes them potential biomarkers, leading to a need to fundamentally understand EV biology. Direct visualization of EVs can provide insights into EV behavior, but current labeling techniques are often restricted by false positive signals and rapid photobleaching. Hence, we developed a method of labeling EVs through conjugation with quantum dots (QDs) – high photoluminescent nano-sized semiconductors – using click chemistry. We showed that QD-EV conjugation could be tailored by altering QD to EV ratio or by using a catalyst. This conjugation chemistry was stable in a biological environment and upon storage for up to a week. Using size exclusion chromatography, QD-EV conjugates could be separated from unconjugated QDs, enabling EV-specific signal detection. We demonstrate that these QD-EV conjugates can be live- and fixed-imaged in high resolution on cells and in tissue sheets, and the conjugates have better photostability compared to the commonly used EV dye DiI. We labeled two distinct EV populations: human semen EVs (sEVs) from fresh semen samples donated by healthy volunteers and brain EVs (bEVs) from excised rat brain tissues. We visualized QD-sEVs in epithelial sheets isolated from human vaginal mucosa, and time-lapse imaged QD-bEV interactions with microglial BV-2 cells. The development of the QD-EV conjugate will

benefit the study of EV localization, movement and function, and accelerate their potential use as biomarkers, therapeutic agents or drug delivery vehicles.

5.2 Quantum dot cellular uptake and toxicity in the developing brain: implications for use as imaging probes

Zhang M, Bishop B, Thompson N, Hildahl K, Dang B, Mironchuk O, Chen N, Aoki R, Holmberg V*, Nance E*. *Nanoscale Advances*. (2019) 1(9), 3424-3442.

*Corresponding author

Nanometer-sized luminescent semiconductor quantum dots (QDs) have been utilized as imaging and therapeutic agents in a variety of disease settings, including diseases of the central nervous system. QDs have several advantages over traditional fluorescent probes including their small size (5-10 nm), tunable excitation and emission spectra, tailorable surface functionality, efficient photoluminescence, and robust photostability, which are ideal characteristics for *in vivo* imaging. Although QDs are promising imaging agents in brain-related applications, no systematic evaluation of QD behavior in brain-relevant conditions has yet been done. Therefore, we sought to investigate QD colloidal stability, cellular uptake, and toxicity *in vitro*, *ex vivo*, and *in vivo* in the brain environment. We found that QD behavior is highly dependent on surface functionality and that treatment of cultured organotypic whole hemisphere (OWH) slices with QDs results in dose-dependent toxicity and metallothionein increase, but no subsequent mRNA expression level changes in inflammatory cytokines or other oxidative stress. QDs coated with poly(ethylene glycol) (PEG) were protected from aggregation in neurophysiologically relevant fluids and in tissue, allowing for greater penetration. Importantly, QD behavior differed in cultured slices as compared to monolayer cell cultures, and behavior in cultured slices aligned more closely with that seen *in vivo*. Irrespective of surface chemistry and brain-relevant platform, non-aggregated QDs were primarily internalized by microglia in a region-dependent manner both in slices and *in vivo* upon

systemic administration. This knowledge will help guide further engineering of candidate QD-based imaging probes for neurological application.

5.3 Nanoparticle-microglia interaction in the ischemic brain is modulated by injury duration and treatment

Joseph A, Liao R, Zhang M, Helmbrecht H, McKenna M, Filteau J, Nance E*. *Bioengineering & Translational Medicine*. (2020), e10175.

*Corresponding author

Cerebral ischemia is a major cause of death in both neonates and adults, and currently has no cure. Nanotechnology represents one promising area of therapeutic development for cerebral ischemia due to the ability of nanoparticles to overcome biological barriers in the brain. *Ex vivo* injury models have emerged as a high-throughput alternative that can recapitulate disease processes and enable nanoscale probing of the brain microenvironment. In this study, we used oxygen–glucose deprivation (OGD) to model ischemic injury and studied nanoparticle interaction with microglia, resident immune cells in the brain that are of increasing interest for therapeutic delivery. By measuring cell death and glutathione production, we evaluated the effect of OGD exposure time and treatment with azithromycin (AZ) on slice health. We found a robust injury response with 0.5 hours of OGD exposure and effective treatment after immediate application of AZ. We observed an OGD-induced shift in microglial morphology towards increased heterogeneity and circularity, and a decrease in microglial number, which was reversed after treatment. OGD enhanced diffusion of polystyrene-poly(ethylene glycol) (PS-PEG) nanoparticles, improving transport and ability to reach target cells. While microglial uptake of dendrimers or quantum dots (QDs) was not enhanced after injury, internalization of PS-PEG was significantly increased. For PS-PEG, azithromycin (AZ) treatment restored microglial uptake to normal control levels. Our results suggest that different nanoparticle platforms should be carefully screened before

application and upon doing so, disease-mediated changes in the brain microenvironment can be leveraged by nanoscale drug delivery devices for enhanced cell interaction.

5.4 Governing transport principles for nanotherapeutic application in the brain

Helmbrecht H, Joseph A, McKenna M, Zhang M, Nance E*. *Current Opinions in Chemical Engineering*. (2020)

*Corresponding author

Neurological diseases account for a significant portion of the global disease burden. While research efforts have identified potential drugs or drug targets for neurological diseases, most therapeutic platforms are still ineffective at reaching the target location selectively and with high yield. Restricted transport, including passage across the blood-brain barrier, through the brain parenchyma, and into specific cells, is a major cause of ineffective therapeutic delivery. However, nanotechnology is a promising, tailorable platform for overcoming these transport barriers and improving therapeutic delivery to the brain. We provide a transport-oriented analysis of nanotechnology's ability to navigate these transport barriers in the brain. We also provide an opinion on the need for technology development for increasing our capacity to characterize and quantify nanoparticle passage through each transport barrier. Finally, we highlight the importance of incorporating the effect of disease, metabolic state, and regional dependencies to better understand transport of nanotherapeutics in the brain.

5.5 Intratumoral nanofluidic system for enhancing tumor biodistribution of agonist CD40 antibody

Chua C, Ho J, Susnjar A, Lolli G, Di Trani N, Pesaresi F, Sizovs A, Zhang M, Nance E, Grattoni A*. *Advanced Therapeutics*. (2020), 2000055.

*Corresponding author

Tumor uptake and biodistribution of immunotherapy is associated with clinical response as well as toxicity. To augment immunotherapy bioavailability in the tumor, an intratumoral administration route via direct injection or local release technologies has emerged as an appealing approach. Here the biodistribution of an agonistic anti-CD40 monoclonal antibody (CD40 mAb) when sustainably delivered via an intratumoral nanofluidic drug-eluting seed (NDES) is evaluated in comparison to systemic or direct intratumoral administration. The NDES achieves sustained drug release through diffusion by leveraging electrostatic nanoconfinement within nanochannels, without requiring internal or external actuation. Using the 4T1 murine mammary carcinoma model, the biodistribution of Alexa Fluor-700 conjugated CD40 mAb is tracked via fluorescence imaging analysis, comparing three routes of administration over 7 and 14 days. NDES-treated cohort shows sustained high levels of intratumoral CD40 mAb without off-target organ exposure, compared to the intraperitoneal and direct intratumoral administration. Moreover, radiation pre-treatment of the 4T1 tumors augments tumor retention of CD40 mAb in the NDES group. Overall, sustained intratumoral release of CD40 mAb via the NDES improves local drug bioavailability without systemic dissemination, suggesting an enhanced approach for immunotherapy administration.

I contributed to this work by perform quantification and 3D reconstruction of CD40 volume distribution in the tumors. Brief description of the tissue processing, image analysis, and image processing, along with published data and figures, is described below (Figure C1).

5.6 Extracellular vesicles in human semen modulate antigen-presenting cell function and decrease downstream antiviral T cell responses

Vojtech L*, [Zhang M](#), Davé V, Levy C, Wang R, Calienes F, Prlic M, Hughes S, Nance E, Hladik F*. Extracellular vesicles in human semen modulate antigen-presenting cell function and decrease downstream antiviral T cell responses. *PloS one* (2019) *14*(10), e0223901.

*Corresponding author

Human semen contains trillions of extracellular vesicles (SEV) similar in size to sexually transmitted viruses and loaded with potentially bioactive miRNAs, proteins and lipids. SEV were shown to inhibit HIV and Zika virus infectivity, but whether SEV are able also to affect subsequent immune responses is unknown. We found that SEV efficiently bound to and entered antigen-presenting cells (APC) and thus we set out to further dissect the impact of SEV on APC function and the impact on downstream T cell responses. In an APC–T cell co-culture system, SEV exposure to APC alone markedly reduced antigen-specific cytokine production, degranulation and cytotoxicity by antigen-specific memory CD8⁺ T cells. In contrast, inhibition of CD4⁺ T cell responses required both APC and T cell exposure to SEV. Surprisingly, SEV did not alter MHC or co-stimulatory receptor expression on APCs, but caused APCs to upregulate indoleamine 2,3 deoxygenase, an enzyme known to indirectly inhibit T cells. Thus, SEV reduce the ability of APCs to activate T cells. We propose here that these immune-inhibitory properties of SEV may be intended to prevent immune responses against semen-derived antigens, but can be hi-jacked by genitally acquired viral infections to compromise adaptive cellular immunity.

5.7 Systems-level thinking for nanoparticle-mediated therapeutic delivery to neurological diseases

Curtis C, Zhang M, Liao R, Wood T, Nance E*. *WIREs Nanomedicine and Nanobiotechnology* (2017) 9(2), e1422.

*Corresponding author

Neurological diseases account for 13% of the global burden of disease. As a result, treating these diseases costs \$750 billion a year. Nanotechnology, which consists of small (~1–100 nm) but highly tailorable platforms, can provide significant opportunities for improving therapeutic delivery to the brain. Nanoparticles can increase drug solubility, overcome the blood–brain and brain penetration barriers, and provide timed release of a drug at a site of interest. Many researchers have successfully used nanotechnology to overcome individual barriers to therapeutic delivery to the brain, yet no platform has translated into a standard of care for any neurological disease. The challenge in translating nanotechnology platforms into clinical use for patients with neurological disease necessitates a new approach to: (1) collect information from the fields associated with understanding and treating brain diseases and (2) apply that information using scalable technologies in a clinically-relevant way. This approach requires systems level thinking to integrate an understanding of biological barriers to therapeutic intervention in the brain with the engineering of nanoparticle material properties to overcome those barriers. To demonstrate how a systems perspective can tackle the challenge of treating neurological diseases using nanotechnology, we will first present physiological barriers to drug delivery in the brain and common neurological disease hallmarks that influence these barriers. We will then analyze the design of nanotechnology platforms in preclinical *in vivo* efficacy studies for treatment of

neurological disease, and map concepts for the interaction of nanoparticle physicochemical properties and pathophysiological hallmarks in the brain.

APPENDIX A: Supplementary Figures to Chapter 3

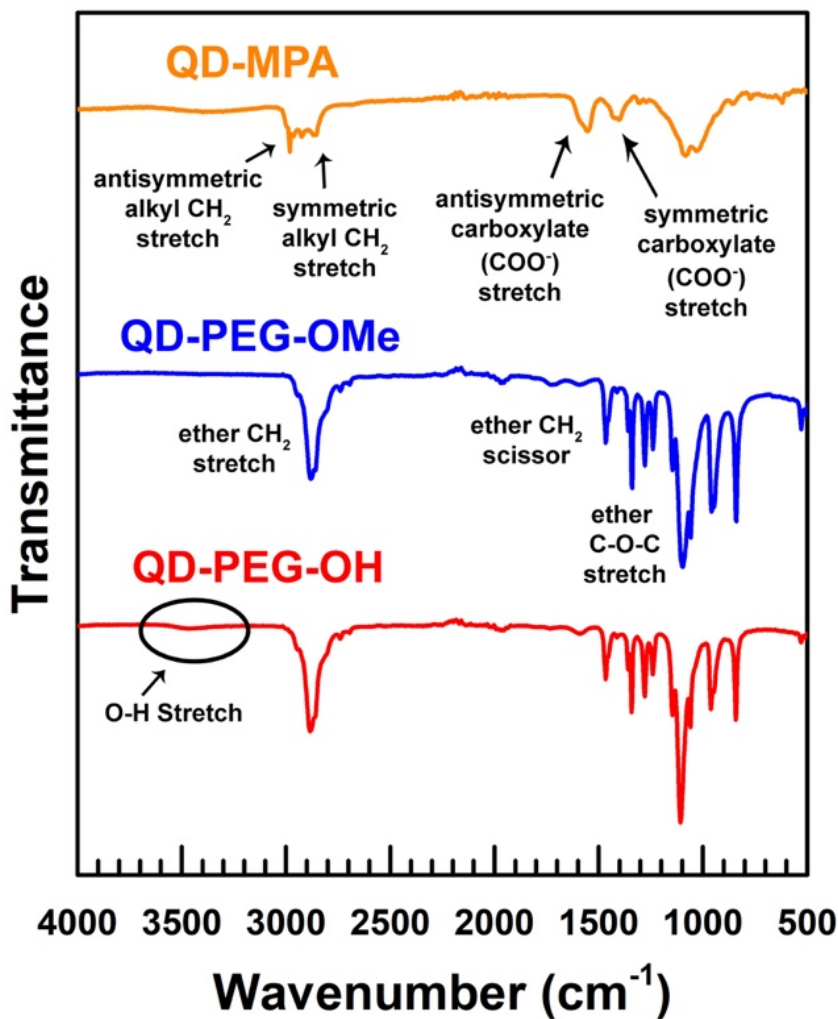


Figure A1. ATR-FTIR spectra of QD-MPA (orange), QD-PEG-OMe (blue), and QD-PEG-OH (red).

The FTIR spectra of the PEGylated QDs show the distinct features of the polyethylene glycol polymer ligand. The peak at 1100 cm⁻¹ is characteristic of an ether C-O-C band, while the peaks at 2870 and 1465 cm⁻¹ correspond to CH₂ stretching and scissoring vibrations, respectively. The remaining peaks indicate the presence of a long-chain polyether. The peaks at 1340, 1280, and 1235 cm⁻¹ are indicative of CH₂ wagging, symmetric twisting, and antisymmetric twisting, respectively. The peak at 960 cm⁻¹ corresponds to a combination of coupled symmetric CH₂

rocking, C-C stretching, and C-O stretching, while the peak at 840 cm^{-1} corresponds to coupled CH_2 rocking and C-O stretching. The QD-PEG-OH samples show an additional broad O-H stretching band extending from 3300 to 3560 cm^{-1} , which is indicative of the additional terminal O-H functional group attached to the PEG. The 3-mercaptopropionic acid-functionalized QDs exhibited characteristic antisymmetric and symmetric alkyl CH_2 stretching bands at 2920 and 2860 cm^{-1} , respectively, along with clear antisymmetric and symmetric carboxylate (COO^-) stretching bands at 1560 and 1410 cm^{-1} , respectively. These observations, in combination with the absence of a strong carboxylic acid $\text{C}=\text{O}$ stretch at 1710 cm^{-1} , indicate complete deprotonation of the carboxylic acid groups on the MPA ligands. Data provided courtesy of Brittany Bishop.

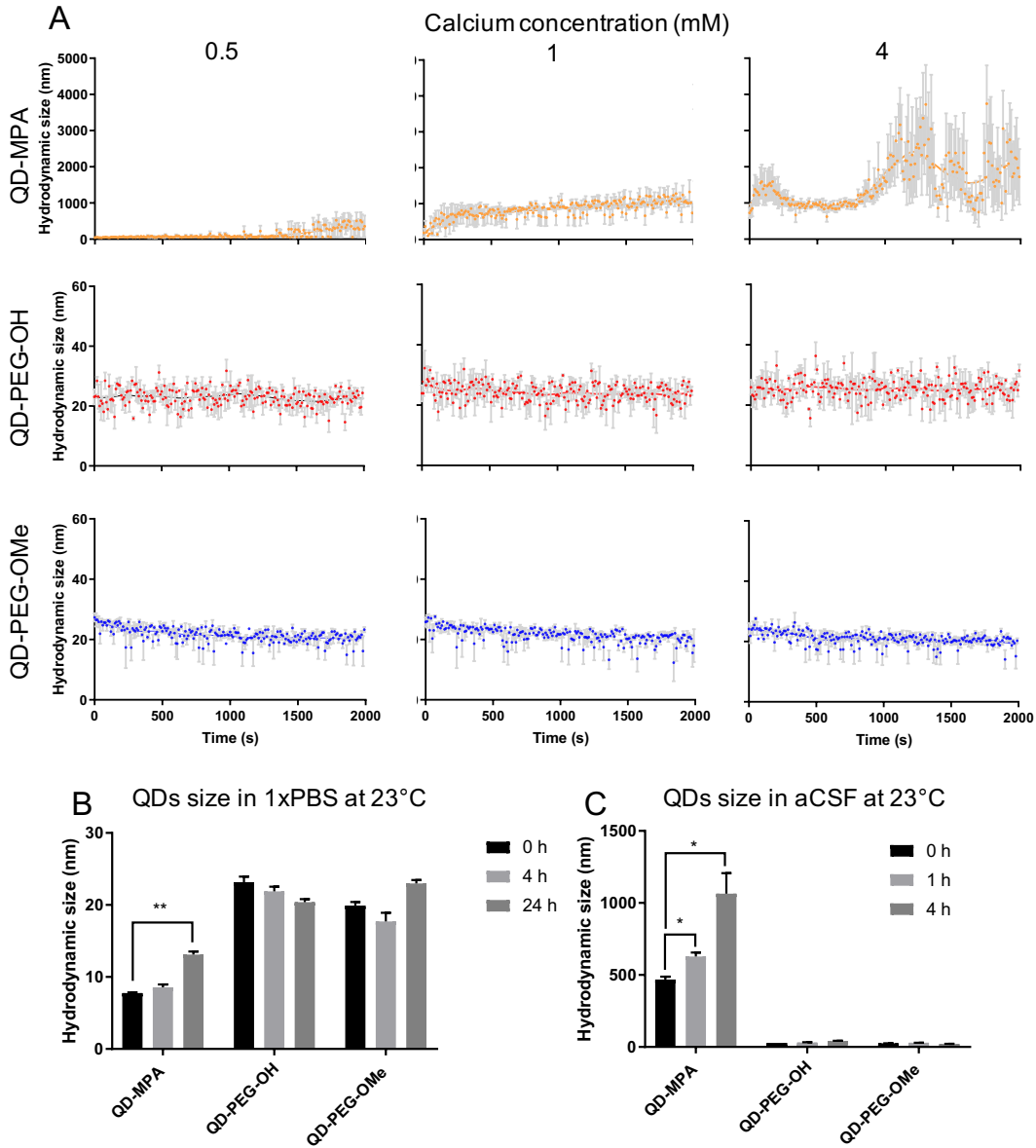


Figure A2. Colloidal stability of QDs at 23°C in neurophysiological fluids.

(A) Initial aggregation kinetics of QD-MPA, QD-PEG-OH and QD-PEG-OMe at 23°C in CaCl_2 solution with 0.5, 1, and 4 mM Ca^{2+} over a period of 2000 sec ($n=3$ measurements per particle type). Trendlines showing initial QD-MPA aggregation were generated using a LOWESS regression in GraphPad. (B) QD hydrodynamic size at 23°C in 1xPBS at 0, 4, 24 h ($n=3$ measurements per particle type). (C) QD hydrodynamic size at 23°C in aCSF at 0, 4, 24 h ($n=3$ measurements per particle type).

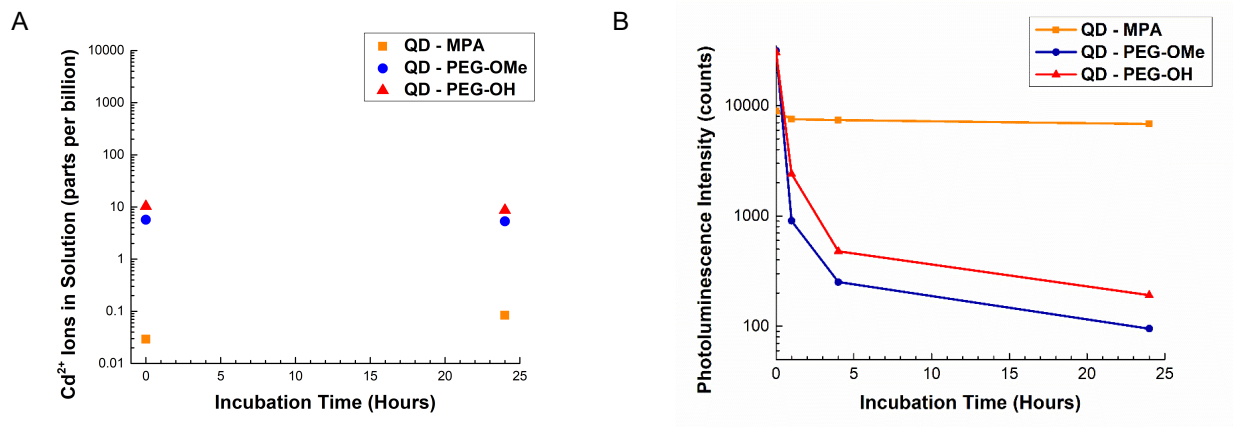


Figure A3. Cadmium ion release and QD photoluminescence change over time.

(A) Cadmium ion release of 0.1 μM CdSe/CdS QDs with different surface functionalities in aCSF at 37°C after 0 h and 24 h incubation. The level of free Cd²⁺ ions in all groups tested was less than 10 parts per billion (ppb). Note that the initial 0-h baseline levels of Cd²⁺ are due to a small subset of CdSe particles that pass through the 50-kD filter and are digested to Cd²⁺ during ICP-MS sample preparation. When a lower molecular weight cutoff filter (3 kD) was used on identical PEGylated samples, a baseline Cd²⁺ ion level of 1 ppb was achieved. The concentration of free Cd²⁺ ions remained virtually unchanged (less than 1 ppb change in concentration) for all samples over the 24-hour measurement period. (B) Photoluminescence intensity of QDs incubated in aCSF under physiological conditions as a function of time.

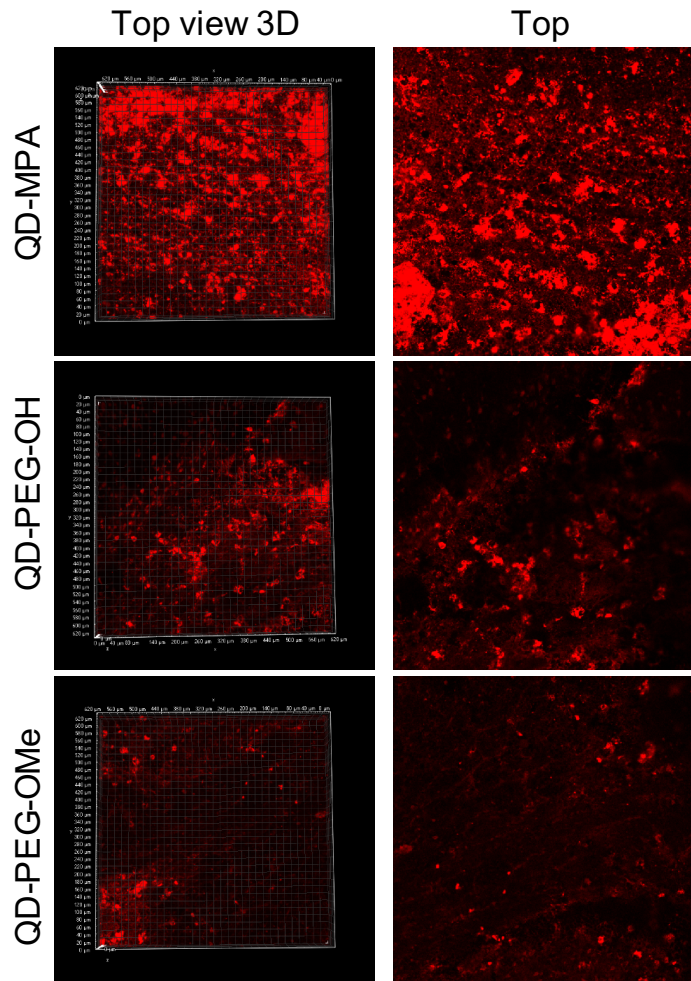


Figure A4. QD penetration in OWH slices.

QD distribution and penetration is shown at 20x magnification in 3D view (left panel) and at a single-z top view (right panel).

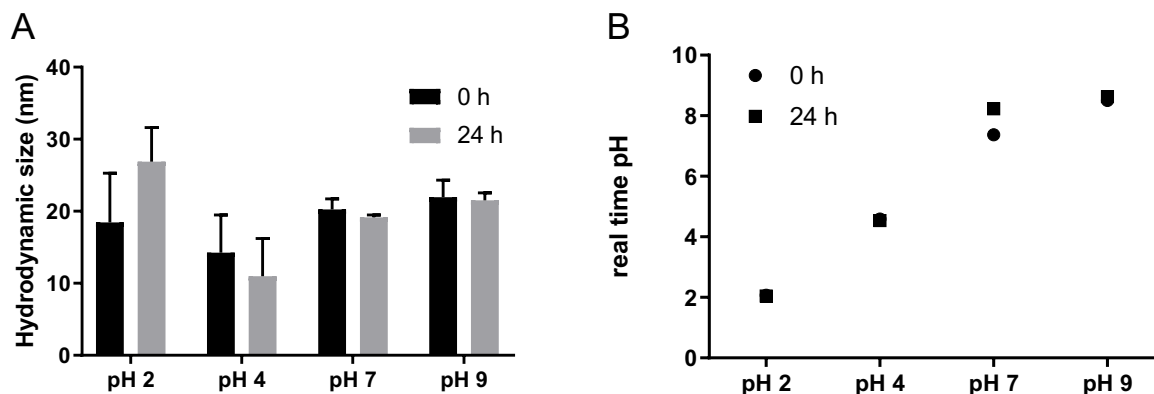


Figure A5. pH influence on QD-PEG-OMe stability in aCSF media.

(A) QD-PEG-OMe hydrodynamic size remains constant from 0 h to 24 h after incubation in aCSF at pH 2, pH 4, pH 6 and pH 9 (n = 3 measurements per condition). (B) Across the full range of pH values evaluated in this study, the pH stays constant during the experimental window (24 h incubation), even in the presence of QD addition.

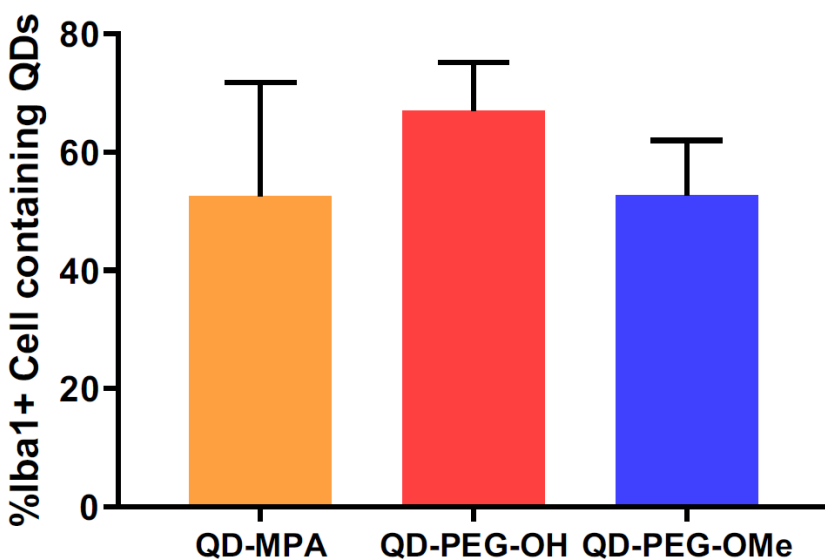


Figure A6. Fraction of Iba1+ cells containing QDs in the corpus callosum region in OWH slices.

Iba1+ microglia cells containing QDs were counted in the corpus callosum region in OWH slices and divided by the total number of Iba1+ microglia cells in the same region. n = 3 slices per QD surface functionality were evaluated. For each slice, n = 3 regions in corpus callosum were imaged for cell counting. The 3 regions evaluated were located in the same positions across all 3

slices. The percentage of Iba1+ cells containing QDs was calculated using all 3 regions of each slice, and the mean and SEOM values were calculated based on the 3 slices.

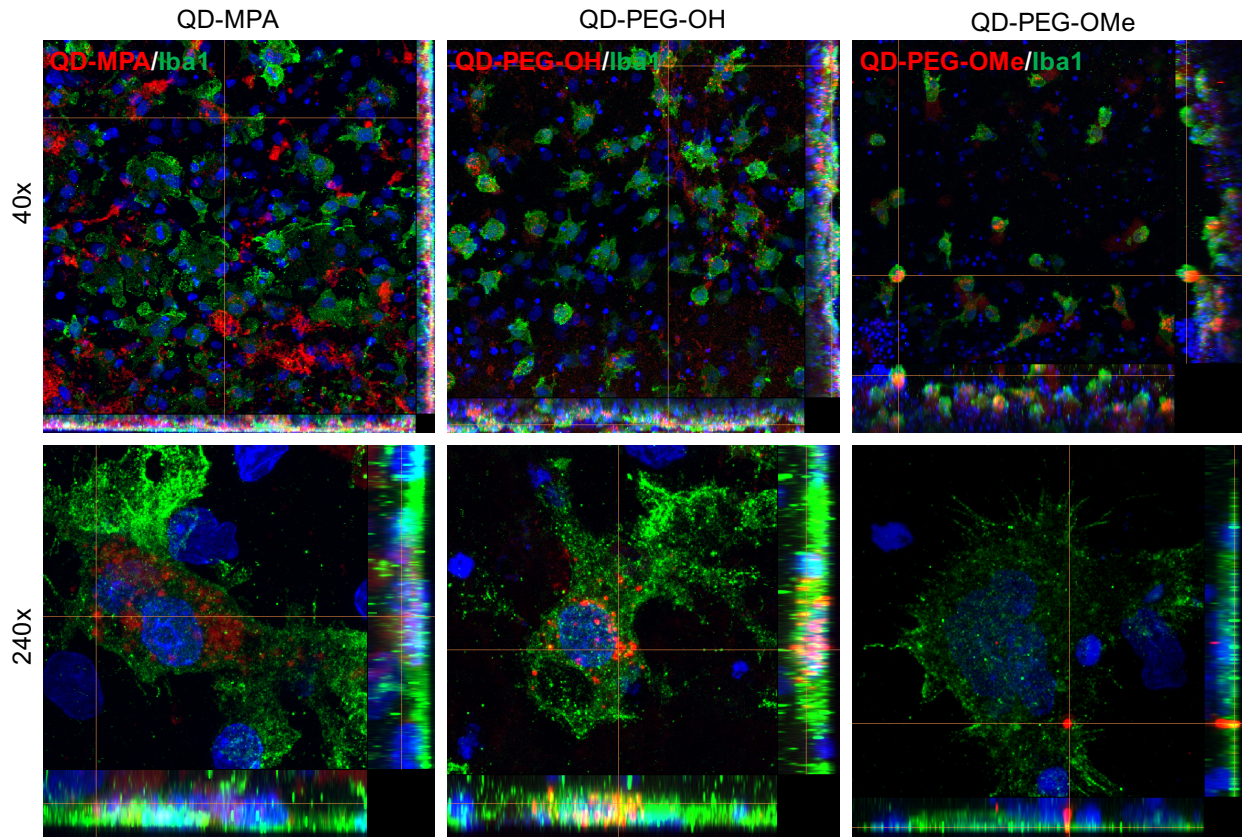


Figure A7. Cross-sectional views of z-stack confocal images of QDs colocalization with Iba1+ microglia following 24 h incubation in OWH slices.

QDs (red, all images) colocalization with Iba1+ microglia (green, all images) is confirmed by cross-sectional view of z-stack images. This colocalization analysis was performed using Nikon software. For each individual image, the line intersection in the 40x maximum intensity projected image represents the QDs selected for colocalization analysis at 240x. The right side-view images represent a “front” view and side view of the 3D z-stack image. Yellow color indicates colocalization of QDs and microglia.

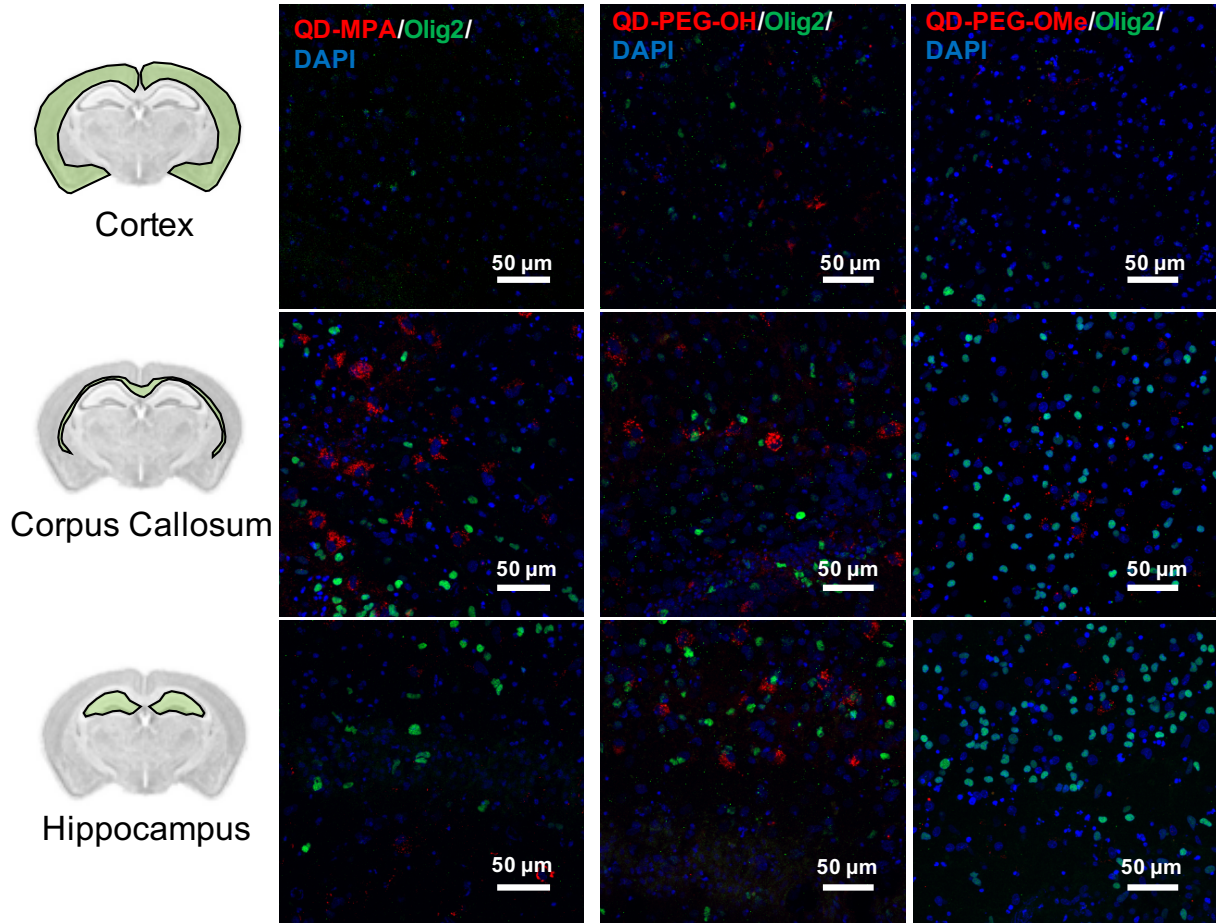


Figure A8. Olig2+ oligodendrocyte uptake of QDs in OWH slices.

40x magnification images of QD-MPA, QD-PEG-OH and QD-PEG-OMe (red, all images) distribution and interaction with Olig2+ oligodendrocytes (green, all images) in the cortex, corpus callosum, and hippocampus in P14 SD rat pup brain slices (300-μm thickness). Cell nuclei were stained with DAPI (blue).

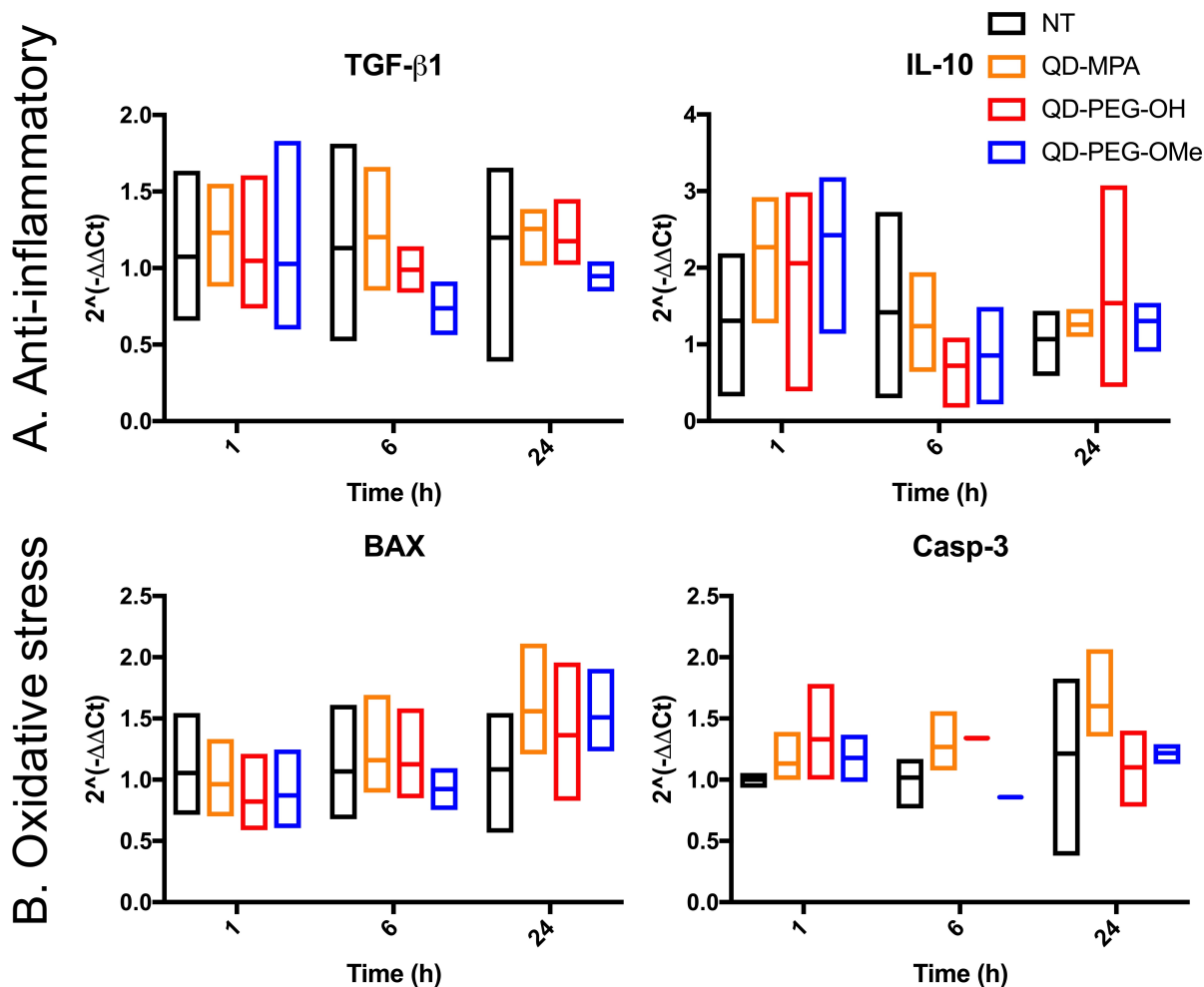


Figure A9. Time-dependent mRNA profiles of QD-induced anti-inflammatory and oxidative stress markers in OWH slices.

Fold-changes in mRNA expression were measured at 1 h, 6 h, and 24 h of QD-MPA, QD-PEG-OH, and QD-PEG-OMe exposure at 0.1 μ M concentration in OWH slices. The fold-changes were measured for (A) anti-inflammatory markers TGF β and IL-10, and (B) oxidative stress markers BAX and Casp-3. For 1 h, 6 h and 24 h time points, n = 3 groups and n = 3-6 slices per group were evaluated for each experimental sample (except for the QD-PEG-OMe 6h proinflammatory sample, where n=2 groups with n = 6 slices in total were evaluated).

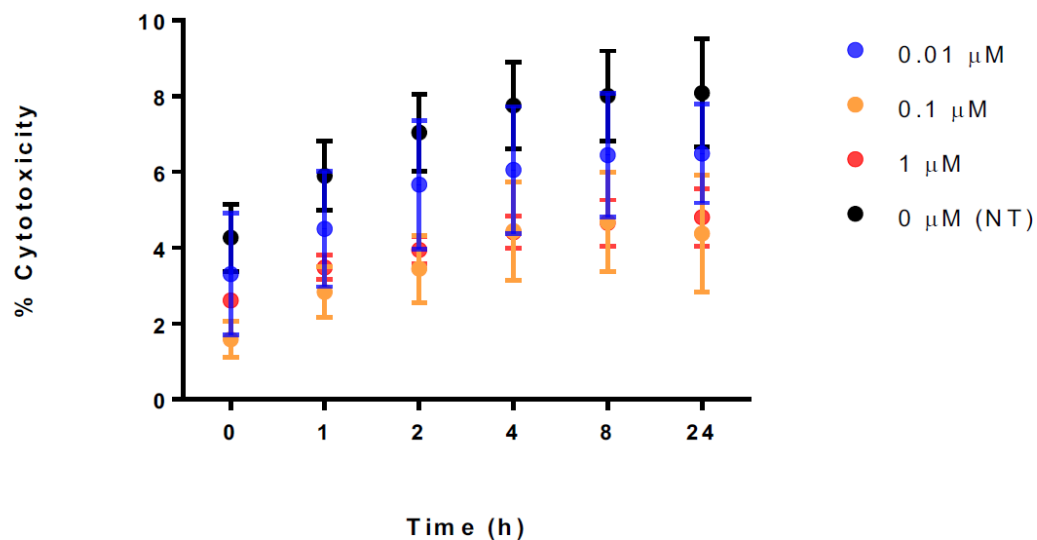


Figure A10. Dose-dependent toxicity of QD-MPA in OWH slices by LDH assay.

Treatment of QD-MPA at 0.01, 0.1, and 1 μM concentrations on P14 rat organotypic brain slices for 24 h. QD toxicity was determined by LDH assay at 0, 1, 2, 4, 8, and 24 h as follows:

%Cytotoxicity = %LDH release = $\frac{\text{Experimental release}}{\text{Maximum release}}$. For each QD concentration, n=3 slices per quantum dot type per concentration condition were evaluated; for NT group (black), n=5 slices.

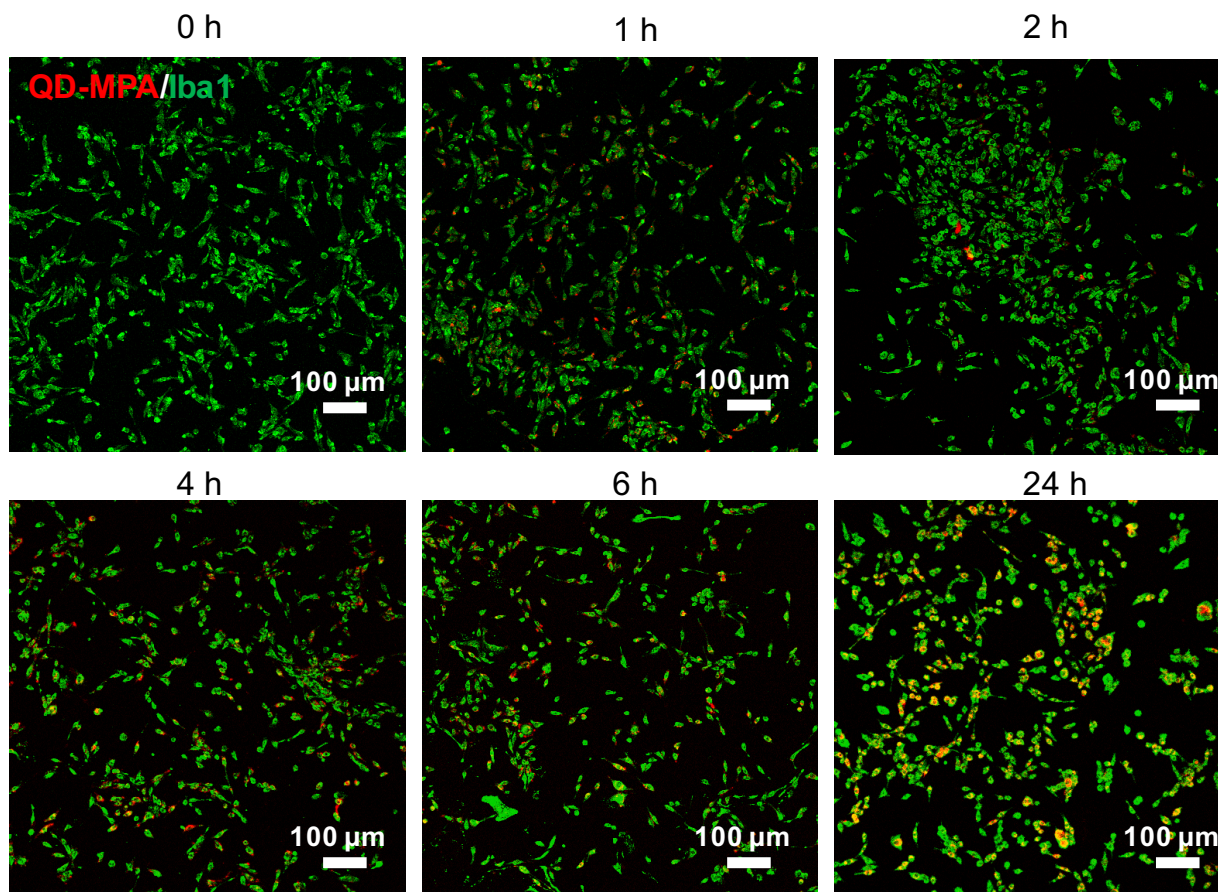


Figure A11. Cellular uptake of QD-MPA on *in vitro* BV-2 cells.

Application of QD-MPA (red, all images) at 0.01 μM concentration onto *in vitro* BV-2 cells for 1, 2, 4, 6, and 24 h. QD-MPA were taken-up into microglia (green, all images) starting at 1 h.

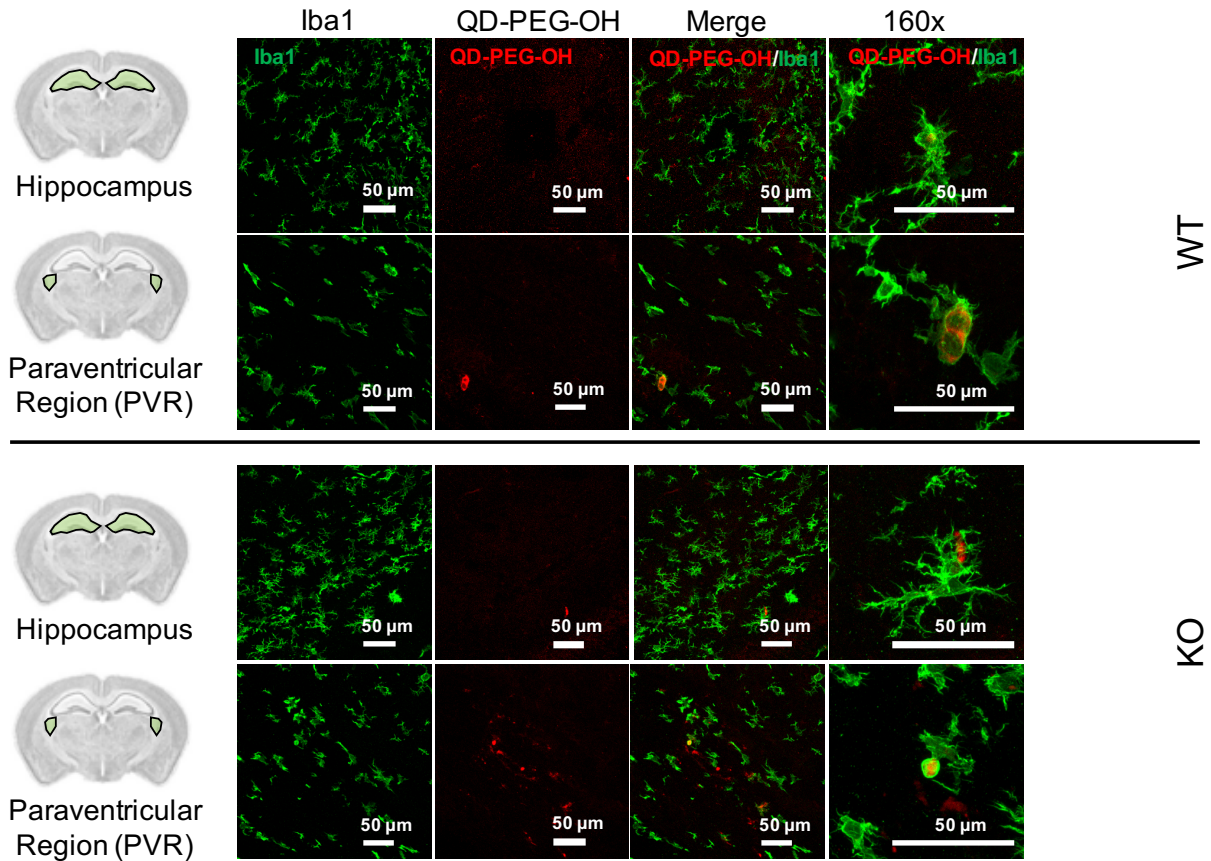


Figure A12. QD cellular uptake in hippocampus and PVR regions in P7 rats, 4 h post-administration.

Representative images of QD-PEG-OH (red, all images) colocalization with Iba1+ microglia cells (green, all images) in the hippocampus and PVR regions in P7 *mglur5* WT and KO pup brains, 4 hours after i.p. administration. 40x magnification images with 4-fold zoom (160x) are presented in the rightmost column to show QD-PEG-OH internalization in cells.

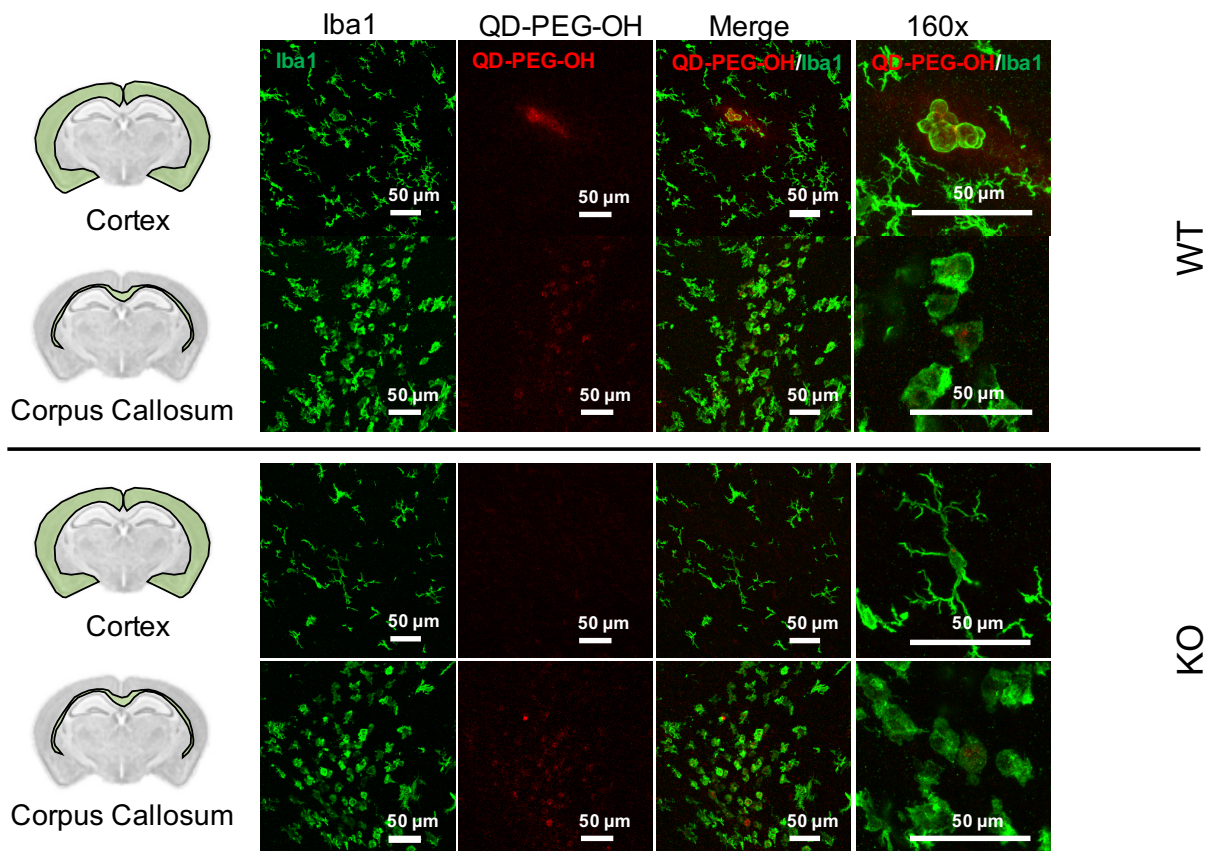


Figure A13. QD cellular uptake in P7 rats, 24 h post-administration.

Representative images of QD-PEG-OH (red, all images) colocalization with Iba1+ microglia cells (green, all images) in the cortex and corpus callosum regions in P7 *mglur5* WT and KO pup brains, 24 h after i.p. administration. 40x magnification images with 4-fold zoom (160x) are presented in the rightmost column to show QD-PEG-OH internalization in cells.

Movie A1.

Time-lapse imaging of QD-PEG-OH (red) uptake in lysosomes (green) in the corpus callosum region in live OWH slices. The video is 10 fps and will replay 5 times.

Movie A2.

Time-lapse imaging of QD-PEG-OMe (red) uptake in lysosomes (green) in the corpus callosum region in live OWH slices. The video is 10 fps and will replay 5 times.

Movie A3.

Time-lapse imaging of QD-MPA (red) uptake in CD11b+ microglia (green) in corpus callosum region in live OWH slices. The video is 5 fps and will replay 5 times.

Movie A4.

Time-lapse imaging of QD-PEG-OH (red) uptake in CD11b+ microglia (green) in corpus callosum region in live OWH slices. The video is 5 fps and will replay 5 times.

Movie A5.

Time-lapse imaging of QD-PEG-OMe (red) uptake in CD11b+ microglia (green) in corpus callosum region in live OWH slices. The video is 5 fps and will replay 5 times.

To access all the movies, see DOI: [10.1039/c9na00334g](https://doi.org/10.1039/c9na00334g)

APPENDIX B: Supplementary Figures to Chapter 4

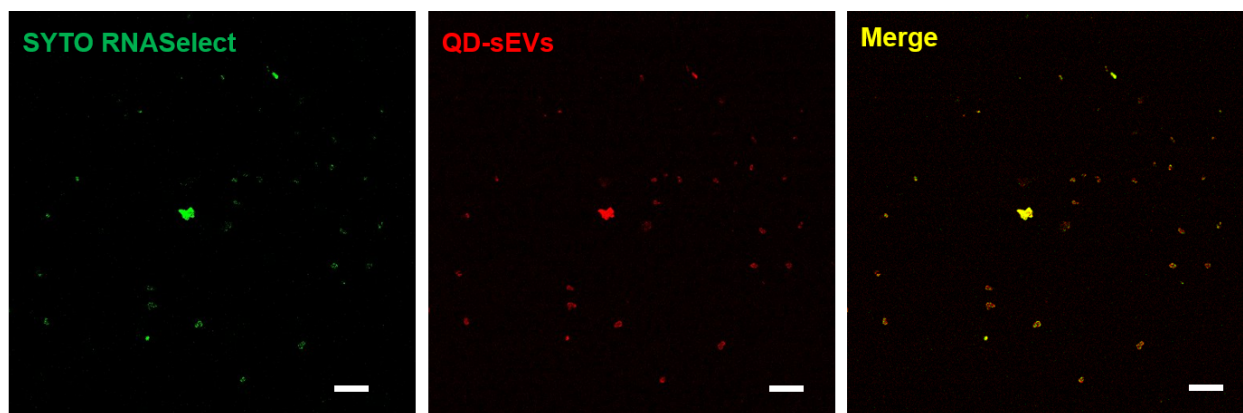


Figure B1. Fluorescence imaging of QD colocalization with sEVs after QD-sEV conjugation.

Representative images taken by confocal microscope at 10x of SYTO RNASelect stained sEVs (green, left), fluorescence signals of QDs in QD-sEVs (red, middle) and merged images of both fluorescence (yellow, right). Scale bar: 100 μm .

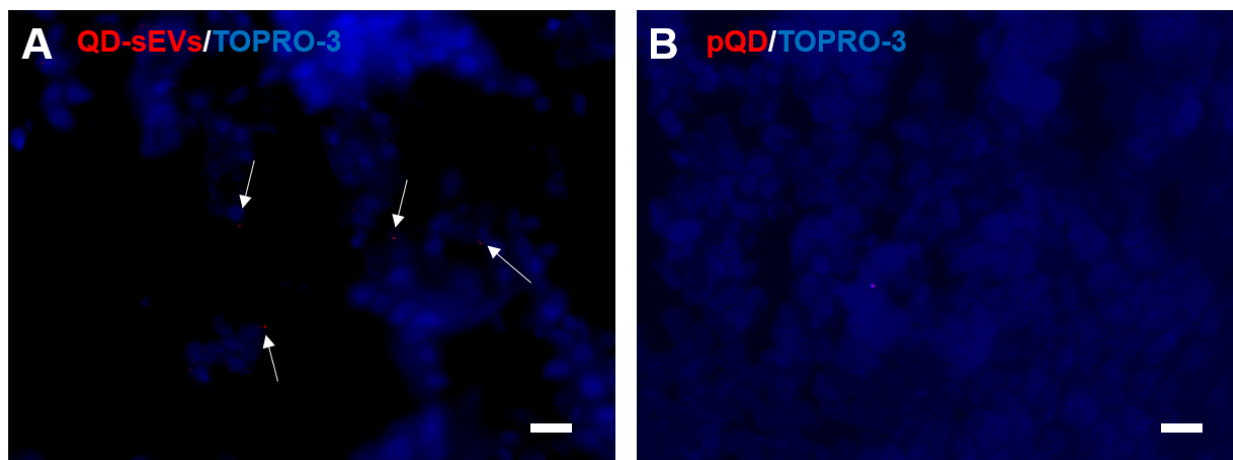


Figure B2. Imaging of QD-sEV conjugates on human vaginal tissue.

After topical application to human vaginal tissue epithelial sheets, incubation and washing, (A) QD-sEV conjugates (red) were distributed across the vaginal epithelium and had punctated signal while (B) pQDs (negative control) showed less distinctive and distributed signal. Cell nuclei were stained with TOPRO-3 (blue). Scale bar: 10 μm . Images provided courtesy of Dr. Lucia Vojtech.

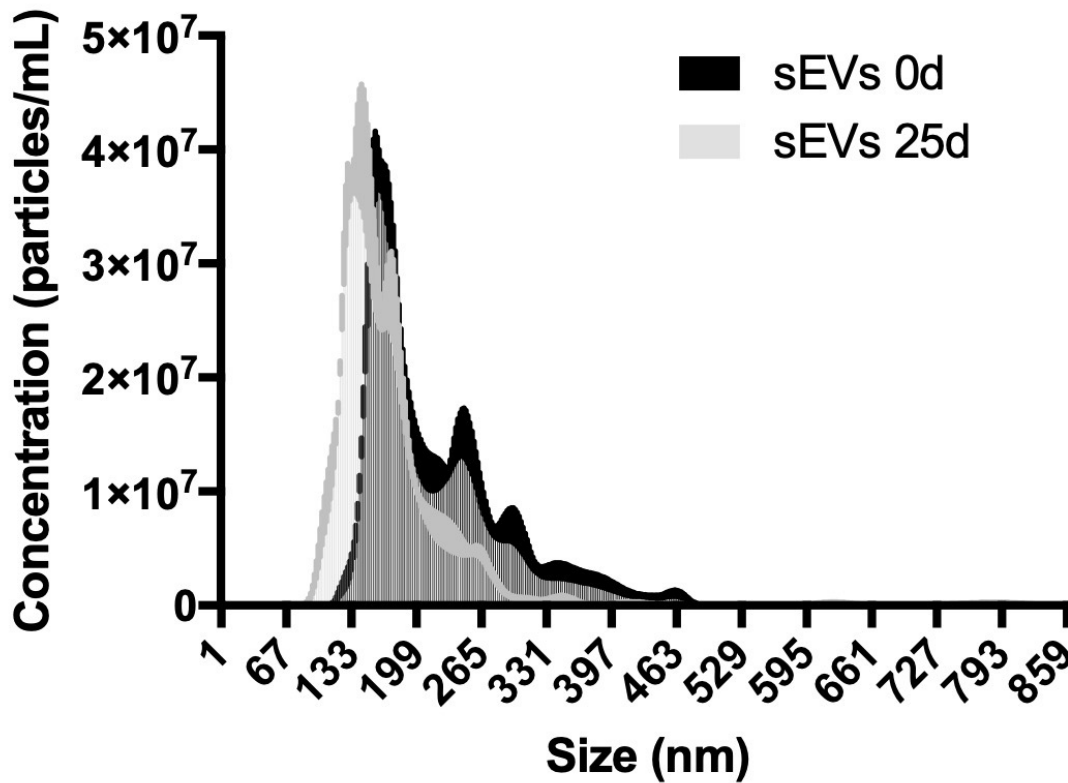


Figure B3. Size distribution of sEVs before and after storing at 4°C for 25 d.

NanoSight measurement was done in triplicate and the data was displayed using the mean value and SEM. The concentration of sEVs at 0 d of storage and 25 d of storage was 7×10^{12} particles/mL and 6.75×10^{12} particles/mL, respectively. The average size of sEVs at 0 d of storage and 25 d of storage was 213.1 nm and 171.1 nm, respectively.

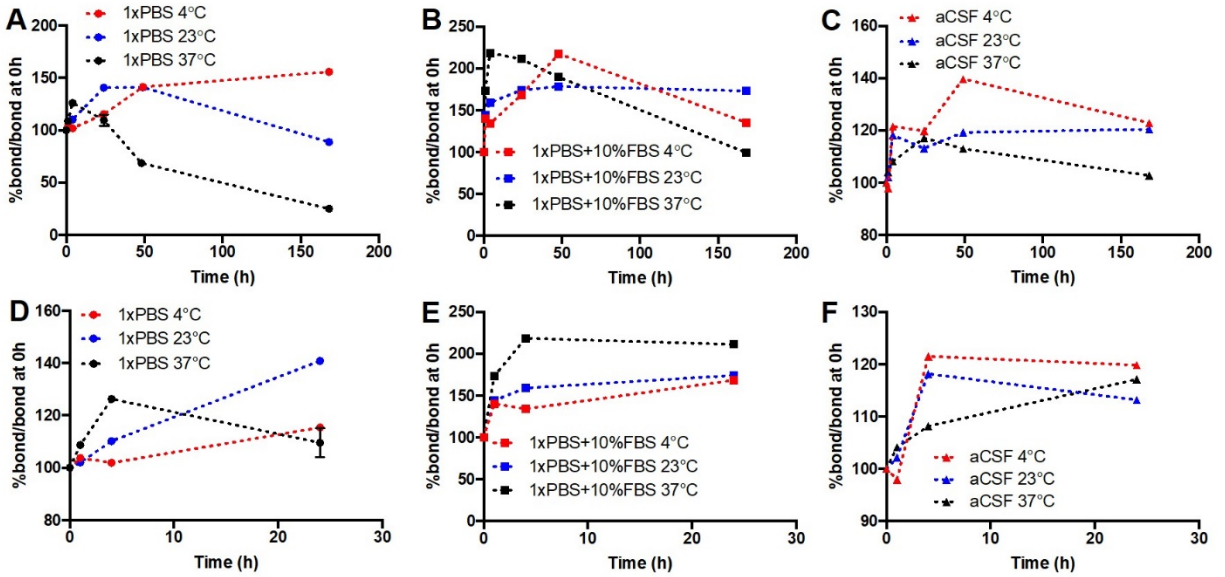


Figure B4. 4FB-HyNic bond stability in biological and storage conditions.

%bond/bond at 0 h as an indicator of 4FB-HyNic bond stability over 1 week in 1xPBS (A), 1xPBS+10%FBS (B), and aCSF (C) at 4°C (red), 23°C (blue) and 37°C (black). %bond/bond at 0 h as an indicator of 4FB-HyNic bond stability over 24 h in 1xPBS (D), 1xPBS+10%FBS (E), and aCSF (F) at 4°C (red), 23°C (blue) and 37°C (black). All analyses were done in triplicate. Error was minimal, and error bars are presented as mean \pm SEM.

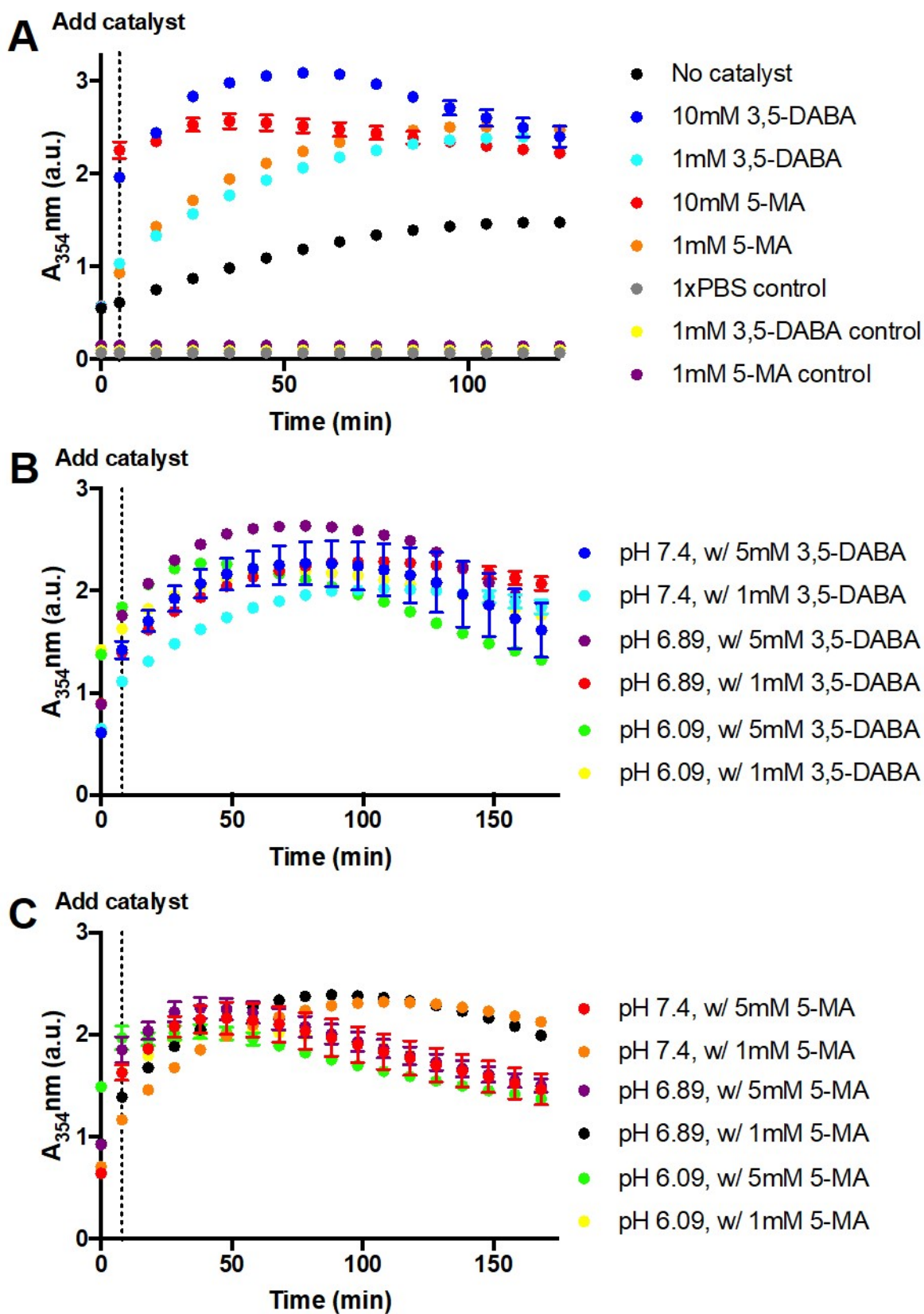


Figure B5. Catalysts accelerate HyNic-4FB bond formation.

Dashed vertical lines represent the time of catalyst addition to the reaction tube. (A) Absorbance intensity at 354 nm of 4FB-HyNic bond with 10 mM 3,5-DABA (blue), 1 mM 3,5-DABA (cyan), 10 mM 5-MA (red), and 1 mM 5-MA (orange) every 10 min during 2 h. The intensity represents the quantity of formed bond. The absorbance of 1xPBS (gray), 3,5-DABA (yellow), and 5-MA (purple) at 354 nm is negligible. (B) Absorbance intensity at 354 nm of 4FB-HyNic bond with 1 mM and 5 mM 5-MA at different pH every 10 min during 2 h. The intensity represents the quantity of formed bond. (C) Absorbance intensity at 354 nm of 4FB-HyNic bond with 1 mM and 5 mM 3,5-DABA at different pH every 10 min during 2 h. The intensity represents the quantity of formed bond. All analyses were done in triplicate, and error bars are presented as mean \pm SEM.

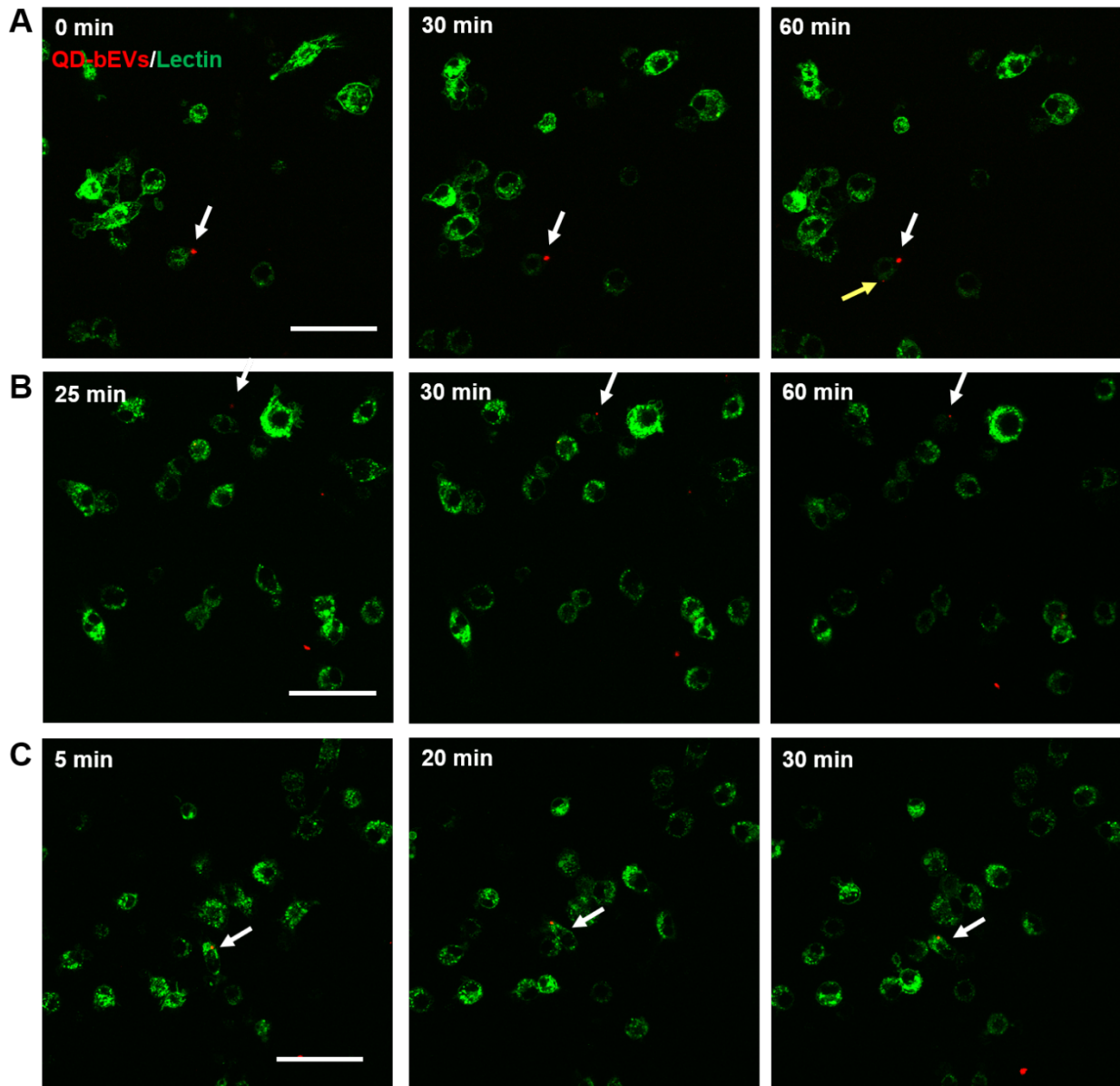


Figure B6. Representative frames of time-lapse imaging of QD-bEVs on BV-2 cells.

(A) Representative frames of Movie B1: Time-lapse imaging of QD-bEVs (red) interacting with Lectin stained BV-2 cells (green) after 1-hour incubation. The QD-bEVs indicated by a white arrow show there was already bEV association with BV-2 cells at the start of 1-hour incubation. The yellow arrow indicates new QD-bEV association with a BV-2 cell surface during the imaging window. The time-lapse images were taken every 5 min for 1 h. Selected frames are at 0 min, 30 min, and 60 min of the imaging window. Scale bar: 50 μm . (B) Representative frames of Movie B2: Time-lapse imaging of QD-bEVs (red) moving and interacting with Lectin stained BV-2 cells (green) after 4-hour incubation. The QD-bEVs indicated by a white arrow moved to a

BV-2 cell, associated with the cell surface and then stayed associated with the cell during the imaging window. The time-lapse images were taken every 5 min for 1 h. Selected frames are at 25 min, 30 min, and 60 min of the imaging window. Scale bar: 50 μm . (C) Representative frame of Movie B3: Time-lapse imaging of QD-bEVs (red) interaction with BV-2 cells (green) after 4-hour incubation. The cell (indicated by a white arrow) continued to migrate during the imaging window even with QD-bEVs associated with its cell membrane. The time-lapse images were taken every 5 min for 1 h. Selected frames are at 5 min, 20 min, and 30 min of the imaging window. Scale bar: 50 μm .

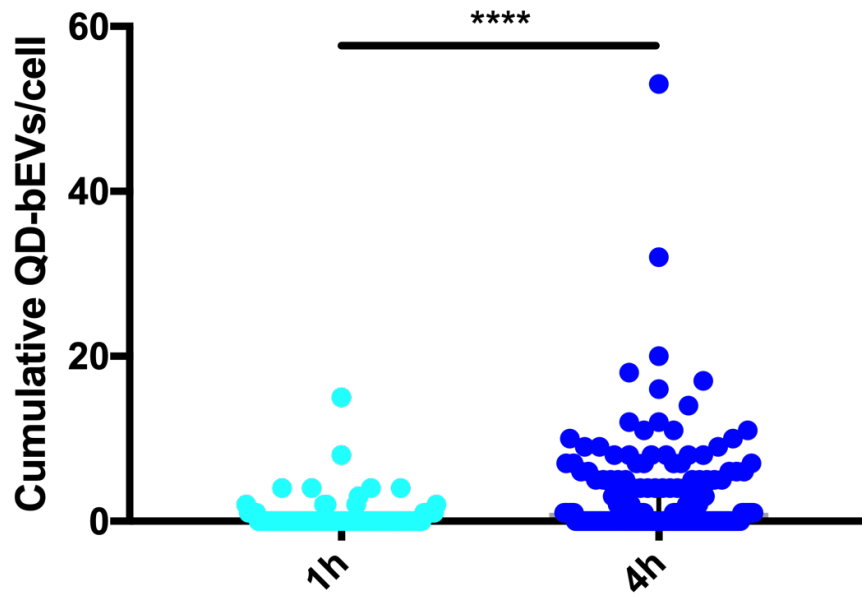


Figure B7. Cumulative counts of the bEV-cell interaction.

Cumulative counts of the bEV-cell interaction per cell during 1-hour time-lapse imaging at 1 h of incubation (n=88 cells in 5 videos, cyan) and 4 h of incubation (n=209 cells in 8 videos, blue). Images were acquired every 5 min for 1 h.

Movie B1.

Time-lapse imaging of QD-bEVs (red) interaction with Lectin stained BV-2 cells (green) after 1-h incubation; the images were taken every 5 min for 1 h.

Movie B2.

Time-lapse imaging of QD-bEVs (red) moving and interacting with Lectin stained BV-2 cells (green) after 4-h incubation; the images were taken every 5 min for 1 h.

Movie B3.

Time-lapse imaging of QD-bEVs (red) interaction with Lectin stained BV-2 cells (green) after 4-h incubation; the images were taken every 5 min for 1 h.

To access the movies, see DOI [10.1021/acsanm.0c01553](https://doi.org/10.1021/acsanm.0c01553).

.

APPENDIX C: Supplementary Figure to Chapter 5

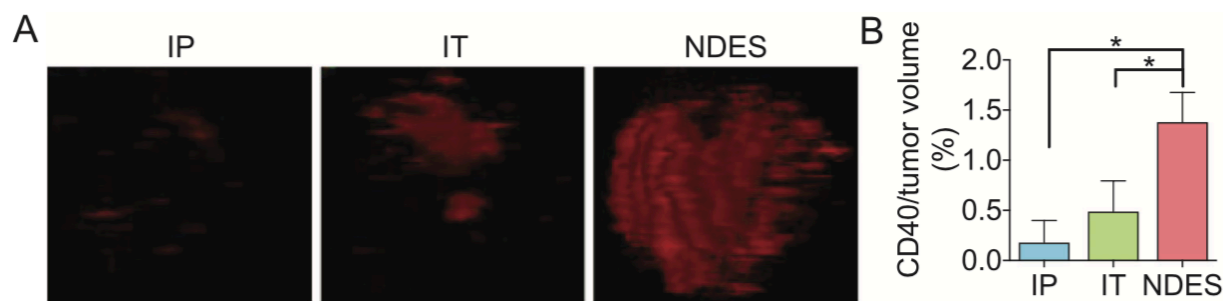


Figure C1. Visualization and quantification of AF700-CD40 distribution in the tumor via immunofluorescence imaging.

A) Reconstructed confocal images of the tumor. Frozen tumor sections were cut into 30 μm slices using a cryostat (Leica Biosystems) with 230 μm between two adjacent slices. Every third slice was imaged *via* a Nikon confocal microscope and 3D reconstructed. The images were stacked through ImageJ and then aligned using the StackReg plugin (ImageJ). A 3D-rendered video was generated using the 3D Viewer Plugin (ImageJ) and representative view of reconstructed images of tumors were taken. B) Percentage AF700-CD40 per tumor volume in intraperitoneal (IP), intratumoral (IT), and NDES group. For each tumor, every third slice was imaged *via* a Nikon confocal microscope for calculation using methodology adapted from previous publication.¹⁵² To minimize noise from tissue autofluorescence, a minimal signal level just below threshold for fluorescent Ab was determined by blank tumor without AF700-CD40. Area of tumor determined by DAPI signals and area of AF700-CD40 were measured by ImageJ macro. Volume of tumor or CD40 was then calculated by multiplying by the distance between images. If the chosen slice was missing or damaged, the adjacent slice was chosen for calculation and the different distance between slices was taken in consideration for calculation. Each data point represents mean \pm standard deviation (STD) ($n = 3$). Statistical significance was determined *via* one-way ANOVA with Tukey test for multiple comparisons. * $p < 0.05$.

Graphs were generated by Alessandro Lab. The data and figures above were published on *Advanced Therapeutic*.

BIBLIOGRAPHY

1. Group, G. B. D. N. D. C., Global, Regional, and National Burden of Neurological Disorders During 1990-2015: A Systematic Analysis for the Global Burden of Disease Study 2015. *Lancet Neurol* **2017**, *16* (11), 877-897.
2. Gooch, C. L.; Pracht, E.; Borenstein, A. R., The Burden of Neurological Disease in the United States: A Summary Report and Call to Action. *Ann Neurol* **2017**, *81* (4), 479-484.
3. Alavijeh, M. S.; Chishty, M.; Qaiser, M. Z.; Palmer, A. M., Drug Metabolism and Pharmacokinetics, the Blood-Brain Barrier, and Central Nervous System Drug Discovery. *NeuroRx* **2005**, *2* (4), 554-71.
4. van Rooy, I.; Cakir-Tascioglu, S.; Hennink, W. E.; Storm, G.; Schiffelers, R. M.; Mastrobattista, E., In Vivo Methods to Study Uptake of Nanoparticles into the Brain. *Pharm Res* **2011**, *28* (3), 456-71.
5. Curtis, C.; Zhang, M.; Liao, R.; Wood, T.; Nance, E., Systems-Level Thinking for Nanoparticle-Mediated Therapeutic Delivery to Neurological Diseases. *Wiley Interdiscip Rev Nanomed Nanobiotechnol* **2017**, *9* (2).
6. Koo, O. M.; Rubinstein, I.; Onyuksel, H., Role of Nanotechnology in Targeted Drug Delivery and Imaging: A Concise Review. *Nanomedicine* **2005**, *1* (3), 193-212.
7. Cormode, D. P.; Skajaa, T.; Fayad, Z. A.; Mulder, W. J., Nanotechnology in Medical Imaging: Probe Design and Applications. *Arterioscler Thromb Vasc Biol* **2009**, *29* (7), 992-1000.
8. Chapman, S.; Dobrovolskaia, M.; Farahani, K.; Goodwin, A.; Joshi, A.; Lee, H.; Meade, T.; Pomper, M.; Ptak, K.; Rao, J.; Singh, R.; Sridhar, S.; Stern, S.; Wang, A.; Weaver, J. B.; Woloschak, G.; Yang, L., Nanoparticles for Cancer Imaging: The Good, the Bad, and the Promise. *Nano Today* **2013**, *8* (5), 454-460.
9. Bogart, L. K.; Pourroy, G.; Murphy, C. J.; Puentes, V.; Pellegrino, T.; Rosenblum, D.; Peer, D.; Levy, R., Nanoparticles for Imaging, Sensing, and Therapeutic Intervention. *ACS Nano* **2014**, *8* (4), 3107-22.
10. Neuwelt, A.; Sidhu, N.; Hu, C. A.; Mlady, G.; Eberhardt, S. C.; Sillerud, L. O., Iron-Based Superparamagnetic Nanoparticle Contrast Agents for Mri of Infection and Inflammation. *AJR Am J Roentgenol* **2015**, *204* (3), W302-13.
11. Xing, Y.; Rao, J., Quantum Dot Bioconjugates for in Vitro Diagnostics & in Vivo Imaging. *Cancer Biomark* **2008**, *4* (6), 307-19.
12. Medintz, I. L.; Uyeda, H. T.; Goldman, E. R.; Mattoussi, H., Quantum Dot Bioconjugates for Imaging, Labelling and Sensing. *Nat Mater* **2005**, *4* (6), 435-46.
13. Michalet, X.; Pinaud, F. F.; Bentolila, L. A.; Tsay, J. M.; Doose, S.; Li, J. J.; Sundaresan, G.; Wu, A. M.; Gambhir, S. S.; Weiss, S., Quantum Dots for Live Cells, in Vivo Imaging, and Diagnostics. *Science* **2005**, *307* (5709), 538-44.
14. Chen, O.; Zhao, J.; Chauhan, V. P.; Cui, J.; Wong, C.; Harris, D. K.; Wei, H.; Han, H. S.; Fukumura, D.; Jain, R. K.; Bawendi, M. G., Compact High-Quality Cdse-Cds Core-Shell Nanocrystals with Narrow Emission Linewidths and Suppressed Blinking. *Nat Mater* **2013**, *12* (5), 445-51.
15. Zhou, J.; Zhu, M.; Meng, R.; Qin, H.; Peng, X., Ideal Cdse/Cds Core/Shell Nanocrystals Enabled by Entropic Ligands and Their Core Size-, Shell Thickness-, and Ligand-Dependent Photoluminescence Properties. *J Am Chem Soc* **2017**, *139* (46), 16556-16567.
16. Kobayashi, H.; Hama, Y.; Koyama, Y.; Barrett, T.; Regino, C. A.; Urano, Y.; Choyke, P. L., Simultaneous Multicolor Imaging of Five Different Lymphatic Basins Using Quantum Dots. *Nano Lett* **2007**, *7* (6), 1711-6.

17. Jaiswal, J. K.; Mattoussi, H.; Mauro, J. M.; Simon, S. M., Long-Term Multiple Color Imaging of Live Cells Using Quantum Dot Bioconjugates. *Nat Biotechnol* **2003**, *21* (1), 47-51.
18. Walters, R.; Medintz, I. L.; Delehanty, J. B.; Stewart, M. H.; Susumu, K.; Huston, A. L.; Dawson, P. E.; Dawson, G., The Role of Negative Charge in the Delivery of Quantum Dots to Neurons. *ASN Neuro* **2015**, *7* (4).
19. Dante, S.; Petrelli, A.; Petrini, E. M.; Marotta, R.; Maccione, A.; Alabastri, A.; Quarta, A.; De Donato, F.; Ravasenga, T.; Sathya, A.; Cingolani, R.; Proietti Zaccaria, R.; Berdondini, L.; Barberis, A.; Pellegrino, T., Selective Targeting of Neurons with Inorganic Nanoparticles: Revealing the Crucial Role of Nanoparticle Surface Charge. *ACS Nano* **2017**, *11* (7), 6630-6640.
20. Minami, S. S.; Sun, B.; Popat, K.; Kauppinen, T.; Pleiss, M.; Zhou, Y.; Ward, M. E.; Floreancig, P.; Mucke, L.; Desai, T.; Gan, L., Selective Targeting of Microglia by Quantum Dots. *J Neuroinflammation* **2012**, *9*, 22.
21. Thorne, R. G.; Nicholson, C., In Vivo Diffusion Analysis with Quantum Dots and Dextran Predicts the Width of Brain Extracellular Space. *Proc Natl Acad Sci U S A* **2006**, *103* (14), 5567-72.
22. Marshall, J. D.; Schnitzer, M. J., Optical Strategies for Sensing Neuronal Voltage Using Quantum Dots and Other Semiconductor Nanocrystals. *ACS Nano* **2013**, *7* (5), 4601-9.
23. Xu, G.; Mahajan, S.; Roy, I.; Yong, K. T., Theranostic Quantum Dots for Crossing Blood-Brain Barrier in Vitro and Providing Therapy of Hiv-Associated Encephalopathy. *Front Pharmacol* **2013**, *4*, 140.
24. Zhang, Q., Imaging Single Synaptic Vesicles in Mammalian Central Synapses with Quantum Dots. *Methods Mol Biol* **2013**, *1026*, 57-69.
25. Dawson, G., Quantum Dots and Potential Therapy for Krabbe's Disease. *J Neurosci Res* **2016**, *94* (11), 1293-303.
26. Efros, A. L.; Delehanty, J. B.; Huston, A. L.; Medintz, I. L.; Barbic, M.; Harris, T. D., Evaluating the Potential of Using Quantum Dots for Monitoring Electrical Signals in Neurons. *Nat Nanotechnol* **2018**, *13* (4), 278-288.
27. Choi, C.; Colon-Berrios, A. R.; Hamachi, L. S.; Owen, J. S.; Schwartz, T. H.; Ma, H. T.; Kymissis, I., Localizing Seizure Activity in the Brain Using Implantable Micro-Leds with Quantum Dot Downconversion. *Adv Mater Technol-Us* **2018**, *3* (6).
28. Pathak, S.; Cao, E.; Davidson, M. C.; Jin, S.; Silva, G. A., Quantum Dot Applications to Neuroscience: New Tools for Probing Neurons and Glia. *J Neurosci* **2006**, *26* (7), 1893-5.
29. Yaghini, E.; Turner, H.; Pilling, A.; Naasani, I.; MacRobert, A., In Vivo Biodistribution and Toxicology Studies of Cadmium-Free Indium-Based Quantum Dot Nanoparticles in a Rat Model. *Nanomedicine* **2018**.
30. Varela, J. A.; Dupuis, J. P.; Etchepare, L.; Espana, A.; Cognet, L.; Groc, L., Targeting Neurotransmitter Receptors with Nanoparticles in Vivo Allows Single-Molecule Tracking in Acute Brain Slices. *Nat Commun* **2016**, *7*, 10947.
31. Chang, J. C.; Kovtun, O.; Blakely, R. D.; Rosenthal, S. J., Labeling of Neuronal Receptors and Transporters with Quantum Dots. *Wiley Interdiscip Rev Nanomed Nanobiotechnol* **2012**, *4* (6), 605-19.
32. Agarwal, R.; Domowicz, M. S.; Schwartz, N. B.; Henry, J.; Medintz, I.; Delehanty, J. B.; Stewart, M. H.; Susumu, K.; Huston, A. L.; Deschamps, J. R.; Dawson, P. E.; Palomo, V.; Dawson, G., Delivery and Tracking of Quantum Dot Peptide Bioconjugates in an Intact Developing Avian Brain. *ACS Chem. Neurosci.* **2015**, *6* (3), 494-504.

33. Wang, J.; Yong, W. H.; Sun, Y.; Vernier, P. T.; Koeffler, H. P.; Gundersen, M. A.; Marcu, L., Receptor-Targeted Quantum Dots: Fluorescent Probes for Brain Tumor Diagnosis. *J. Biomed. Opt.* **2007**, *12* (4), 044021.
34. Hong, Z. Y.; Lv, C.; Liu, A. A.; Liu, S. L.; Sun, E. Z.; Zhang, Z. L.; Lei, A. W.; Pang, D. W., Clicking Hydrazine and Aldehyde: The Way to Labeling of Viruses with Quantum Dots. *ACS Nano* **2015**, *9* (12), 11750-60.
35. Joo, K. I.; Fang, Y.; Liu, Y.; Xiao, L.; Gu, Z.; Tai, A.; Lee, C. L.; Tang, Y.; Wang, P., Enhanced Real-Time Monitoring of Adeno-Associated Virus Trafficking by Virus-Quantum Dot Conjugates. *ACS Nano* **2011**, *5* (5), 3523-35.
36. Raposo, G.; Stoorvogel, W., Extracellular Vesicles: Exosomes, Microvesicles, and Friends. *J Cell Biol* **2013**, *200* (4), 373-83.
37. Tkach, M.; Thery, C., Communication by Extracellular Vesicles: Where We Are and Where We Need to Go. *Cell* **2016**, *164* (6), 1226-1232.
38. Hristov, M.; Erl, W.; Linder, S.; Weber, P. C., Apoptotic Bodies from Endothelial Cells Enhance the Number and Initiate the Differentiation of Human Endothelial Progenitor Cells in Vitro. *Blood* **2004**, *104* (9), 2761-6.
39. Kim, K. M.; Abdelmohsen, K.; Mustapic, M.; Kapogiannis, D.; Gorospe, M., Rna in Extracellular Vesicles. *Wiley Interdiscip Rev RNA* **2017**, *8* (4).
40. Camussi, G.; Deregibus, M. C.; Tetta, C., Paracrine/Endocrine Mechanism of Stem Cells on Kidney Repair: Role of Microvesicle-Mediated Transfer of Genetic Information. *Curr Opin Nephrol Hypertens* **2010**, *19* (1), 7-12.
41. Grange, C.; Tapparo, M.; Bruno, S.; Chatterjee, D.; Quesenberry, P. J.; Tetta, C.; Camussi, G., Biodistribution of Mesenchymal Stem Cell-Derived Extracellular Vesicles in a Model of Acute Kidney Injury Monitored by Optical Imaging. *Int J Mol Med* **2014**, *33* (5), 1055-63.
42. Shenoda, B. B.; Ajit, S. K., Modulation of Immune Responses by Exosomes Derived from Antigen-Presenting Cells. *Clin Med Insights Pathol* **2016**, *9* (Suppl 1), 1-8.
43. Aswad, H.; Forterre, A.; Wiklander, O. P.; Vial, G.; Danty-Berger, E.; Jalabert, A.; Lamaziere, A.; Meugnier, E.; Pesenti, S.; Ott, C.; Chikh, K.; El-Andaloussi, S.; Vidal, H.; Lefai, E.; Rieusset, J.; Rome, S., Exosomes Participate in the Alteration of Muscle Homeostasis During Lipid-Induced Insulin Resistance in Mice. *Diabetologia* **2014**, *57* (10), 2155-64.
44. Croese, T.; Furlan, R., Extracellular Vesicles in Neurodegenerative Diseases. *Mol Aspects Med* **2018**, *60*, 52-61.
45. Karthikeyan, A.; Patnala, R.; Jadhav, S. P.; Eng-Ang, L.; Dheen, S. T., Micrnas: Key Players in Microglia and Astrocyte Mediated Inflammation in Cns Pathologies. *Curr Med Chem* **2016**, *23* (30), 3528-3546.
46. Trotta, T.; Panaro, M. A.; Cianciulli, A.; Mori, G.; Di Benedetto, A.; Porro, C., Microglia-Derived Extracellular Vesicles in Alzheimer's Disease: A Double-Edged Sword. *Biochem Pharmacol* **2018**, *148*, 184-192.
47. Manek, R.; Moghieb, A.; Yang, Z.; Kumar, D.; Kobessiy, F.; Sarkis, G. A.; Raghavan, V.; Wang, K. K. W., Protein Biomarkers and Neuroproteomics Characterization of Microvesicles/Exosomes from Human Cerebrospinal Fluid Following Traumatic Brain Injury. *Mol Neurobiol* **2018**, *55* (7), 6112-6128.
48. Brites, D.; Fernandes, A., Neuroinflammation and Depression: Microglia Activation, Extracellular Microvesicles and Microrna Dysregulation. *Front Cell Neurosci* **2015**, *9*, 476.

49. Chen, Y. F.; Tang, Y. L.; Fan, G. C.; Duan, D. D., Extracellular Vesicles as Novel Biomarkers and Pharmaceutical Targets of Diseases. *Acta Pharmacol Sin* **2018**, *39* (4), 499-500.
50. Vader, P.; Breakefield, X. O.; Wood, M. J., Extracellular Vesicles: Emerging Targets for Cancer Therapy. *Trends Mol Med* **2014**, *20* (7), 385-93.
51. Doeppner, T. R.; Herz, J.; Gorgens, A.; Schlechter, J.; Ludwig, A. K.; Radtke, S.; de Miroschedji, K.; Horn, P. A.; Giebel, B.; Hermann, D. M., Extracellular Vesicles Improve Post-Stroke Neuroregeneration and Prevent Postischemic Immunosuppression. *Stem Cells Transl Med* **2015**, *4* (10), 1131-43.
52. van der Meel, R.; Fens, M. H.; Vader, P.; van Solinge, W. W.; Eniola-Adefeso, O.; Schiffelers, R. M., Extracellular Vesicles as Drug Delivery Systems: Lessons from the Liposome Field. *J Control Release* **2014**, *195*, 72-85.
53. Yu, W. W.; Qu, L.; Guo, W.; Peng, X., Experimental Determination of the Extinction Coefficient of Cdte, Cdse, and Cds Nanocrystals. *Chem. Mater.* **2003**, *15* (14), 2854-2860.
54. Monguzzi, A.; Braga, D.; Gandini, M.; Holmberg, V. C.; Kim, D. K.; Sahu, A.; Norris, D. J.; Meinardi, F., Broadband up-Conversion at Subsolar Irradiance: Triplet-Triplet Annihilation Boosted by Fluorescent Semiconductor Nanocrystals. *Nano Lett.* **2014**, *14* (11), 6644-50.
55. Zhang, H.; Cheng, K.; Hou, Y. M.; Fang, Z.; Pan, Z. X.; Wu, W. J.; Hua, J. L.; Zhong, X. H., Efficient Cdse Quantum Dot-Sensitized Solar Cells Prepared by a Postsynthesis Assembly Approach. *Chem. Commun. (Camb.)* **2012**, *48* (91), 11235-7.
56. Zhang, F.; Nance, E.; Alnasser, Y.; Kannan, R.; Kannan, S., Microglial Migration and Interactions with Dendrimer Nanoparticles Are Altered in the Presence of Neuroinflammation. *J Neuroinflammation* **2016**, *13* (1), 65.
57. Calvo, P.; Gouritin, B.; Chacun, H.; Desmaele, D.; D'Angelo, J.; Noel, J. P.; Georgin, D.; Fattal, E.; Andreux, J. P.; Couvreur, P., Long-Circulating Pegylated Polycyanoacrylate Nanoparticles as New Drug Carrier for Brain Delivery. *Pharm Res* **2001**, *18* (8), 1157-66.
58. Perez-Campana, C.; Gomez-Vallejo, V.; Puigivila, M.; Martin, A.; Calvo-Fernandez, T.; Moya, S. E.; Ziolo, R. F.; Reese, T.; Llop, J., Biodistribution of Different Sized Nanoparticles Assessed by Positron Emission Tomography: A General Strategy for Direct Activation of Metal Oxide Particles. *ACS Nano* **2013**, *7* (4), 3498-505.
59. Kulkarni, S. A.; Feng, S. S., Effects of Particle Size and Surface Modification on Cellular Uptake and Biodistribution of Polymeric Nanoparticles for Drug Delivery. *Pharm Res* **2013**, *30* (10), 2512-22.
60. Curtis, C.; Toghiani, D.; Wong, B.; Nance, E., Colloidal Stability as a Determinant of Nanoparticle Behavior in the Brain. *Colloids Surf B Biointerfaces* **2018**, *170*, 673-682.
61. Bustin, S. A.; Benes, V.; Garson, J. A.; Hellemans, J.; Huggett, J.; Kubista, M.; Mueller, R.; Nolan, T.; Pfaffl, M. W.; Shipley, G. L.; Vandesompele, J.; Wittwer, C. T., The Miqe Guidelines: Minimum Information for Publication of Quantitative Real-Time Pcr Experiments. *Clin Chem* **2009**, *55* (4), 611-22.
62. Vojtech, L.; Woo, S.; Hughes, S.; Levy, C.; Ballweber, L.; Sauteraud, R. P.; Strobl, J.; Westerberg, K.; Gottardo, R.; Tewari, M.; Hladik, F., Exosomes in Human Semen Carry a Distinctive Repertoire of Small Non-Coding Rnas with Potential Regulatory Functions. *Nucleic Acids Res* **2014**, *42* (11), 7290-304.
63. Vella, L. J.; Scicluna, B. J.; Cheng, L.; Bawden, E. G.; Masters, C. L.; Ang, C. S.; Williamson, N.; McLean, C.; Barnham, K. J.; Hill, A. F., A Rigorous Method to Enrich for Exosomes from Brain Tissue. *J Extracell Vesicles* **2017**, *6* (1), 1348885.

64. Webber, J.; Clayton, A., How Pure Are Your Vesicles? *J Extracell Vesicles* **2013**, *2*.
65. They, C.; Amigorena, S.; Raposo, G.; Clayton, A., Isolation and Characterization of Exosomes from Cell Culture Supernatants and Biological Fluids. *Curr Protoc Cell Biol* **2006**, Chapter 3, Unit 3 22.
66. Crisalli, P.; Kool, E. T., Water-Soluble Organocatalysts for Hydrazone and Oxime Formation. *J Org Chem* **2013**, *78* (3), 1184-9.
67. Gobe, G.; Crane, D., Mitochondria, Reactive Oxygen Species and Cadmium Toxicity in the Kidney. *Toxicol Lett* **2010**, *198* (1), 49-55.
68. Adisheshaiah, P. P.; Hall, J. B.; McNeil, S. E., Nanomaterial Standards for Efficacy and Toxicity Assessment. *Wiley Interdiscip Rev Nanomed Nanobiotechnol* **2010**, *2* (1), 99-112.
69. Rehberg, M.; Praetner, M.; Leite, C. F.; Reichel, C. A.; Bihari, P.; Mildner, K.; Duhr, S.; Zeuschner, D.; Krombach, F., Quantum Dots Modulate Leukocyte Adhesion and Transmigration Depending on Their Surface Modification. *Nano Lett* **2010**, *10* (9), 3656-64.
70. Hoshino, A.; Fujioka, K.; Oku, T.; Suga, M.; Sasaki, Y. F.; Ohta, T.; Yasuhara, M.; Suzuki, K.; Yamamoto, K., Physicochemical Properties and Cellular Toxicity of Nanocrystal Quantum Dots Depend on Their Surface Modification. *Nano Letters* **2004**, *4* (11), 2163-2169.
71. Tang, Y.; Han, S.; Liu, H.; Chen, X.; Huang, L.; Li, X.; Zhang, J., The Role of Surface Chemistry in Determining in Vivo Biodistribution and Toxicity of Cdse/Zns Core-Shell Quantum Dots. *Biomaterials* **2013**, *34* (34), 8741-55.
72. Zhang, Y.; Pan, H.; Zhang, P.; Gao, N.; Lin, Y.; Luo, Z.; Li, P.; Wang, C.; Liu, L.; Pang, D.; Cai, L.; Ma, Y., Functionalized Quantum Dots Induce Proinflammatory Responses in Vitro: The Role of Terminal Functional Group-Associated Endocytic Pathways. *Nanoscale* **2013**, *5* (13), 5919-29.
73. Blanco, E.; Shen, H.; Ferrari, M., Principles of Nanoparticle Design for Overcoming Biological Barriers to Drug Delivery. *Nat Biotechnol* **2015**, *33* (9), 941-51.
74. Kress, S. J.; Antolinez, F. V.; Richner, P.; Jayanti, S. V.; Kim, D. K.; Prins, F.; Riedinger, A.; Fischer, M. P.; Meyer, S.; McPeak, K. M.; Poulikakos, D.; Norris, D. J., Wedge Waveguides and Resonators for Quantum Plasmonics. *Nano Lett* **2015**, *15* (9), 6267-75.
75. Wu, X.; Liu, H.; Liu, J.; Haley, K. N.; Treadway, J. A.; Larson, J. P.; Ge, N.; Peale, F.; Bruchez, M. P., Immunofluorescent Labeling of Cancer Marker Her2 and Other Cellular Targets with Semiconductor Quantum Dots. *Nat Biotechnol* **2003**, *21* (1), 41-6.
76. Nance, E. A.; Woodworth, G. F.; Sailor, K. A.; Shih, T. Y.; Xu, Q.; Swaminathan, G.; Xiang, D.; Eberhart, C.; Hanes, J., A Dense Poly(Ethylene Glycol) Coating Improves Penetration of Large Polymeric Nanoparticles within Brain Tissue. *Sci Transl Med* **2012**, *4* (149), 149ra119.
77. Holmberg, V. C.; Rasch, M. R.; Korgel, B. A., Pegylation of Carboxylic Acid-Functionalized Germanium Nanowires. *Langmuir* **2010**, *26* (17), 14241-6.
78. Hiroatsu, M.; Tatsuo, M., Intrachain Force Field and Normal Vibrations of Polyethylene Glycol. *Bulletin of the Chemical Society of Japan* **1968**, *41* (8), 1798-1808.
79. Matsuura, H.; Miyazawa, T., Frequency Distribution and Neutron Scattering of Polyethylene Glycol Chain. *The Journal of Chemical Physics* **1969**, *50* (2), 915-919.
80. Interpretation of Infrared Spectra, a Practical Approach. In *Encyclopedia of Analytical Chemistry*.
81. Oomens, J.; Steill, J. D., Free Carboxylate Stretching Modes. *J Phys Chem A* **2008**, *112* (15), 3281-3.
82. Gareri, P.; Mattace, R.; Nava, F.; De Sarro, G., Role of Calcium in Brain Aging. *Gen Pharmacol* **1995**, *26* (8), 1651-7.

83. Guzman, J. N.; Sanchez-Padilla, J.; Wokosin, D.; Kondapalli, J.; Ilijic, E.; Schumacker, P. T.; Surmeier, D. J., Oxidant Stress Evoked by Pacemaking in Dopaminergic Neurons Is Attenuated by Dj-1. *Nature* **2010**, *468* (7324), 696-700.
84. Smith, A. M.; Duan, H.; Rhyner, M. N.; Ruan, G.; Nie, S., A Systematic Examination of Surface Coatings on the Optical and Chemical Properties of Semiconductor Quantum Dots. *Phys Chem Chem Phys* **2006**, *8* (33), 3895-903.
85. Ling, E. A.; Wong, W. C., The Origin and Nature of Ramified and Amoeboid Microglia: A Historical Review and Current Concepts. *Glia* **1993**, *7* (1), 9-18.
86. Maysinger, D.; Behrendt, M.; Lalancette-Hebert, M.; Kriz, J., Real-Time Imaging of Astrocyte Response to Quantum Dots: In Vivo Screening Model System for Biocompatibility of Nanoparticles. *Nano Lett* **2007**, *7* (8), 2513-20.
87. Lovric, J.; Bazzi, H. S.; Cuie, Y.; Fortin, G. R.; Winnik, F. M.; Maysinger, D., Differences in Subcellular Distribution and Toxicity of Green and Red Emitting Cdte Quantum Dots. *J Mol Med (Berl)* **2005**, *83* (5), 377-85.
88. Ohkuma, S.; Poole, B., Fluorescence Probe Measurement of the Intralysosomal Ph in Living Cells and the Perturbation of Ph by Various Agents. *Proc Natl Acad Sci U S A* **1978**, *75* (7), 3327-31.
89. Nagy, A.; Zane, A.; Cole, S. L.; Severance, M.; Dutta, P. K.; Waldman, W. J., Contrast of the Biological Activity of Negatively and Positively Charged Microwave Synthesized Cdse/Zns Quantum Dots. *Chem Res Toxicol* **2011**, *24* (12), 2176-88.
90. Humpel, C., Organotypic Brain Slice Cultures: A Review. *Neuroscience* **2015**, *305*, 86-98.
91. Wu, T.; Zhang, T.; Chen, Y.; Tang, M., Research Advances on Potential Neurotoxicity of Quantum Dots. *J Appl Toxicol* **2016**, *36* (3), 345-51.
92. Chen, N.; He, Y.; Su, Y.; Li, X.; Huang, Q.; Wang, H.; Zhang, X.; Tai, R.; Fan, C., The Cytotoxicity of Cadmium-Based Quantum Dots. *Biomaterials* **2012**, *33* (5), 1238-44.
93. Chang, E.; Thekkek, N.; Yu, W. W.; Colvin, V. L.; Drezek, R., Evaluation of Quantum Dot Cytotoxicity Based on Intracellular Uptake. *Small* **2006**, *2* (12), 1412-7.
94. Jevprasesphant, R.; Penny, J.; Jalal, R.; Attwood, D.; McKeown, N. B.; D'Emanuele, A., The Influence of Surface Modification on the Cytotoxicity of Pamam Dendrimers. *Int J Pharm* **2003**, *252* (1-2), 263-6.
95. Kirchner, C.; Liedl, T.; Kudera, S.; Pellegrino, T.; Munoz Javier, A.; Gaub, H. E.; Stolzle, S.; Fertig, N.; Parak, W. J., Cytotoxicity of Colloidal Cdse and Cdse/Zns Nanoparticles. *Nano Lett* **2005**, *5* (2), 331-8.
96. Ho, C. C.; Chang, H.; Tsai, H. T.; Tsai, M. H.; Yang, C. S.; Ling, Y. C.; Lin, P., Quantum Dot 705, a Cadmium-Based Nanoparticle, Induces Persistent Inflammation and Granuloma Formation in the Mouse Lung. *Nanotoxicology* **2013**, *7* (1), 105-15.
97. Tang, S.; Wu, Y.; Ryan, C. N.; Yu, S.; Qin, G.; Edwards, D. S.; Mayer, G. D., Distinct Expression Profiles of Stress Defense and DNA Repair Genes in *Daphnia Pulex* Exposed to Cadmium, Zinc, and Quantum Dots. *Chemosphere* **2015**, *120*, 92-9.
98. Simon, D. F.; Domingos, R. F.; Hauser, C.; Hutchins, C. M.; Zerges, W.; Wilkinson, K. J., Transcriptome Sequencing (Rna-Seq) Analysis of the Effects of Metal Nanoparticle Exposure on the Transcriptome of *Chlamydomonas Reinhardtii*. *Appl Environ Microbiol* **2013**, *79* (16), 4774-85.
99. Nagy, A.; Hollingsworth, J. A.; Hu, B.; Steinbruck, A.; Stark, P. C.; Rios Valdez, C.; Vuyisich, M.; Stewart, M. H.; Atha, D. H.; Nelson, B. C.; Iyer, R., Functionalization-Dependent

- Induction of Cellular Survival Pathways by Cdse Quantum Dots in Primary Normal Human Bronchial Epithelial Cells. *ACS Nano* **2013**, 7 (10), 8397-411.
100. Sharma, S.; Rais, A.; Sandhu, R.; Nel, W.; Ebadi, M., Clinical Significance of Metallothioneins in Cell Therapy and Nanomedicine. *Int J Nanomedicine* **2013**, 8, 1477-88.
101. Thirumoorthy, N.; Shyam Sunder, A.; Manisenthil Kumar, K.; Senthil Kumar, M.; Ganesh, G.; Chatterjee, M., A Review of Metallothionein Isoforms and Their Role in Pathophysiology. *World J Surg Oncol* **2011**, 9, 54.
102. Peynshaert, K.; Soenen, S. J.; Manshian, B. B.; Doak, S. H.; Braeckmans, K.; De Smedt, S. C.; Remaut, K., Coating of Quantum Dots Strongly Defines Their Effect on Lysosomal Health and Autophagy. *Acta Biomater* **2017**, 48, 195-205.
103. Sabolic, I.; Breljak, D.; Skarica, M.; Herak-Kramberger, C. M., Role of Metallothionein in Cadmium Traffic and Toxicity in Kidneys and Other Mammalian Organs. *Biometals* **2010**, 23 (5), 897-926.
104. Artells, E.; Palacios, O.; Capdevila, M.; Atrian, S., Mammalian Mt1 and Mt2 Metallothioneins Differ in Their Metal Binding Abilities. *Metallomics* **2013**, 5 (10), 1397-410.
105. Becher, B.; Spath, S.; Goverman, J., Cytokine Networks in Neuroinflammation. *Nat Rev Immunol* **2017**, 17 (1), 49-59.
106. Su, J. H.; Deng, G.; Cotman, C. W., Bax Protein Expression Is Increased in Alzheimer's Brain: Correlations with DNA Damage, Bcl-2 Expression, and Brain Pathology. *J Neuropathol Exp Neurol* **1997**, 56 (1), 86-93.
107. Yang, X.; Yang, S.; Zhang, J.; Xue, L.; Hu, Z., Role of Caspase 3 in Neuronal Apoptosis after Acute Brain Injury. *Chin J Traumatol* **2002**, 5 (4), 250-3.
108. Sawada, M.; Suzumura, A.; Hosoya, H.; Marunouchi, T.; Nagatsu, T., Interleukin-10 Inhibits Both Production of Cytokines and Expression of Cytokine Receptors in Microglia. *J Neurochem* **1999**, 72 (4), 1466-71.
109. Drouin-Ouellet, J.; Brownell, A. L.; Saint-Pierre, M.; Fasano, C.; Emond, V.; Trudeau, L. E.; Levesque, D.; Cicchetti, F., Neuroinflammation Is Associated with Changes in Glial Mglur5 Expression and the Development of Neonatal Excitotoxic Lesions. *Glia* **2011**, 59 (2), 188-99.
110. Byrnes, K. R.; Stoica, B.; Loane, D. J.; Riccio, A.; Davis, M. I.; Faden, A. I., Metabotropic Glutamate Receptor 5 Activation Inhibits Microglial Associated Inflammation and Neurotoxicity. *Glia* **2009**, 57 (5), 550-560.
111. Carrasquillo, M. M.; Allen, M.; Burgess, J. D.; Wang, X.; Strickland, S. L.; Aryal, S.; Siuda, J.; Kachadoorian, M. L.; Medway, C.; Younkin, C. S.; Nair, A.; Wang, C.; Chanana, P.; Serie, D.; Nguyen, T.; Lincoln, S.; Malphrus, K. G.; Morgan, K.; Golde, T. E.; Price, N. D.; White, C. C.; De Jager, P. L.; Bennett, D. A.; Asmann, Y. W.; Crook, J. E.; Petersen, R. C.; Graff-Radford, N. R.; Dickson, D. W.; Younkin, S. G.; Ertekin-Taner, N., A Candidate Regulatory Variant at the Trem Gene Cluster Associates with Decreased Alzheimer's Disease Risk and Increased Trem11 and Trem2 Brain Gene Expression. *Alzheimers Dement* **2017**, 13 (6), 663-673.
112. Hoshyar, N.; Gray, S.; Han, H.; Bao, G., The Effect of Nanoparticle Size on in Vivo Pharmacokinetics and Cellular Interaction. *Nanomedicine (Lond)* **2016**, 11 (6), 673-92.
113. Kato, S.; Itoh, K.; Yaoi, T.; Tozawa, T.; Yoshikawa, Y.; Yasui, H.; Kanamura, N.; Hoshino, A.; Manabe, N.; Yamamoto, K.; Fushiki, S., Organ Distribution of Quantum Dots after Intraperitoneal Administration, with Special Reference to Area-Specific Distribution in the Brain. *Nanotechnology* **2010**, 21 (33), 335103.

114. Paris-Robidas, S.; Brouard, D.; Emond, V.; Parent, M.; Calon, F., Internalization of Targeted Quantum Dots by Brain Capillary Endothelial Cells in Vivo. *J Cereb Blood Flow Metab* **2016**, *36* (4), 731-42.
115. Gao, X.; Chen, J.; Chen, J.; Wu, B.; Chen, H.; Jiang, X., Quantum Dots Bearing Lectin-Functionalized Nanoparticles as a Platform for in Vivo Brain Imaging. *Bioconjug Chem* **2008**, *19* (11), 2189-95.
116. Gangadaran, P.; Hong, C. M.; Ahn, B. C., Current Perspectives on in Vivo Noninvasive Tracking of Extracellular Vesicles with Molecular Imaging. *Biomed Res Int* **2017**, *2017*, 9158319.
117. Puzar Dominkus, P.; Stenovec, M.; Sitar, S.; Lasic, E.; Zorec, R.; Plemenitas, A.; Zagar, E.; Kreft, M.; Lenassi, M., Pkh26 Labeling of Extracellular Vesicles: Characterization and Cellular Internalization of Contaminating Pkh26 Nanoparticles. *Biochim Biophys Acta Biomembr* **2018**, *1860* (6), 1350-1361.
118. Takov, K.; Yellon, D. M.; Davidson, S. M., Confounding Factors in Vesicle Uptake Studies Using Fluorescent Lipophilic Membrane Dyes. *J Extracell Vesicles* **2017**, *6* (1), 1388731.
119. Morales-Kastresana, A.; Telford, B.; Musich, T. A.; McKinnon, K.; Clayborne, C.; Braig, Z.; Rosner, A.; Demberg, T.; Watson, D. C.; Karpova, T. S.; Freeman, G. J.; DeKruyff, R. H.; Pavlakis, G. N.; Terabe, M.; Robert-Guroff, M.; Berzofsky, J. A.; Jones, J. C., Labeling Extracellular Vesicles for Nanoscale Flow Cytometry. *Sci Rep* **2017**, *7* (1), 1878.
120. Lai, C. P.; Kim, E. Y.; Badr, C. E.; Weissleder, R.; Mempel, T. R.; Tannous, B. A.; Breakefield, X. O., Visualization and Tracking of Tumour Extracellular Vesicle Delivery and Rna Translation Using Multiplexed Reporters. *Nat Commun* **2015**, *6*, 7029.
121. Field, L. D.; Walper, S. A.; Susumu, K.; Lasarte-Aragones, G.; Oh, E.; Medintz, I. L.; Delehanty, J. B., A Quantum Dot-Protein Bioconjugate That Provides for Extracellular Control of Intracellular Drug Release. *Bioconjug Chem* **2018**, *29* (7), 2455-2467.
122. Zhang, M. Y.; Bishop, B. P.; Thompson, N. L.; Hildahl, K.; Dang, B.; Mironchuk, O.; Chen, N. N.; Aoki, R.; Holmberg, V. C.; Nance, E., Quantum Dot Cellular Uptake and Toxicity in the Developing Brain: Implications for Use as Imaging Probes. *Nanoscale Adv* **2019**, *1* (9), 3424-3442.
123. Blanco-Canosa, J. B.; Medintz, I. L.; Farrell, D.; Mattoussi, H.; Dawson, P. E., Rapid Covalent Ligation of Fluorescent Peptides to Water Solubilized Quantum Dots. *J Am Chem Soc* **2010**, *132* (29), 10027-33.
124. Jiang, X.; Zong, S.; Chen, C.; Zhang, Y.; Wang, Z.; Cui, Y., Gold-Carbon Dots for the Intracellular Imaging of Cancer-Derived Exosomes. *Nanotechnology* **2018**, *29* (17), 175701.
125. Madhankumar, A. B.; Mrowczynski, O. D.; Patel, S. R.; Weston, C. L.; Zacharia, B. E.; Glantz, M. J.; Siedlecki, C. A.; Xu, L. C.; Connor, J. R., Interleukin-13 Conjugated Quantum Dots for Identification of Glioma Initiating Cells and Their Extracellular Vesicles. *Acta Biomater* **2017**, *58*, 205-213.
126. Carnell-Morris, P.; Tannetta, D.; Siupa, A.; Hole, P.; Dragovic, R., Analysis of Extracellular Vesicles Using Fluorescence Nanoparticle Tracking Analysis. *Methods Mol Biol* **2017**, *1660*, 153-173.
127. Wang, J.; Guo, R.; Yang, Y.; Jacobs, B.; Chen, S.; Iwuchukwu, I.; Gaines, K. J.; Chen, Y.; Simman, R.; Lv, G.; Wu, K.; Bihl, J. C., The Novel Methods for Analysis of Exosomes Released from Endothelial Cells and Endothelial Progenitor Cells. *Stem Cells Int* **2016**, *2016*, 2639728.

128. Rodrigues, M.; Richards, N.; Ning, B.; Lyon, C. J.; Hu, T. Y., Rapid Lipid-Based Approach for Normalization of Quantum-Dot-Detected Biomarker Expression on Extracellular Vesicles in Complex Biological Samples. *Nano Lett* **2019**, *19* (11), 7623-7631.
129. Boriachek, K.; Islam, M. N.; Gopalan, V.; Lam, A. K.; Nguyen, N. T.; Shiddiky, M. J. A., Quantum Dot-Based Sensitive Detection of Disease Specific Exosome in Serum. *Analyst* **2017**, *142* (12), 2211-2219.
130. Dobhal, G.; Ayupova, D.; Laufersky, G.; Ayed, Z.; Nann, T.; Goreham, R. V., Cadmium-Free Quantum Dots as Fluorescent Labels for Exosomes. *Sensors (Basel)* **2018**, *18* (10).
131. Zong, S.; Zong, J.; Chen, C.; Jiang, X.; Zhang, Y.; Wang, Z.; Cui, Y., Single Molecule Localization Imaging of Exosomes Using Blinking Silicon Quantum Dots. *Nanotechnology* **2018**, *29* (6), 065705.
132. McNicholas, K.; Michael, M. Z., Immuno-Characterization of Exosomes Using Nanoparticle Tracking Analysis. *Methods Mol Biol* **2017**, *1545*, 35-42.
133. Arruebo, M.; Valladares, M.; Gonzalez-Fernandez, A., Antibody-Conjugated Nanoparticles for Biomedical Applications. *J Nanomater* **2009**, 37-61.
134. Richards, D. A.; Maruani, A.; Chudasama, V., Antibody Fragments as Nanoparticle Targeting Ligands: A Step in the Right Direction. *Chem Sci* **2017**, *8* (1), 63-77.
135. Reth, M., Matching Cellular Dimensions with Molecular Sizes. *Nat Immunol* **2013**, *14* (8), 765-7.
136. Kowal, J.; Arras, G.; Colombo, M.; Jouve, M.; Morath, J. P.; Primdal-Bengtson, B.; Dingli, F.; Loew, D.; Tkach, M.; Thery, C., Proteomic Comparison Defines Novel Markers to Characterize Heterogeneous Populations of Extracellular Vesicle Subtypes. *Proc Natl Acad Sci USA* **2016**, *113* (8), E968-77.
137. Betzer, O.; Perets, N.; Angel, A.; Motiei, M.; Sadan, T.; Yadid, G.; Offen, D.; Popovtzer, R., In Vivo Neuroimaging of Exosomes Using Gold Nanoparticles. *ACS Nano* **2017**, *11* (11), 10883-10893.
138. Busato, A.; Bonafede, R.; Bontempi, P.; Scambi, I.; Schiaffino, L.; Benati, D.; Malatesta, M.; Sbarbati, A.; Marzola, P.; Mariotti, R., Labeling and Magnetic Resonance Imaging of Exosomes Isolated from Adipose Stem Cells. *Curr Protoc Cell Biol* **2017**, *75*, 3 44 1-3 44 15.
139. Busato, A.; Bonafede, R.; Bontempi, P.; Scambi, I.; Schiaffino, L.; Benati, D.; Malatesta, M.; Sbarbati, A.; Marzola, P.; Mariotti, R., Magnetic Resonance Imaging of Ultrasmall Superparamagnetic Iron Oxide-Labeled Exosomes from Stem Cells: A New Method to Obtain Labeled Exosomes. *Int J Nanomedicine* **2016**, *11*, 2481-90.
140. Zhao, J. Y.; Chen, G.; Gu, Y. P.; Cui, R.; Zhang, Z. L.; Yu, Z. L.; Tang, B.; Zhao, Y. F.; Pang, D. W., Ultrasmall Magnetically Engineered Ag₂Se Quantum Dots for Instant Efficient Labeling and Whole-Body High-Resolution Multimodal Real-Time Tracking of Cell-Derived Microvesicles. *J Am Chem Soc* **2016**, *138* (6), 1893-903.
141. Budzinski, K. L.; Sgro, A. E.; Fujimoto, B. S.; Gadd, J. C.; Shuart, N. G.; Gonen, T.; Bajjaleih, S. M.; Chiu, D. T., Synaptosomes as a Platform for Loading Nanoparticles into Synaptic Vesicles. *ACS Chem Neurosci* **2011**, *2* (5), 236-241.
142. Bailey, R. C.; Kwong, G. A.; Radu, C. G.; Witte, O. N.; Heath, J. R., DNA-Encoded Antibody Libraries: A Unified Platform for Multiplexed Cell Sorting and Detection of Genes and Proteins. *J Am Chem Soc* **2007**, *129* (7), 1959-67.
143. Villa, C. H.; Dao, T.; Ahearn, I.; Fehrenbacher, N.; Casey, E.; Rey, D. A.; Korontsvit, T.; Zakhaleva, V.; Batt, C. A.; Philips, M. R.; Scheinberg, D. A., Single-Walled Carbon Nanotubes

- Deliver Peptide Antigen into Dendritic Cells and Enhance Igg Responses to Tumor-Associated Antigens. *Acs Nano* **2011**, *5* (7), 5300-11.
144. Egli, S.; Nussbaumer, M. G.; Balasubramanian, V.; Chami, M.; Bruns, N.; Palivan, C.; Meier, W., Biocompatible Functionalization of Polymersome Surfaces: A New Approach to Surface Immobilization and Cell Targeting Using Polymersomes. *J. Am. Chem. Soc.* **2011**, *133* (12), 4476-83.
145. Nolte-'t Hoen, E.; Cremer, T.; Gallo, R. C.; Margolis, L. B., Extracellular Vesicles and Viruses: Are They Close Relatives? *Proc Natl Acad Sci U S A* **2016**, *113* (33), 9155-61.
146. Lorincz, A. M.; Timar, C. I.; Marosvari, K. A.; Veres, D. S.; Otkocsi, L.; Kittel, A.; Ligeti, E., Effect of Storage on Physical and Functional Properties of Extracellular Vesicles Derived from Neutrophilic Granulocytes. *J Extracell Vesicles* **2014**, *3*, 25465.
147. Kumeda, N.; Ogawa, Y.; Akimoto, Y.; Kawakami, H.; Tsujimoto, M.; Yanoshita, R., Characterization of Membrane Integrity and Morphological Stability of Human Salivary Exosomes. *Biol Pharm Bull* **2017**, *40* (8), 1183-1191.
148. Hermanson, G. T., *Bioconjugate Techniques*. Third edition. ed.; Elsevier/AP: London ; Waltham, MA, 2013; p xvii, 1146 pages.
149. Cheng, Y.; Zeng, Q.; Han, Q.; Xia, W., Effect of Ph, Temperature and Freezing-Thawing on Quantity Changes and Cellular Uptake of Exosomes. *Protein Cell* **2019**, *10* (4), 295-299.
150. Konoshenko, M. Y.; Lekchnov, E. A.; Vlassov, A. V.; Laktionov, P. P., Isolation of Extracellular Vesicles: General Methodologies and Latest Trends. *Biomed Res Int* **2018**, *2018*, 8545347.
151. Paolicelli, R. C.; Bergamini, G.; Rajendran, L., Cell-to-Cell Communication by Extracellular Vesicles: Focus on Microglia. *Neuroscience* **2019**, *405*, 148-157.
152. Zhang, C.; Mastorakos, P.; Sobral, M.; Berry, S.; Song, E.; Nance, E.; Eberhart, C. G.; Hanes, J.; Suk, J. S., Strategies to Enhance the Distribution of Nanotherapeutics in the Brain. *J. Control. Release* **2017**, *267*, 232-239.

CURRICULUM VITAE

Mengying Zhang

6532 34th AVE NE, Unit A, Seattle, WA, 98115

Phone: (206)-954-5417 Email: myz16@uw.edu

I. EDUCATION

- 2015-2020 University of Washington, Seattle, WA
Ph.D. in Molecular Engineering and Sciences
Dissertation: “*Quantum dot probes for neuroimaging and visualization of extracellular vesicles.*”
- 2011-2015 Sichuan University, Chengdu, Sichuan, China
B.S. in Biological Sciences
Wuyuzhang Honorary College
SCU-UW Exchange Program 2013-2014

II. PROFESSIONAL EXPERIENCE

- 2015-Present University of Washington, Seattle, WA
Graduate Research Assistant, Advisor: Elizabeth Nance
Lead study design, SOP generation, experiments, data analysis, research collaboration, and manuscript preparation for various research projects, including:
- Systematically evaluated quantum dots (QDs) with different surface chemistries on their colloidal stability, toxicity, molecular mechanisms, and cellular uptake in central nervous system (CNS) using *in vitro*, *ex vivo*, and *in vivo* brain models.
 - Developed a controllable approach to label human semen/rat brain extracellular vesicles with QDs for high throughput imaging.
 - Applied confocal microscopy and imaging processing to investigate the efficiency of a novel immunotherapy against triple-negative breast cancer, by analyzing its intratumoral distribution.
 - Worked in a BSL-2 environment and developed a QD-based platform for labeling and imaging Zika virus.
 - Investigated the interaction between brain cells and nanotherapeutic under different disease severity, using ischemic brain slice models.
 - Resulted in 7 first-author or co-author peer-reviewed paper publications and 2 oral presentations at top-tier conferences.
- 2019 University of Washington, Seattle, WA
Teaching Assistant for Engineering Transformation of Health, College of Engineering
- Led lab sessions of 3D printing, computer-aided design (CAD), programming & microprocessing (Arduino).
 - Mentored 9 students in a 5-week design project for the successful design of functional 3D prosthetic hand.
- 2014-2015 University of Washington, Seattle, WA
Undergraduate Research Assistant, Advisor: Miqin Zhang
- Utilized cell culture, fluorescence microscopy, agarose cell migration assay, FTIR analysis, rheological analysis, and western blot to characterize and optimize PEG-grafted chitosan hydrogel as drug depot for treating brain cancer.

III. HONORS and AWARDS

- 2019 *Nanoscale Advances* selected back cover image
2019 GSFEI Graduate Student Travel Award to “BMES 2019 Annual Meeting”
2017 GSFEI Graduate Student Travel Award to “2017 AIChE Annual Meeting”
2015 Sichuan University Annually Outstanding Undergraduate Thesis
2013-2014 China Scholarship Council (CSC) full scholarship for exchange study at the University of Washington

IV. PUBLICATIONS

1. Joseph, A., Liao, R., **Zhang, M.**, Helmbrecht, H., McKenna, M., Filteau, J., & Nance, E. (2020). Nanoparticle-microglial interaction in the ischemic brain is modulated by injury duration and treatment. *Bioengineering & Translational Medicine*, e10175.
2. Helmbrecht, H., Joseph, A., McKenna, M., **Zhang, M.**, & Nance, E. (2020). Governing transport principles for nanotherapeutic application in the brain. *Current Opinions in Chemical Engineering*.
3. Chua, C. Y. X., Ho, J., Susnjar, A., Lolli, G., Di Trani, N., Pesaresi, F., **Zhang, M.**, Nance, E & Grattoni, A. (2020). Intratumoral Nanofluidic System for Enhancing Tumor Biodistribution of Agonist CD40 Antibody. *Advanced Therapeutics*, 2000055.
4. **Zhang, M.**, Vojtech, L., Ye, Z., Hladik, F., & Nance, E. (2020). Quantum Dot Labeling and Visualization of Extracellular Vesicles. *ACS Applied Nano Materials*, 3(7), 7211-7222.
5. Vojtech, L., **Zhang, M.**, Davé, V., Levy, C., Wang, R., Calienes, F., Prlic, M., Hughes, S., Nance, E., & Hladik F. (2019). Extracellular vesicles in human semen modulate antigen-presenting cell function and decrease downstream antiviral T cell responses. *PLoS one*, 14(10), e0223901.
6. **Zhang, M.**, Bishop, B., Thompson, N., Hildahl, K., Dang, B., Mironchuk, O., Chen, N., Aoki, R., Holmberg, V., & Nance E. (2019). Quantum dot cellular uptake and toxicity in the developing brain: implications for use as imaging probes. *Nanoscale Advances*, 1(9), 3424-3442.
7. Curtis, C., **Zhang, M.**, Liao, R., Wood, T., & Nance, E. (2017). Systems-level thinking for nanoparticle-mediated therapeutic delivery to neurological diseases. *Wiley Interdiscip Rev Nanomed Nanobiotechnol*. 9(2), e1422. **selected cover image: Curtis, C., Zhang, M., Liao, R., Wood, T., & Nance, E. Cover Image, Volume 9, Issue 2. *WIREs Nanomed Nanobiotechnol*, (2017) 9: n/a, e1463. doi:10.1002/wnan.1463
8. Chang, F. C., Tsao, C. T., Lin, A., **Zhang, M.**, Levengood, S. L., & Zhang, M. (2016). PEG-chitosan hydrogel with tunable stiffness for study of drug response of breast cancer cells. *Polymers*, 8(4), 112.
9. Tsao, C. T., Hsiao, M. H., **Zhang, M. Y.**, Levengood, S. L., & Zhang, M. (2015). Chitosan-PEG hydrogel with sol-gel transition triggerable by multiple external stimuli. *Macromolecular rapid communications*, 36(3), 332-338.

V. PRESENTATIONS and PUBLIC TALKS

1. Ye, Z., **Zhang, M.**, Nance, E. (2020). Quantifying the effect of brain-derived extracellular vesicles on microglia cells *in vitro*. University of Washington Undergraduate Research Symposium. (Oral Presentation).
2. **Zhang, M.**, Nance, E. (2020). Quantum dot-based probes for characterizing neuroinflammation and tracking extracellular vesicles in the developing brain. UW Biomaterials Seminar Series. (Oral Presentation).
3. **Zhang, M.**, Vojtech, L., Nance, E. (2019). Quantum dot labeling and tracking of extracellular vesicles. 2019 Biomedical Engineering Society (BMES) Annual Meeting. (Oral Presentation).
4. Adebayo, T., **Zhang, M.**, Nance, E. (2019). Quantum dot toxicity and intracellular uptake on BV-2 cells. 2019 Summer STEM Research Poster Session. (Poster).
5. Adebayo, T., **Zhang, M.**, Nance, E. (2019). Quantum dot toxicity and intracellular uptake on BV-2 cells. UW GenOM Project ALVA Program Oral Presentation and Closing Ceremony. (Oral Presentation).
6. **Zhang, M.** (2019). A nano-adventure to the brain. Town Hall Seattle. (Public Oral Talk).

7. **Zhang, M.**, Bishop, B., Hildahl, K., Mironchuk, O., Dang, B., Thompson, N., Holmberg, V., Nance, E. (2018). Systematic evaluation of CdSe quantum dot toxicity and cellular uptake in the developing brain. The 16th International Nanomedicine & Drug Delivery Symposium (NanoDDS). (Poster).
8. Hildahl, K., **Zhang, M.**, Nance, E. (2018). Characterization of quantum dot toxicity for potential use as biomarker in brain injury. University of Washington Undergraduate Research Symposium. (Oral Presentation).
9. Mironchuk, O., **Zhang, M.**, Nance, E. (2018). Characterization of quantum dot stability in the brain microenvironment for potential use as biomarkers. University of Washington Undergraduate Research Symposium. (Poster).
10. **Zhang, M.**, Dang, B., Hildahl, K., Bishop, B., Aoki, R., Thompson, N., Holmberg, V., Nance, E. (2017). Quantum dot-based biomarkers of neuroinflammation in the developing brain. The American Institute of Chemical Engineers (AIChE) Annual Meeting. (Oral Presentation).
11. **Zhang, M.**, Bishop, B., Dang, B., Hildahl, K., Aoki, R., Thompson, N., Mironchuk, O., Holmberg, V., Nance, E. (2017). Quantum dot-based biomarkers of neuroinflammation in the developing brain. UW Chemical Engineering Graduate Student Symposium. (Poster).
12. Dang, B., **Zhang, M.**, Hildahl, K., Nance, E. (2017). The role of surface chemistry in cellular uptake of quantum dots in the developing brain. University of Washington Undergraduate Research Symposium. (Oral Presentation).
13. **Zhang, M.**, Nance, E. (2017). Quantum dot-based biomarkers of neuroinflammation in the developing brain. UW Biomaterials Seminar Series. (Oral Presentation).
14. Hildahl, K., **Zhang, M.**, Nance, E. (2017). Characterization of quantum dot toxicity for potential uses as a biomarker in brain injury. University of Washington Undergraduate Research Symposium. (Poster).
15. **Zhang, M.**, Kievit, F., Tsao, F., Zhang, M. (2014). "Rocket Project": A liquid transition drug delivery system for brain cancer. University of Washington Undergraduate Research Symposium. (Poster).

VI. LEADERSHIP EXPERIENCE

- 2019-Present Engage: The Science Speaker Series and Seminar, *Director, Tech Manager, Social Media Director, Workshop Committee*
- 2019-2020 Women in Chemical Engineering (WChE), University of Washington, *Secretary*
- 2017 2nd Annual Fall Industry Panel of Women in Chemical Engineering, *Committee Member*
- 2016-2018 UW Engineering Discovery Days, *Volunteer*
- 2013-2015 Foundation International Understanding Through Student (FIUTS), University of Washington, *Facilitator and Volunteer*
- 2012 the 9th World Biomaterials Congress, *Volunteer*
- 2008-2011 Zhaohua Literature Society, Chengdu No.7 High School, *Chief Editor*
- 2008-2011 Student TV Station, Chengdu No.7 High School, *Reporter*

VII. MENTORSHIP

Graduate Student

03/2020-Present Nam Phuong Nguyen, Molecular Engineering and Sciences Ph.D. student

Undergraduate Students

07/2019-Present Tolulope Adebayo, Undecided Bachelor's student, *ALVA Program Fellow*
06/2019-Present Ziming Ye, Chemical Engineering Bachelor's student
06/2018-04/2019 Nina Chen, Biology Bachelor's student
06/2017-01/2019 Olesya Mironchuk, Bioengineering and Neurobiology Bachelor's student
05/2016-06/2018 Kate Hildahl, Chemical Engineering Bachelor's student, *Mary Gates Scholar*
01/2016-09/2017 Binh Dang, Chemical Engineering Bachelor's student, *Mary Gates Scholar*

VIII. SKILLS

Technical knowledge and skills: Molecular and Cellular Biology, Neurobiology, Immunology, Mammalian Cell Culture (Suspension and Adherent), Tissue Culture, Tissue Harvesting, Tissue Processing and Sectioning, Immunohistochemistry, Human Tissue Experiment, Animal Handling Experience, Flow Cytometry, Fluorescence-Activated Cell Sorting (FACS), Nanoparticle Characterization, Cross-Linking, Biodegradable Polymer, Polymer Nanoparticle Synthesis, Hydrogel, Dynamic Light Scattering (DLS), Nanoparticle Tracking Analysis (NTA), DNA and RNA Isolation, NanoDrop, Real-Time Quantitative Polymerase Chain Reaction (RT-qPCR), Reverse Transcription Polymerase Chain Reaction (RT-PCR), Colorimetric Assay (BCA Assay), Imaging, Confocal Microscopy, Live Cell Imaging, Image Processing and Analysis (ImageJ), UV-Vis Spectrometer, Cytotoxicity Analysis, Cell Based Assays, Western Blot (WB), Microfluidics, Extracellular Vesicle (EV) Isolation and Purification, Size Exclusion Chromatography (SEC), Bioconjugation, Genotyping, Transmission Electron Microscopy (TEM), Drug Delivery, FTIR, Graphpad Prism, 3D Printing, Data Analysis, Basic Knowledge of Python for Image Analysis, Statistical Analysis for Biomedical Research, etc.

Communication skills: Oral and Written Presentation, Public Talks, Microsoft Office, Science Communication, Science Writing, Workshop Organizing, Newsletter Generation, Multi-Media Communication.

Languages: English, Chinese.

IX. REFERENCES

Elizabeth Nance, Ph.D.

Clare Boothe Luce Assistant Professor, Chemical Engineering
Adjunct Assistant Professor, Radiology, School of Medicine
University of Washington
enance@uw.edu
206-543-2216

Lucia Vojtech, Ph.D.

Research Assistant Professor, Obstetrics & Gynecology
University of Washington
luciv@uw.edu
206-399-6461

Vincent Holmberg, Ph.D.

Assistant Professor, Chemical Engineering
Faculty Member, Molecular Engineering & Sciences Institute, Clean Energy Institute
University of Washington
holmvc@uw.edu
206-616-0199